
**A New Seismological Network for
Bavaria and its Application to the
Study of Meteorologically Triggered
Earthquake Swarms**

*Inaugural-Dissertation
zur
Erlangung des Doktorgrades
der
Fakultät für Geowissenschaften
der
Ludwig-Maximilians-Universität München*

vorgelegt im Mai 2006 von

Toni Kraft

1. Berichterstatter: Prof. Dr. Heiner Igel
2. Berichterstatter: Prof. Dr. Valerian Bachtadse

Tag der mündlichen Prüfung: 18. August 2006

To
Robert Kraft
(* 1935 - † 2002)



*Groß und mächtig - schicksalsträchtig
um seinen Gipfel jagen - Nebelschwaden.
A Donnern schickt er oft ins Tal
und dann schauderts alle auf amal.
Wann er donnert, Gott behüt,
der Berg, der kennt kein Einsehn net.
Staufen, Staufen, Schicksalsberg,
du bist so groß - und i nur a Zwerg.*

W. Ambros & J. Prokopetz (Der Berg, 1974)
(leicht abgewandelt ;-)

Contents

Contents	i
List of Figures	iv
List of Tables	viii
Zusammenfassung	xi
Summary	xix
I A New Seismological Network for Bavaria	1
1 History of Seismology in Bavaria	3
1.1 The Bavarian Earthquake Service	3
1.2 Other Seismological Networks in Bavaria	7
1.2.1 Seismological Central Observatory Gräfenberg	7
1.2.2 German Continental Deep Drilling Program	9
1.2.3 German Regional Seismic Network	10
1.2.4 German Experimental Seismic System	11
1.3 Motivation for a New Bavarian Network	12
2 A New Bavarian Seismological Network	15
2.1 Network Geometry and Seismicity	15
2.2 Technical Station Design	20
2.2.1 Hardware	21
2.2.2 Software	26
2.3 The Data Center	30
2.3.1 Hardware	30
2.3.2 Software	32
2.4 Public Presentation of the Data	35
2.4.1 Homepage of the Bavarian Earthquake Service	35

2.4.2	Homepage of the Geophysics Institute	43
2.5	Network Performance and Outlook	47
II	The 2002 Mt. Hochstaufen Earthquake Swarms	49
3	Indication for Rainfall-Triggering	51
3.1	Introduction	52
3.2	The Study Area	53
3.2.1	Geography, Morphology, Tectonics and Geology	53
3.2.2	Previous Studies and Seismicity	55
3.2.3	Seismo-Meteorological Network	57
3.3	The 2002 Earthquake Swarms	59
3.3.1	Data Analysis, Derivation of Velocity Model	59
3.3.2	Observed Seismicity	61
3.4	Hydrological Interpretation	65
3.5	Discussion and Conclusion	69
4	Relocation and Focal Mechanisms	73
4.1	Introduction	74
4.2	Study Area and Data	75
4.3	Cluster Analysis	79
4.4	Multi-Event Semi-Automatic Phase Repicking	82
4.5	Earthquake Relocation	84
4.5.1	Probabilistic Earthquake Location	84
4.5.2	Master Event Location Technique	88
4.5.3	Result of the Relocation	92
4.6	Focal Mechanism Determination	94
4.7	Discussion	99
4.8	Conclusions	101
4.9	Acknowledgements	102
5	Evidence for Rainfall-Triggering	103
5.1	Introduction	103
5.2	Seismicity at Mt. Hochstaufen	104
5.3	Seismicity Model	106
5.4	Results	107
5.5	Discussion	111
5.6	Conclusions	112
5.7	Acknowledgments	112

Bibliography	113
Appendix	127
A Seismological station	127
B Content of Supplement CD	151
Acknowledgments	155
Curriculum Vitae	157

List of Figures

1.1	”Earthquake House” at the Royal Astronomical Observatory in Munich.	4
1.2	Map of the Bavarian network in the end of 2000.	6
1.3	Map of the Gräfenberg-Array (GRF).	8
1.4	Map of the KTB-Net.	9
1.5	Map of the German Regional Seismic Network (GRSN).	10
1.6	Station locations of the GERESS array in Southeastern Germany.	11
2.1	Geological map of Bavaria.	16
2.2	Map of earthquakes felt in Bavaria (1000-2002)	17
2.3	Earthquake swarm region of Vogtland/Western Bohemia	18
2.4	Map of the new Bavarian Seismological Network.	19
2.5	Station hardware of the new Bavarian Seismological Network.	22
2.6	Hardware of the weather stations	26
2.7	Data flow diagram of the Bavarian seismological network.	27
2.8	Design and dataflow of the data center FUR.	31
2.9	Data section of the Bavarian Earthquake Service homepage	36
2.10	Virtual matrix structure of data display.	37
2.11	Example for seismogram display on the BayernNetz homepage.	39
2.12	Example for spectrogram display on the BayernNetz homepage.	40
2.13	Example for GPS position display on the BayernNetz homepage.	41
2.14	Example for weather data display on the BayernNetz homepage.	41
2.15	Picture of the info center of the BayernNetz	42
2.16	Example of the 24h-seismogram plot of the Geophysics Institute homepage.	44

2.17	Example of the 24h-spectrogram plot of the Geophysics Institute homepage.	45
2.18	Example of the 24h-seismicity world map of the Geophysics Institute homepage.	46
2.19	Example of the Google news ticker linked on the Geophysics Institute homepage.	46
3.1	Tectonic map of the region around the study area.	54
3.2	Schematic geological cross section of Mt. Hochstaufen.	55
3.3	Macroseismicity of the Bad Reichenhall area between 1000 and 2005.	56
3.4	Seismo-meteorological network around Mt. Hochstaufen.	58
3.5	Location error obtained with Hypo71 and the minimum-1D-velocity model for Mt. Hochstaufen earthquakes in 2002.	60
3.6	Epicenters of 546 earthquakes in 2002 located using Hypo71 and the derived minimum-1D-velocity model.	62
3.7	Spatio-temporal development of the seismicity in 2002.	64
3.8	Gray scaled normalized time series of precipitation, seismicity, and increase rate of groundwater level for 2002.	65
3.9	Time-depth plots for three earthquake swarm of 2002.	68
4.1	Tectonic map of the region around the study area.	76
4.2	Seismo-meteorological network around Mt. Hochstaufen.	77
4.3	Spatio-temporal development of the seismicity in 2002.	78
4.4	Similarity matrix and clusters obtained by pairwise single linkage clustering.	80
4.5	Example seismograms of station STAU form three clusters found in 2002.	81
4.6	Normalized cumulative histogram of standard deviations of arrival-time differences $\sigma^{cl}(dt_p, dt_s)$	84
4.7	Pseudo-3D-velocity model with topography used for probabilistic nonlinear earthquake location.	85
4.8	Examples of probabilistic location result.	87
4.9	Error analysis of the probabilistic earthquake location.	88
4.10	Geometrical layout for master-event technique.	89
4.11	Relocation results for four clusters.	91
4.12	Hypocenter map of 2002 Mt. Hochstaufen seismicity before and after relocation, and spatio-temporal development of the seismicity.	92

4.13	Focal mechanisms of 25 events with a variance less than 20° of the fault-plane normals.	95
4.14	Epicenter map of the 25 derived focal mechanisms.	99
5.1	2002 Epicenter map and profiles of the Staufeu Massif.	105
5.2	Result of the parameter search for maximizing the likelihood value.	108
5.3	Spatio-temporal patterns of pore pressure and estimated earthquake rate.	109
5.4	Correlation analysis of observed earthquake rate.	110
A.1	Map of the new Bavarian Seismological Network.	127

List of Tables

2.1	Technical data of Lennartz LE3Dlite and Streckeisen STS-2 seismometers.	24
3.1	Cross-correlation result for precipitation, seismicity, and increase rate of groundwater level for 2002.	66
4.1	Uncertainty/phase-weighting scheme for picking, cross-correlation and NonLinLoc Gaussian error estimation.	83
4.2	Source parameters of 25 events with a variance less than 20° of the fault-plane normals.	97
A.1	Station parameters of the Bavarian seismological Network. . .	128

Zusammenfassung

Die vorliegende Arbeit befasst sich mit zwei eigenständigen Themen, deshalb ist sie in zwei Teile gegliedert. Im ersten Teil wird der Aufbau eines neuen seismologischen Stationsnetzes für Bayern beschrieben, wohingegen der zweite Teil über die Untersuchung der durch Regen ausgelösten seismischen Aktivität bei Bad Reichenhall in Südost-Bayern berichtet.

Teil 1

Im August 2005 konnte der Bayerische Erdbebendienst auf eine Geschichte von 100 Jahren zurückblicken, da am 2. August 1905 an der königlich-bayerischen Sternwarte in München-Bogenhausen die erste bayerische Erdbebenstation in Betrieb genommen wurde. In den darauf folgenden vier Jahrzehnten wurden über unterschiedlich lange Zeiträume bis zu vier weitere Erdbebenstationen in Bayern betrieben, bis 1944 kriegsbedingt der Betrieb des seismologischen Dienstes zum Erliegen kam.

Ab Mitte der 1950er Jahre wurden verschiedene seismologische Projekte in Bayern begonnen. Zum einen begann die Universität München mit dem Wiederaufbau des Bayerischen Erdbebennetzes, das bis zum Jahre 2001 auf zwölf Stationen in Bayern und Österreich erweitert wurde. Die Stationen wurden nahe den bekannten Erdbebengebieten in Bayern aufgestellt, allerdings mussten sie aufgrund der begrenzten Speicherkapazität und des kleinen Übertragungsvolumens mit geringen Abtastfrequenzen und im Triggermodus betrieben werden. Einige Stationen wurden sogar bis Ende der 1990er Jahre mit Tintenregistrierung betrieben und standen erst nach einigen Tagen zur Auswertung zur Verfügung.

Außerdem wurden im Zuge der Überwachung von Kernwaffentests - und später zu wissenschaftlichen Zwecken - sogenannte Arrays in Bayern installiert. Diese nutzen eine aus der Astronomie bekannte Technik, bei der

einzelne Empfänger zu einer Antenne zusammengeschaltet werden, die dann mit Methoden der Signalverarbeitung auf bestimmte Beobachtungsrichtungen eingestellt werden kann. Die Instrumentierung der Arraystationen wurde so gewählt, das sie optimal zur Registrierung von Fern- und Regionalbeben, also für Erdbeben im Entfernungsbereich über 600 km, geeignet waren. Seismogramme von Beben aus diesem Entfernungsbereich setzen sich aus langwelligen Schwingungen zusammen, die im wesentlichen weniger als eine Schwingung pro Sekunde enthalten. Deshalb können die Abtastraten zur Digitalisierung dieser Daten klein sein. In Bayern erreichten sie maximal 80 Hz, was für die Aufzeichnung vieler Lokalbeben zu wenig ist.

Ende des Jahres 2000 fand man in Bayern also folgende Situation vor: Die vorhandenen Erdbebenstationen waren hauptsächlich für die Registrierung von entfernten Erdbeben geeignet. Außerdem konnten die wenigen für die Aufzeichnung von Lokalbeben optimierten kurzperiodischen Messstationen aufgrund der Aufzeichnung im Triggermodus und des zu großen Stationsabstandes keine schnelle und verlässliche Erdbebenlokalisierung gewährleisten. So war es keine Ausnahme, dass gespürte Beben erst durch Anrufe besorgter Personen bei der Polizei oder am Geophysikalischen Observatorium der Universität München bekannt wurden und nur mit großer zeitlicher Verzögerung lokalisiert werden konnten. Aus dieser Situation heraus beschlossen die Universität München und das Bayerische Geologische Landesamt, einen Antrag zum Ausbau des bayerischen Erdbebennetzes bei der Bayerischen Staatsregierung einzureichen. Dieser Antrag wurde im Oktober 2000 genehmigt und der Aufbau eines Messnetzes von 21 modernen seismologischen Stationen begonnen.

Die Wahl der Stationsstandorte orientierte sich eng an der bekannten Seismizität von Bayern. Bei Marktredwitz in Nordost-Bayern und bei Bad Reichenhall in Südost-Bayern wurden Subnetze von je sechs Stationen errichtet, um die in diesen Gebieten auftretenden Erdbebenschwärme zu untersuchen. Auf letztere wird im zweiten Teil der Arbeit näher eingegangen. Weitere Stationsstandorte finden sich in der Hohen Rhön (NW-Bayern), im Nördlinger Ries und im Altmühltal (Zentral-Bayern), sowie entlang des nördlichen Alpenrandes in Oberstdorf, Garmisch-Partenkirchen und Berchtesgaden. Die Stationen sind über ISDN an das Datenzentrum im Geophysikalischen Observatorium in Fürstenfeldbruck angeschlossen. Hier findet die Auswertung und die Archivierung der aufgezeichneten Daten statt. Die Daten der einzelnen Stationen werden in Form von Seismogrammbildern

der letzten sechs Stunden im Internet veröffentlicht und in regelmäßigen Abständen aktualisiert (30-60 min). Eine interaktive Website erlaubt die Sichtung von Daten der letzten fünf Tage. Der Zugriff auf die Daten der letzten 90 Tage aller Stationen ist über das Datenzentrum mit wenigen Minuten Verzögerung jederzeit möglich.

Das neue bayerische seismologische Netz erlaubt die echtzeitnahe Beurteilung der seismischen Aktivität und die schnelle Information von Behörden und Bevölkerung im Falle gespürter Erdbeben. Die Erhöhung der Stationsdichte sowie der Datenqualität ermöglicht es außerdem, vielseitige wissenschaftliche Fragestellungen zu untersuchen, die von der Erdbebengefährdung Bayerns bis zur Untersuchung von regen-induzierten Erdbeben am Hochstaufen bei Bad Reichenhall reichen. Letzteres wird im zweiten Teil der Arbeit beschrieben.

Teil 2

Das Gebirgsmassiv des Hochstaufen ist ein Ost-West streichender, 10 km langer Rücken, der mit seinen 1775 m Höhe markant die Umgebung überragt. Als Teil des Tirolischen Bogens der Nördlichen Kalkalpen bildet er die Grenze zur Flyschzone im Norden und ist hauptsächlich aus unter- bis mittel-triassischen Kalkformationen aufgebaut. Die Schichtung der Gesteine ist durch die Überschiebung der alpinen Decken nach Norden aufgestellt. Geologisch nachgewiesene gravitative Massenbewegungen haben im Gipfelbereich des Berges zur Ausbildung von Großklüften geführt, die mehrere Meter geöffnet und mindesten 100 m tief sind. Nach Süden schließt sich das sedimentgefüllte Reichenhaller Becken mit salinen Serien an, das vom Staufen durch die linkslaterale Störungszone des Saalach-Westbruchs getrennt ist. Weiter südlich schließt sich als weitere kalkalpine Decke die Bechtesgadener Masse an.

Das erste bekannte Erdbeben in Bayern fand am 16. Oktober 1390 bei Bad Reichenhall statt und wurde dort mit einer makroseismischen Intensität von V (MSK) wahr genommen. Beben bis zu dieser Größe ereigneten sich im Raum Bad Reichenhall im Abstand von wenigen Jahren immer wieder und wurden als Einsturzbeben aus dem Gebiet der Reiteralm südlich von Bad Reichenhall angesehen. Nach der Installation einer Erdbebenstation in der Alten Saline von Bad Reichenhall im Jahr 1972 wurde erkannt, dass sich neben den regelmäßig gefühlten Beben auch viele Mikrobeben ereignen.

Diese treten gehäuft in den Sommermonaten auf, die auch die höchsten Niederschlagsmengen aufweisen. Erst in den 1980er Jahren konnte, durch die Installation eines temporären seismologischen Messnetzes, der Gebirgszug des Hochstaufen nördlich von Bad Reichenhall als Herdgebiet identifiziert werden und Einsturzbeben als Ursache für die beobachtete Seismizität ausgeschlossen werden. Wenig später konnte die Korrelation von langjährigen monatlich gemittelten Zeitreihen der Seismizität, des Niederschlages und des Grundwasserstandes nachgewiesen werden.

Eine Besonderheit ist der Schwarmbebencharakter der beobachteten Seismizität. Obwohl es keine wissenschaftlich präzise Definition des Begriffes Erdbebenschwarm gibt, versteht man darunter im Allgemeinen eine Erdbebenserie bei der keine Einteilung der Seismizität in Vor-, Haupt- und Nachbeben vorgenommen werden kann. Charakteristisch ist häufig ein langsames zeitliches An- und Abklingen der seismischen Aktivität das keiner bekannten Gesetzmäßigkeit folgt. Erdbebenschwärme treten weltweit hauptsächlich in vulkanisch aktiven Regionen auf. Man vermutet deshalb, dass sie durch die Bewegung von Fluiden (Gase und/oder Flüssigkeiten) in der Erdkruste verursacht werden. Auch künstlich erzeugte Schwärme von Mikroerdbeben wurden z. B. bei der Erdölförderung und Druckversuchen in tiefen Bohrlöchern beobachtet.

Mit der Installation eines Subnetzes von sechs kontinuierlich registrierenden seismologischen Stationen des in Teil 1 beschriebenen BayernNetzes im Bereich der Hochstaufen-Massives, stand ab Mitte 2001 ein Werkzeug zur hochauflösenden Untersuchung des raum-zeitlichen Seismizitätsmusters zur Verfügung. In dieser Arbeit wird im Speziellen über die Untersuchung der Seismizität im Jahr 2002 berichtet.

Im März und August 2002 kam es im Raum Bad Reichenhall zu starken Regenfällen, die innerhalb von 24 h, bzw. 48 h, den jeweiligen Monatsdurchschnitt überschritten. Die Starkniederschläge im August führten zu Jahrhunderthochwassern in Mitteleuropa, die einen Schaden von 18.5 Milliarden Euro verursachten. Zeitgleich mit den Niederschlagsereignissen stieg die Anzahl der pro Tag registrierten Mikrobeben im Bereich des Hochstaufen stark an. Sie erreichten nach jeweils zehn Tagen ihr Maximum und blieben für mehrere Monate auf einem erhöhten Niveau. Der Vergleich der täglichen Erdbebenrate mit Zeitreihen des Niederschlages und des Grundwasseranstieges zeigt, dass diese auch im kleinskaligen Bereich gut

übereinstimmen. Die Kreuzkorrelation der gefilterten Zeitreihen ergab sehr hohe Werte für relative Zeitversätze von 8-10 Tagen.

Insgesamt wurden 1171 Mikroerdbeben registriert. Das stärkste Ereignis, am 10. April, hatte eine Lokalmagnitude von $m_l=2.4$. Es wurden allerdings auch Beben bis zu einer Magnitude von $m_l=-1.6$ aufgezeichnet. Aus der Häufigkeitsverteilung der Magnituden kann die Vollständigkeit des Erdbeben-datensatzes für Beben einer Magnitude größer $m_l=-0.2$ abgeleitet werden. Mit den seismologischen Stationen des BayernNetzes und drei zusätzlichen Mobilstationen konnten 546 Erdbeben lokalisiert werden, woraus sich das folgend Bild der Seismizität ergab. Der erste Erdbebenschwarm im März 2002 ereignete sich südlich des Hochstaufen nahe des Thumsees in einem kleinen Herdvolumen in ungefähr 3 km Tiefe. Die Epizentren des im August beginnenden Schwarmes waren im Gegensatz dazu diffus über das Gebirgsmassiv des Staufen verteilt. Auffällig ist eine zeitliche Verlagerung der Seismizität in die Tiefe. Diese konnte besonders deutlich am Anfang des August-Schwarmes beobachtet werden.

Die Wanderung der Erdbebenherde wurde mit einem einfachen hydrodynamischen Modell untersucht. Das Coulomb-Bruchkriterium besagt, dass die Scherfestigkeit eines Materials proportional zur Normalspannung auf die potentielle Bruchfläche ist. Der Porendruck wirkt dem Normaldruck entgegen und verringert so die Scherfestigkeit. Andererseits folgt der raumzeitliche Verlauf einer von der Oberfläche eines poro-elastischen Halbraums in die Tiefe diffundierenden Druckstörung im Zeit-Tiefen-Diagramm einer Wurzelfunktion, die von der Diffusivität des Halbraumes abhängt. Das heißt, wenn die Erdbeben durch eine Erhöhung des Porendruckes ausgelöst werden, sollte die in einem solchen Diagramm aufgetragene Seismizität hauptsächlich im Bereich erhöhten Porendrucks unter der Wurzelfunktion liegen. Die Diffusivität des Halbraumes lässt sich dann über die Anpassung der Wurzelfunktion an die beobachtete Seismizität abschätzen.

Zur Anpassung der Wurzelfunktion an die Seismizität wurde ein Verfahren entwickelt, das die Diffusivität ausgehend von $0 \text{ m}^2/\text{s}$ solange erhöht, bis sämtliche Erdbeben darunter zu liegen kommen. Der Prozentsatz der sich unter der Wurzelfunktion befindenden Erdbeben wird dann gegen die Diffusivität aufgetragen. Dabei entsteht eine Kurve, die man mit zwei Geraden annähern kann. Aus dem Schnittpunkt der Geraden erhält man die gesuchte Diffusivität. Das Verfahren wurde mit synthetischen Daten

getestet und liefert zusätzlich zu früheren Verfahren eine Fehlerabschätzung für die Diffusivität. Sämtliche Schwärme des Jahres 2002 wurden mit dieser Methode untersucht. Der Nullpunkt der Wurzelfunktion wurde dabei an die Zeit des jeweiligen Regenereignisses gesetzt. Die abgeschätzte Diffusivität von $0.75 \pm 0.35 \text{ m}^2/\text{s}$ stimmt gut mit Werten aus anderer Arbeiten überein und deutet an, dass der Mechanismus der Porendruckdiffusion eine wichtige Rolle bei der Auslösung von Erdbeben im Hochstaufer spielt.

Um die Ergebnisse der ersten Untersuchung zu verifizieren, wurde in einem nächsten Schritt eine hochgenaue Relokalisierung der Erdbeben des Jahres 2002 durchgeführt. Dabei wurde ausgenutzt, dass sich im beobachteten Datensatz viele Erdbeben befinden, die sehr ähnliche Seismogramme besitzen. Mit Hilfe von Kreuzkorrelations- und anschließender Clusteranalyse wurden Gruppen ähnlicher Erdbeben, sogenannte Cluster, zusammengestellt. Man kann davon ausgehen, dass solche Ereignisse räumlich sehr nahe zusammenliegen und dies zur hochgenauen Lokalisierung nutzen. Dabei wird ein Beben des Clusters zum Masterevent erklärt und die restlichen, mit Hilfe der sehr genauen relativen Einsatzzeiten aus der Kreuzkorrelationsanalyse, relativ dazu lokalisiert. Die Ausdehnung der Cluster schrumpfte mit der Relokalisierung bis auf wenige 10er Meter zusammen. Allerdings liegt die berechnete Unsicherheit der relativen Lokalisierung im selben Bereich, sodass keine Interpretation der inneren Struktur der Cluster vorgenommen werden konnte.

Zur Verbesserung der absolute Lokalisierungen wurden ein 3D-Geschwindigkeitsmodell erstellt. Es setzte sich aus zwei homogenen Viertelräumen zusammen, die einerseits den Flysch andererseits das Kalkalpin repräsentierten, und besaß eine realistische Topographie. Ein finite-Differenzen Algorithmus zur Laufzeitberechnung wurde in Verbindung mit einem probabilistischen Inversionsansatz zu Lokalisierung von 612 Erdbeben verwendet. Die Unsicherheit der Lokalisierung war mit einem Mittel von 200 m sehr gering und konnte durch die Kombination mit den Ergebnissen der Masterevent-Lokalisierung noch verbessert werden.

Nach der Relokalisierung treten in der Seismizitätsverteilung deutliche Muster hervor. Die Erdbeben des Jahres 2002 im Staufen-Massiv fanden zwischen 1700 m üNN - d. h. mehr als 1000 m über Bad Reichenhall - und 4200 m uNN statt, wobei der Großteil unterhalb 1000 m üNN liegt. Die Erdbebenherde scheinen zwei planaren Strukturen zu folgen. Eine streicht

nach Norden und fällt steil nach Westen ein, die andere streicht nach Westen und fällt sehr flach nach Süden ein. Keine der Strukturen kann jedoch eindeutig mit geologischen Strukturen in Verbindung gebracht werden. Die Raum-zeitliche Tiefenwanderung der Seismizität der früheren Lokalisierung konnte bestätigt werden.

Für ausgewählte Cluster und Einzelereignisse wurden auf Grundlage der Polaritäten der Phasen P, SH und SV Herdmechanismen bestimmt. Hierzu wurden in einem Jackknife-Verfahren aus jedem Polaritäten-Datensatz neue Datensätze erzeugt, in denen jeweils eine Polaritätsbeobachtung des ursprünglichen Datensatzes weggelassen wurde. Für alle so erzeugten Datensätze eines Ereignisses oder Clusters wurde mögliche Herdmechanismen errechnet. Die Summe aller möglichen Herdmechanismen mit weniger als zwei Polaritätsfehlern und mindestens zwölf Beobachtungen wurde einer statistischen Analyse unterzogen und durch Mittelung der Normalenvektoren der Herdflächen, die bevorzugten Herdmechanismen und deren Varianz berechnet. Insgesamt konnten 25 Herdmechanismen mit einer Varianz kleiner als 20° gefunden werden.

Die Anzahl der abgeleiteten Mechanismen ist zu gering, um eindeutige Aussagen über die tektonischen Vorgänge im Raum Bad Reichenhall machen zu können. Sie scheinen jedoch anzudeuten, dass der Saalach Westbruch Einfluss auf das Spannungsregime des Untersuchungsgebiet hat. Entlang dieser Störung verschob sich seit dem mittleren Oligozän die Berchtesgadener Masse um 12-15 km nach Nordosten. Die errechneten Herdmechanismen lassen sich in drei Spannungsregime gliedern, die mit einer links-lateralen Verschiebung am Saalach-Westbruch in Einklang zu bringen sind. Sollte sich dieses Ergebnis durch zukünftige Untersuchungen bestätigen, könnte dies große Auswirkungen auf die seismische Gefährdungsanalyse für die Städte Bad Reichenhall und Salzburg haben, die sehr nahe an der Störung liegen.

Im letzten Schritt wurde das raum-zeitliche Muster der relokalierten Seismizität mit Hilfe eines statistisch-hydrodynamischen Modelles untersucht. Die beobachtete Seismizität wurde als stochastischer Punktprozess modelliert, welcher durch eine konditionelle Intensitätsfunktion beschrieben werden kann. Diese stellt vereinfacht gesagt die sich aus einem parametrisierten physikalischen Modell unter der Bedingung der bekannten, vorangegangenen Seismizität ergebende Ereignisrate an. Durch Maximierung der sich aus der Intensitätsfunktion ergebenden Wahrscheinlichkeitsfunktion

können die optimalen Modellparameter abgeleitet werden.

Die Intensitätsfunktion des modellierten Punktprozesses setzte sich aus einem konstanten Hintergrundterm und einem Porendruckterm zusammen. Letzterer gibt die Erdbebenrate an, die aus der niederschlagsbedingten Porendruckänderung in der Tiefe eines poroelastischen homogenen Halbraumes vom Rate-and-State Reibungsgesetz vorhergesagt wird. Diese Gesetz ist aus Laborversuchen abgeleitet und beschreibt die Abhängigkeit des Reibungskoeffizienten einer Bruchfläche von deren Verschiebungsbetrag, -rate und der Ruhekontaktzeit.

Die aus dem optimierten Modell berechneten raum-zeitlichen Felder für Porendruck und Erdbebenrate stimmen sehr gut mit der beobachteten Seismizität überein. Die daraus vorhergesagte tägliche Erdbebenzahl wurde mit Hilfe der Kreuzkorrelation mit der beobachteten täglichen Erdbebenrate verglichen. Dabei wurde ein sehr hoher Korrelationskoeffizient von 0.82 ermittelt, der eine gute Anpassung des zugrunde liegenden Modelles anzeigt. Die berechneten absoluten Porendrücke im Tiefenbereich von 1-4 km liegen zwischen 5-13 mbar. Diese sind um Größenordnungen kleiner als üblicherweise bei Druckversuchen in Bohrlöchern oder bei Staudamm-induzierter Seismizität beobachtet (1-100 bar) und zeigen, dass die Erdkruste in manchen Bereichen in einem so kritischen Zustand sein kann, dass minimale Störungen ausreichen um Erdbeben zu verursachen.

Abschließend kann festgestellt werden, dass es gelungen ist, einen eindeutigen Zusammenhang zwischen niederschlagsbedingten Porendruckänderungen und den Schwarmbeben am Hochstaufen bei Bad Reichenhall nachzuweisen. Berücksichtigt man, dass die Beben in einem sehr kleinen Herdvolumen stattfinden, fast jährlich auftreten und von einem dichten seismo-meteorologischen Messnetz permanent überwacht werden, erweist sich das Hochstaufen-Massiv als eine nahezu laborartige Forschungsumgebung zum Studium von Schwarmbeben und fluid-getriggelter Seismizität.

Summary

This thesis addresses to self-contained topics and is therefore structured in two parts. The first part describes the installation of a new seismological network for Bavaria, whereas the second part focuses on the investigation of rainfall induced seismicity near Bad Reichenhall in southeastern Bavaria.

Part 1

Because of the focus of the existing seismological stations on teleseismic and regional events, the capability of locating local earthquakes in various regions of Bavaria was quite limited. To overcome this situation 15 new stations were installed in the country. Additionally, six existing stations were updated to state-of-the-art technology in a second stage. The network geometry closely oriented on the seismicity of Bavaria, with densely spaced stations in areas where activity is high and promising scientific problems could be addressed. The software concept was, as far as possible, adopted from the GEOFON Project of the GeoForschungsZentrum Potsdam (GFZ), which is already used for the German Regional Seismic Network (GRSN) and other European networks. This assures an easy data transfer with other services and allows the future incorporation of real-time data of the Bavarian network in an European and global seismological networks.

Part 2

In the second part of this thesis, the focus will be laid on one of the dense sub-networks in southeastern Bavaria. Here, near the town of Bad Reichenhall, a connection between rainfall and seismicity is suggested since the early 1970ties. However, because of the lack of continuous high-quality data such a correlation could never be tested by means of a physical model. In three papers the observation of above average rainfall in 2002 and associated earthquake swarms are studied in detail. Starting with an overview paper

with first location results and interpretation in Chapter 3, the discussion of cluster analysis, high-precision relocation and focal-mechanism analysis in Chapter 4 and finally by statistical modeling of the relocated seismicity by means of point process modeling and pore-pressure diffusion assuming a rate-state earthquake friction model in Chapter 5.

Although, seasonal variability of seismicity related to ground water recharge and precipitation has been previously observed on regional scales, a statistically significant causal relationship between rainfall and earthquake activity for an isolated region can be shown here for the first time. The analysis of the high quality meteorological and seismic data in the Mt. Hochstaufen region yields clear evidence that tiny pore pressure changes induced by rainfall are able to trigger earthquake activity even at 4 km depth via the mechanism of fluid diffusion. Stress changes of the order of 5-13 mbar are found to trigger earthquakes. This is much less than usually produced in fluid injection experiments (several 100 bars and more), indicating an extreme sensitivity of the crust with regard to tiny changes. This might be an universal feature which can, however, only be seen in the rare occasion of an isolated but critical system, like the study area.

Although, the derived focal mechanisms indicate an influence of the Saalach Fault Zone on the stress regime of the study area, the reason for the criticality of the seismogenic volume in the Mt. Hochstaufen region is not yet finally resolved. However, the high correlation between rainfall-induced pressure changes at depth and seismicity opens the possibility of forecasting future earthquake rates on the basis of rainfall data in this region. Regarding the small volume in which the earthquakes take place, the almost yearly occurring earthquake swarms and the permanent, seismo-meteorological monitoring network, Mt. Hochstaufen provides nearly controlled experimental conditions to study fluid-induced seismicity and the physics of earthquake swarms.

Part I

**A New Seismological Network
for Bavaria**

Chapter 1

History of Seismology in Bavaria

To motivate the necessity of a new modern seismological network for Bavaria, this chapter reviews the history of seismology in Bavaria. It begins with a brief outline of pre-instrumental observations and continues with the installation of the first seismometer in Munich in 1905 as well as further auxiliary stations in several Bavarian cities shortly after. Starting in 1955, the Bavarian seismological network was continuously expanded, including also stations in Austria. Additionally, several temporal and permanent seismological networks and arrays were installed in Bavaria. Some had major influence not only on the history of seismology in Bavaria and will briefly be introduced here. Thereafter, the demand for a modern seismological network in Bavaria is demonstrated, considering the example of the M 3.2 Berchtesgaden earthquake of May 12, 2000.

1.1 The Bavarian Earthquake Service

Profiting from the invention of the art of printing with moveable metallic letters by J. Gutenberg in about 1450, an invasion of illustrated broadsheets and chronicles of all kinds began to appear in Germany. This introduced a rapid and effective way to distribute news, including reports on felt earthquakes [Grünthal, 2004]. Yet, the first printed earthquake report known in Germany was published by an unknown Bavarian writer in Munich [Günther, 1890], addressing the strong 1511 Slovenia-Friuli-Venezia earthquake and printed shortly after.

Up to the 18th century earthquakes were seen as heavenly chastisement by most of the people of Europe. In the German speaking countries, Alexan-

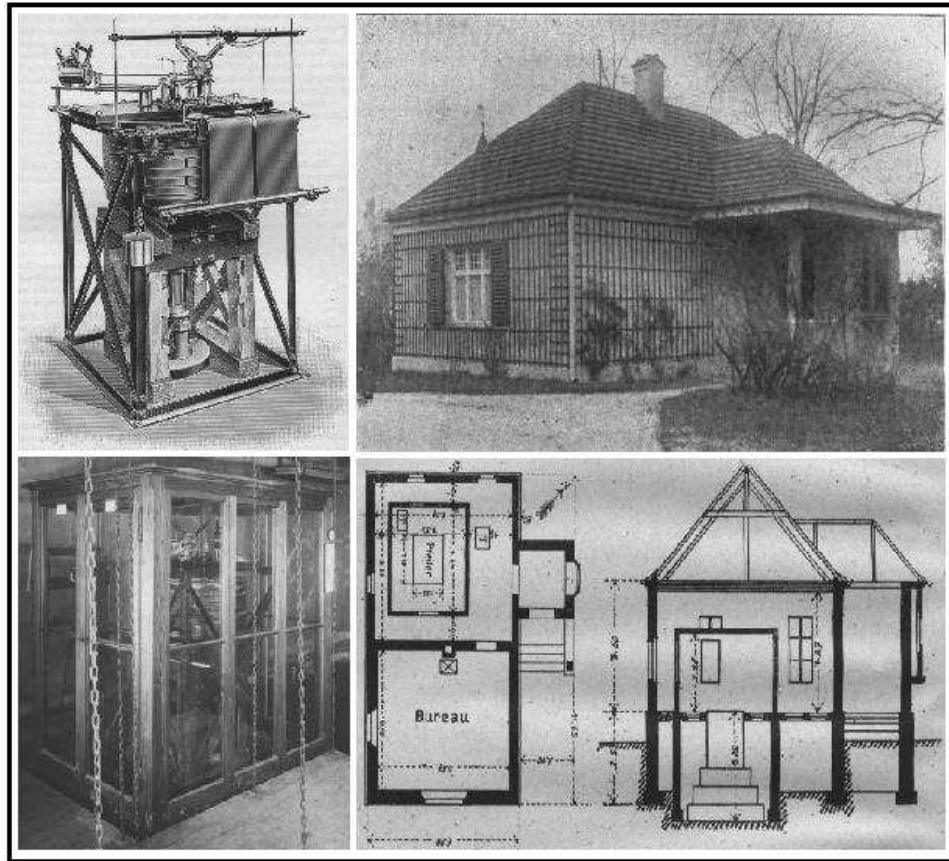


Figure 1.1: "Earthquake House" at the Royal Astronomical Observatory in Munich. Upper left) A illustration of the 1200 kg Wichert Seismograph. Upper right) View of the "Earthquake House" from outside. Lower left) View into the "Earthquake House" with hanging flours and seismometer housing. Lower right) Plan of the "Earthquake House".

der v. Humboldt (1769-1859) laid the foundation for the scientific observation of earthquakes. His opinion, that earthquakes were directly connected to volcanic activity [*Humboldt*, 1845–1861], was shared by many researchers up to the middle of the 19th century. Contrarily, Otto Vogler (1822-1897) introduced the collapse theory [*Volger*, 1857–1858], which caused controversy between scientists supporting Neptunism, following his idea, and Plutonism, which favored the Humboldtian view. Observing correlation between elongated areas of equal macroseismic intensity and geologically observed fault and fracture zones known in the Alps, Albert Heim (1849-1937) formulated the thesis of earthquakes being linked to the processes of mountain building [*Heim*, 1878]. Heim was one of the founders of the Swiss Seismological Commission in 1887, whose successful work stimulated the foundation of similar organisations in the rest of Europe [*Wielandt*, 1997].

The International Seismological Association, founded in 1903 in Strasbourg, suggested to build seismological services in all countries of the German Empire. Thereupon, the Bavarian Academy of Science submitted an accordant proposal to the Royal Bavarian Government, which was accepted in July 1904. A 1200 kg Wiechert seismometer was installed on August 2, 1905 at the Royal Astronomical Observatory in Munich-Bogenhausen, where also the geomagnetic observatory resided since 1840 (comp. Fig. 1.1). Here, J. v. Lamont (1805-1879), the originator of geomagnetic observations in Bavaria, had already observed several teleseismic events on his magnetometers. He also suggested the construction of a seismometer long before Filippo Cecchi (1822-1887) finally invented it in 1875 in Italy.

First investigation of earthquake occurrence in Bavaria were accomplished on basis of macroseismic and historic data [Gümbel, 1889; Günther, 1890; Gümbel, 1898; Reindl, 1902-1903, 1903; Günther and Reindl, 1903; Reindl, 1905a,b] and continued by Messerschmitt [1907], Lutz [1921], Giessberger [1922], which were then able to include first recordings of the Munich seismometer [see also Schweitzer and Lee, 2003]. Between 1909 and 1932 three auxiliary stations were installed in Hof (1909-1919), to monitor the earthquake swarm region in Vogtland; in Nördlingen (1912-1932), to study the origin of the Nördlinger Ries; and in Hausham (1914-1923), where a coal mine was monitored. The main station in Munich was operated by C. W. Lutz until 1944, when he retired and no successor was found in the confusion of World War II. All seismological stations up to this time recorded on smoked paper, which are still available today in the archive of the Geophysical Observatory of the University of Munich.

After intermediate installation in the cellar of the newly founded Institute of Geophysics in Munich, between 1955 and 1958, the Bavarian seismological main station was moved to Fürstenfeldbruck. Here, it again joined the geomagnetic observatory, which moved to this place in 1937. Led by O. Förtsch the regular operation of the seismological station started again in August 1965 with three long-period Sprengnether instruments and photo-optical registration. He also reinstalled the station in Hof in 1955, which was in operation until 2000, and started to install several stations in Garmisch-Partenkirchen, Bad Reichenhall and the Austrian Alps in the 1970ies. With the exception of Fürstenfeldbruck, all stations were equipped with ink-recording units. Seismograms were sent by mail on a weekly basis to the Geophysical Observatory in Fürstenfeldbruck where they were analyzed.

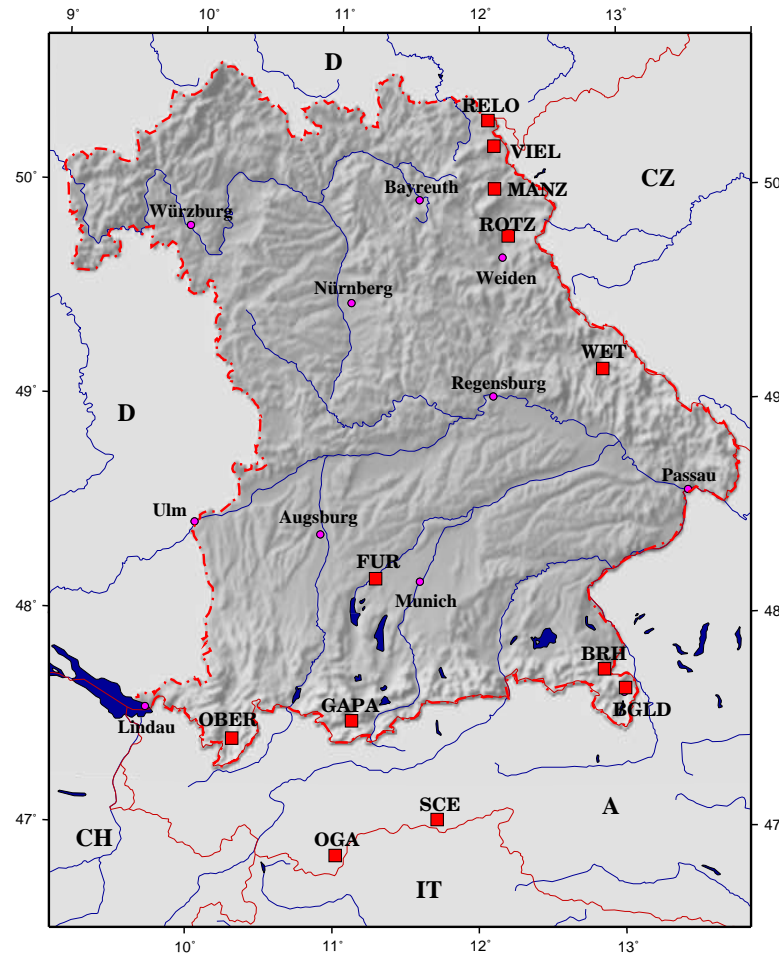


Figure 1.2: Map of the Bavarian seismological network in the end of 2000. Stations are indicated by red squares. Major cities and political borders are given. The territory of Bavaria is highlighted by topography.

Förtsch also initiated the installation of temporal seismological networks to study local seismicity [e.g., *Koschyk, 1973*], which was continued after E. Schmedes took over the Bavarian Earthquake Service in 1976 [e.g., *Gebrande et al., 1977; Nöthen, 1981; Schwarzmann, 1996*]. Schmedes expanded the Network further and installed stations in Viellitz, Manzenberg and Rotzenmühle (NE-Bavaria), in Oberstdorf and Berchtesgaden (S-Bavaria), as well as in Obergurgl and at the Schlegeis reservoir (Austria). A map of the seismological network in the end of 2000 can be found in Figure 1.2.

Until the beginning of 2001, most of the stations were running in trigger mode. This means the recording was only stored on hard disk if a simple

detection algorithm identified an event. However, as anthropogenic seismic noise often has similar characteristics as local earthquake signals, the fine-tuning of such algorithms is difficult. They often represent a compromise between most complete earthquake recording and hard disk storage capability. This means, that on the one hand many recorded events represent noise and on the other hand many local earthquakes may be missed. Furthermore, since at least four observations are needed to be able to invert for the earthquakes location and source time, the sparseness of the network prohibited even an approximate location in some cases.

1.2 Other Seismological Networks in Bavaria

Several other networks have been installed temporarily or permanently in Bavaria. In the majority of the cases the Bavarian Seismological Service was closely involved in the installation, maintenance of the stations and the analysis of the recorded data. Four of these networks, which were the most important for national and international seismology, will be briefly introduced in the following.

1.2.1 Seismological Central Observatory Gräfenberg

In 1959 the U.S. Department of Defense initiated the program VELA UNIFORM, for better detection of underground nuclear explosions. Part of the program was to adapt the array technique, developed in radar and radio astronomy, for seismology. This technique combines several sensors to an antenna and uses signal processing techniques to focus on arbitrary observation directions. In July 1963, a cross-shaped network of 3km diameter was installed near Gräfenberg in Central-Bavaria. It consisted of seven vertical Benioff seismometers in its arms, and a three-component Sprengnether broadband instrumentation as center station. The aim of the array was to detect nuclear explosions at the Nevada Test Site, U.S.A. Starting in 1965, the three German institutions Scientific Council Physics of the Earth (FKPE), Institute for Geosciences and Natural Resources (BGR) and German Science Foundation (DFG) took responsibility for the array, which had also become an important tool for seismological research.

In 1967, the array was reconfigured to triangular shape and a Seismological Central Observatory (SZGRF) was installed in Haidhof near Gräfenberg.

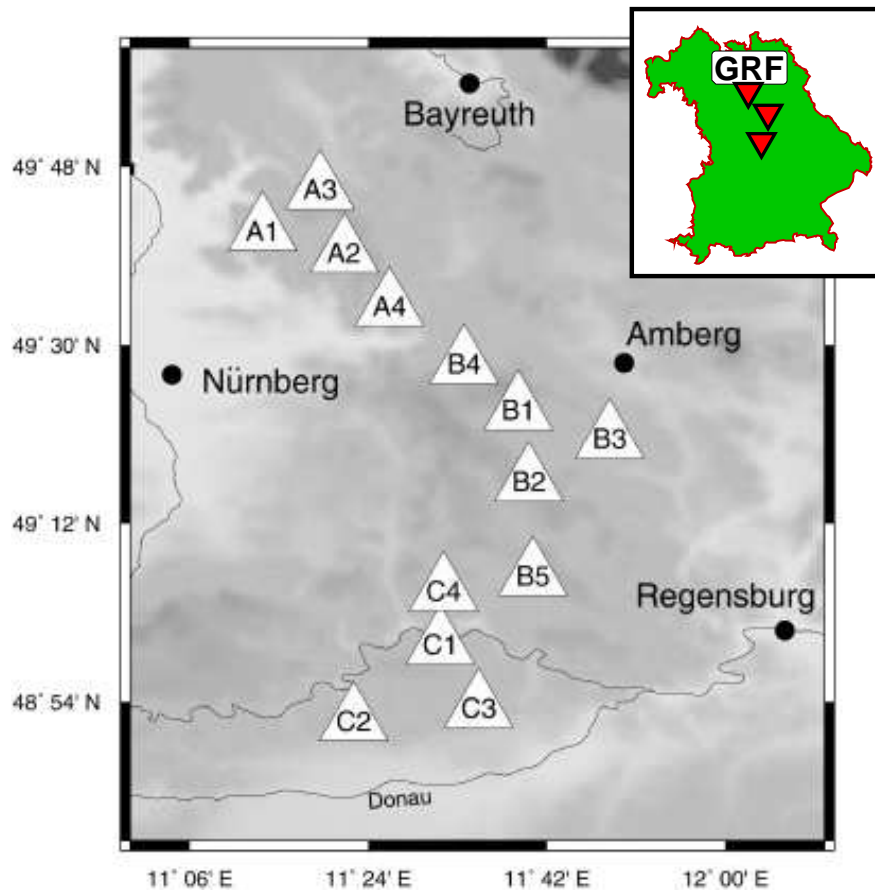


Figure 1.3: Map of the Gräfenberg-Array (GRF) [mod. from *Rothert and Ritter, 2000*]. Three-component stations are A1, B1, and C1. Their location is also shown in the insert map. The others stations are vertical-component stations.

Between 1976 and 1980 the Gräfenberg-Array (GRF) was expanded to a L-shaped broadband array, consisting of 13 stations with Streckeisen STS-1 seismometers, which were purpose-designed by E. Wielandt to meet the high demands on the linearity of the instrument characteristic [*Wielandt and Streckeisen, 1982*].

In the following ten years the GRF defined the state-of-the-art of digital broadband seismology. Today, the datacenter of the SZGRF is located in Erlangen (C-Bavaria), where most of the data can be accessed via internet (www.szgrf-bgr.de). More detailed information and further references can be found in *Seidl and Aichele [1997]*. Figure 1.3 shows a location map of the present configuration of the GRF.

1.2.2 German Continental Deep Drilling Program

In 1987 the German Continental Deep Drilling Program (KTB) was started near Windischeschenbach NE-Bavaria. KTB was designed to study the properties and processes of the deeper continental crust by means of a super-deep borehole, reaching a depth of 9.1 km. A seismological network (KTB-Net) of 25 km aperture, consisting of four Steckeisen STS-2 broadband seismometer stations with 20 bit digital recording, was installed around the KTB site in 1991 to monitor the local seismicity and scientific experiments [e.g., *Dahlheim et al.*, 1997; *Emmermann and Lauterjung*, 1997]. Maintenance of the network and data analysis was provided by the University of Munich. When the KTB project ended in 1995, the Bavarian Seismological Service integrated the KTB-Net into its network leaving one station at its original locations and reinstalled the three others at different locations in Bavaria. A map of the KTB-Net can be found in Figure 1.4

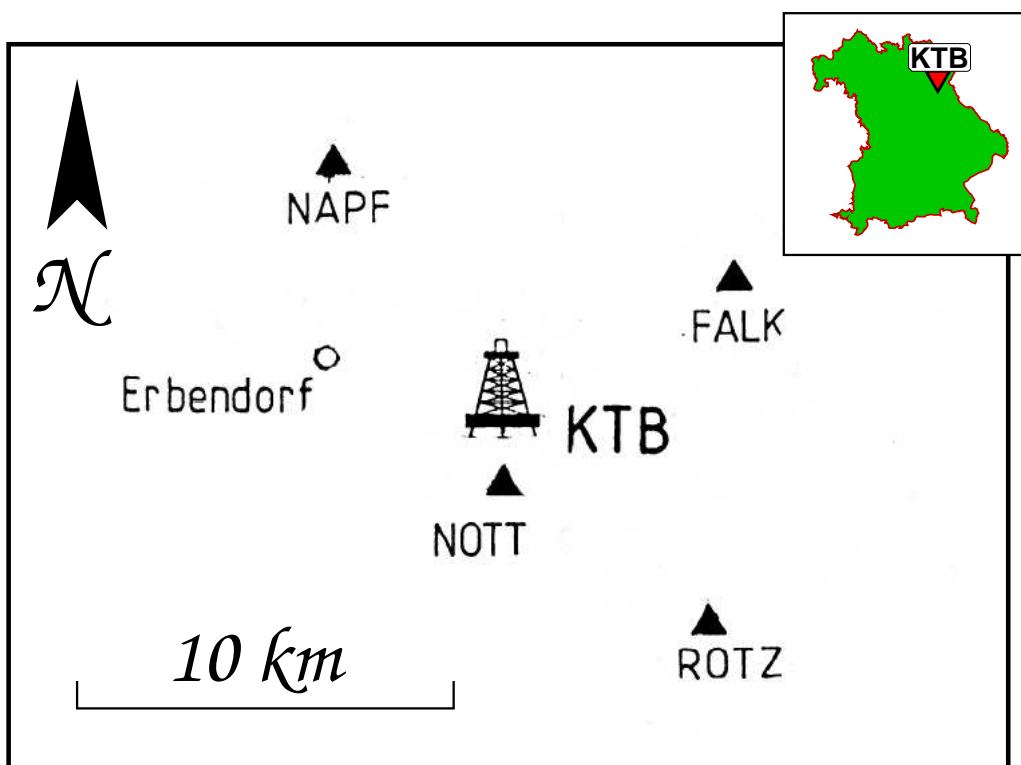


Figure 1.4: Map of seismological network of the German Continental Deep Drilling Program (KTB-Net) [mod. from *Dahlheim et al.*, 1997]. Insertmap shows the location of the KTB-drilling site.

1.2.3 German Regional Seismic Network

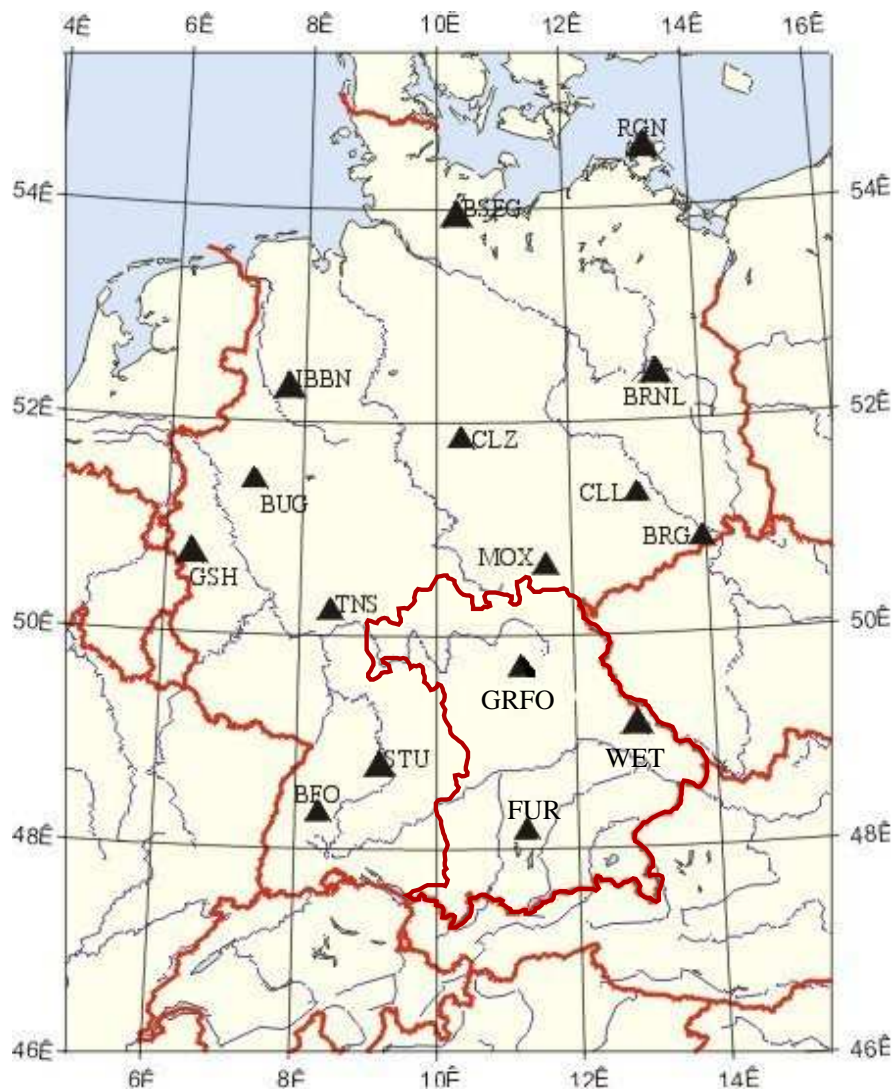


Figure 1.5: Map of the German Regional Seismic Network (GRSN). Stations GRFO, WET and FUR are located in Bavaria. Political borders are indicated by red lines.

In 1991 the German Regional network (GRSN), consisting of 14 identical broadband stations, was installed in Germany. GRSN was a joint research project of BGR and geophysical institutes of German universities and was funded by the DFG. It was planned as an extension of the GRF. In addition, the GRSN can be regarded as the German contribution to international initiatives aimed at the establishment of modern digital seismic broadband networks on a regional and global scale. All GRSN stations have identical instrumentation, consisting of Steckisen STS-2 broadband seismometers with

24 bit digital recording, and are evenly distributed over Germany. Three stations in Gräfenberg (GRFO), Fürstenfeldbruck (FUR) and Wetzell (WET) are located in Bavaria. The latter two are maintained by the Bavarian Seismological Service. The data center of the GRSN is located at the SZGRF in Erlangen and can be accessed via internet (www.szgrf-bgr.de). A map of the GRSN is shown in Figure 1.5.

1.2.4 German Experimental Seismic System

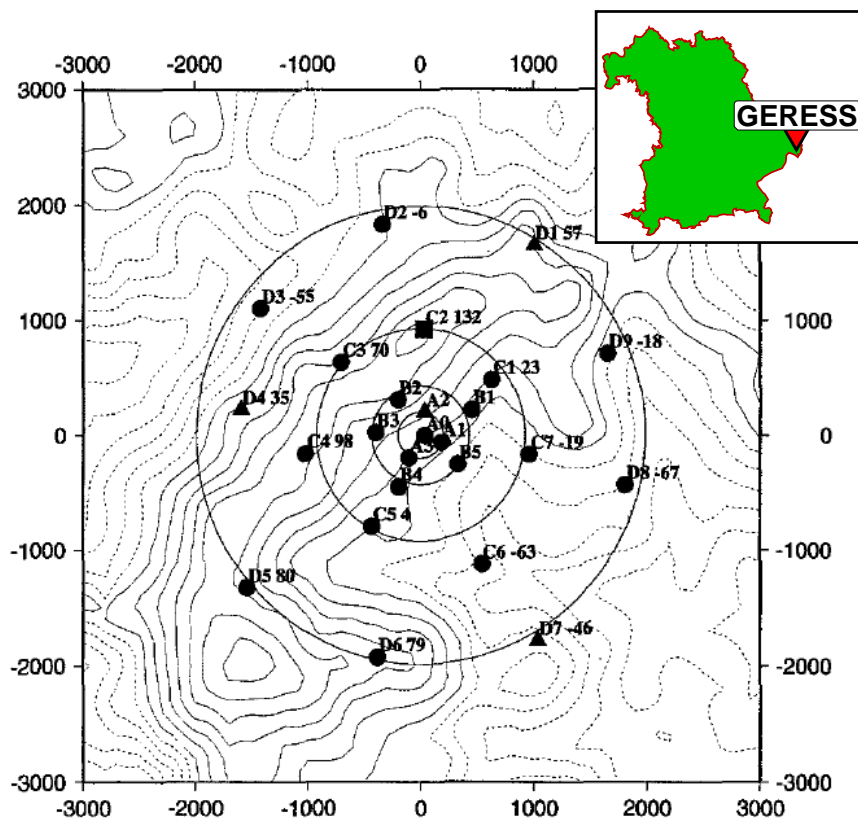


Figure 1.6: Station locations of the GERESS array in Southeastern Germany. Filled circles show the 25 vertical short-period instruments, triangles and rectangles show the three-component instruments. Topographic variation across the array of about 200 m is shown by contour lines (increment of 25 m), with dashed lines for elevations below 1000 m.

The German Experimental Seismic System (GERESS) is one of the most sensitive seismic systems in central Europe. The array is located in the Bavarian Forest (CE-Bavaria) and consists of a total of 25 seismograph stations, which are distributed around a center point on four concentric circles with a

maximum radius of 2 km (Fig. 1.6). GERESS has primarily been designed for the detection of weak signals from earthquakes and underground nuclear explosions. The monitoring capability of GERESS is used to automatically detect and locate seismic events in Germany and adjacent areas. Seismological data can be ordered online [Harjes, 1990].

1.3 Motivation for a New Bavarian Network

As outlined in the previous sections, the seismological network in Bavaria until the end of 2000 was mainly suited to observe teleseismic and regional earthquakes. This was on the one hand due to the fact, that a major part of the seismological stations had too low sampling rates to adequately record local seismicity. On the other hand, short-period stations suitable for recording local events, did not allow the derivation of reliable location in near real time, because of the low station density and their non-continuous recording. Additionally, fast estimation of the local seismic activity was hardly possible, because of the delayed data transfer.

This became clear, when in the afternoon (15:16 local time) of Friday, May 12, 2000, a $m_l=3.2$ earthquake occurred in Berchtesgaden (SE-Bavaria) and was felt by many local residents. Numerous telephone calls reached the police in the area of Berchtesgaden and Bad Reichenhall, reporting on noticeable ground motion and minor damages. Because of the lack of defined information paths the Geophysical Observatory in Fürstfeldbruck was informed about the earthquake occurrence only after nearly one hour. After that it took further 15 minutes to download the data from the available two stations in the area and estimate the location and strength of the event. Up to this time it was not absolutely clear if the event happened in Bavaria or in a neighboring country.

The Berchtesgaden earthquake, although very small, did reveal the necessity of a modern seismological network in Bavaria, which is suitable for the detection of local seismicity down to a magnitude of at least $m_l=2.0$ in near-real time. Further, the definition of unequivocal information paths between authorities and Seismological Service turned out to be of paramount importance. Consequently, Prof. H. Igel of the University of Munich and the Bavarian Geological Survey proposed a project to install a modern seismological network to the Bavarian government. The key issues of the project were: (1) to update the instrumentation of the Bavarian seismological net-

work to record local events with high resolution, (2) to increase the station density in areas of permanent seismic activity to be able to get reliable earthquake location and magnitude, (3) to install a data center at the Geophysical Observatory in Fürstfeldbruck to store and analyze data, and (4) to develop an infrastructure for the information of authorities and the public.

The Bavarian Ministry for the Environment founded the proposed project in October 2000. Thereupon, the Bavarian Seismological Network (**BayernNetz**) was installed in two steps. Following the grant of 250,000 € by the Bavarian State 15 new stations were installed. After a $m_l=5.3$ earthquake in northern-Italy was felt in great parts of southern-Bavaria on July 17, 2001, an additional grant of the Bavarian State allowed the update of six existing stations to the new state-of-the-art instrumentation.

The installation of the network and the development of necessary software was accomplished by the author in cooperation with members of the Geophysical Observatory of University of Munich and will be described in the following chapter.

Chapter 2

A New Bavarian Seismological Network

In this chapter the new Seismological Network of Bavaria is introduced. Since the geometry of the network is strongly orientated on the seismicity, it will be briefly reviewed together with the geology of Bavaria. After that, the design of the individual seismological stations and of the data center in the Geophysical Observatory in Fürstenfeldbruck is described in terms of hard- and software. Further, data transfer and storage are discussed. Finally, the presentation of the near-realtime data in the internet is described and the design of two information centers in S- and N-Bavaria is introduced.

2.1 Network Geometry and Seismicity

Before giving a short overview of the Bavarian seismicity a very brief description of the geology of the country, based on *Frank* [1996], will be given. The geological map of Bavaria, which is shown in Figure 2.1, can be divided in four major parts: the northern Bavarian basal and overburden complexes north of Danube, and the Molasse Basin and the Alps south of the Danube. A special feature is the impact structure of the Nördlinger Ries in western Bavaria.

The Variscian basal complex outcrops in NE-Bavaria and is composed of granitic and metamorphic rocks. It builds the basement below all other geological complexes and varies in depth from a few hundred meters in the Vindelician Swell (C-Bavaria) to over 5000 m in the southern Molasse Basin. Overlaying the basal complex, the overburden complex is mainly outcropping in NW-Bavaria and is built up by sedimentary rock of Paleozoic to Meso-

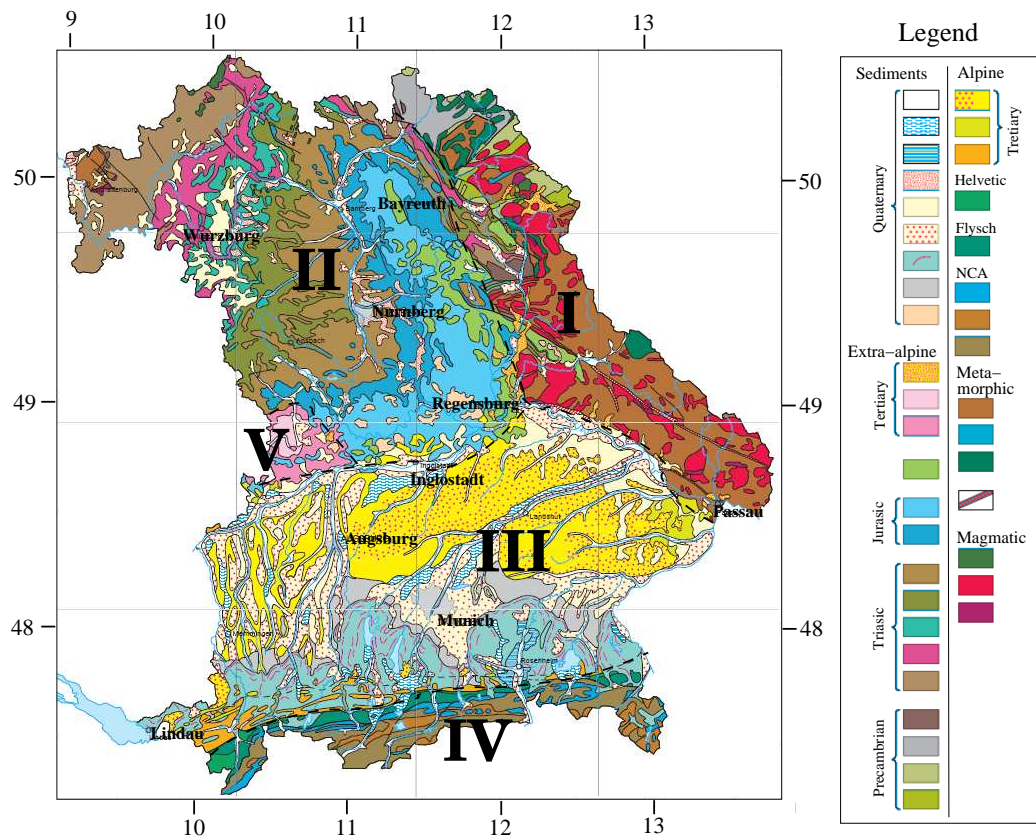


Figure 2.1: Geological map of Bavaria. Four main parts can be distinguished: the northern Bavarian basal (I) and overburden complexes (II) north of Danube, and the Molasse Basin (III) and the Alps (IV) south of the Danube. A special feature is the Ries impact structure (V). [mod. from *GLA-Bayern*, 1998]

zoic age. A prominent member of this complex is the Franconian Jurassic. The Molasse Basin developed in more than 30 Ma through sedimentation from the rising Alps into a subsiding basin structure reaching a thickness of over 5000 m. The southern part of the Molasse is tectonically influenced by the northward movement of the Alps. Their geological subunits Flysch, Helveticum and Northern Calcareous Alps outcrop in southern Bavaria. A special feature of the Bavarian geology is the 15 Ma old impact structure of the Nördlinger Ries with its circular crater of about 20 km diameter.

The seismicity of Bavaria, as it is known up to date, mainly concentrates in three of the geological complexes introduced above. As shown in Figure 2.2 these are the basal complex, the overburden complexes and the Alps, whereas the Molasse Basin is characterized by relatively low seismicity.

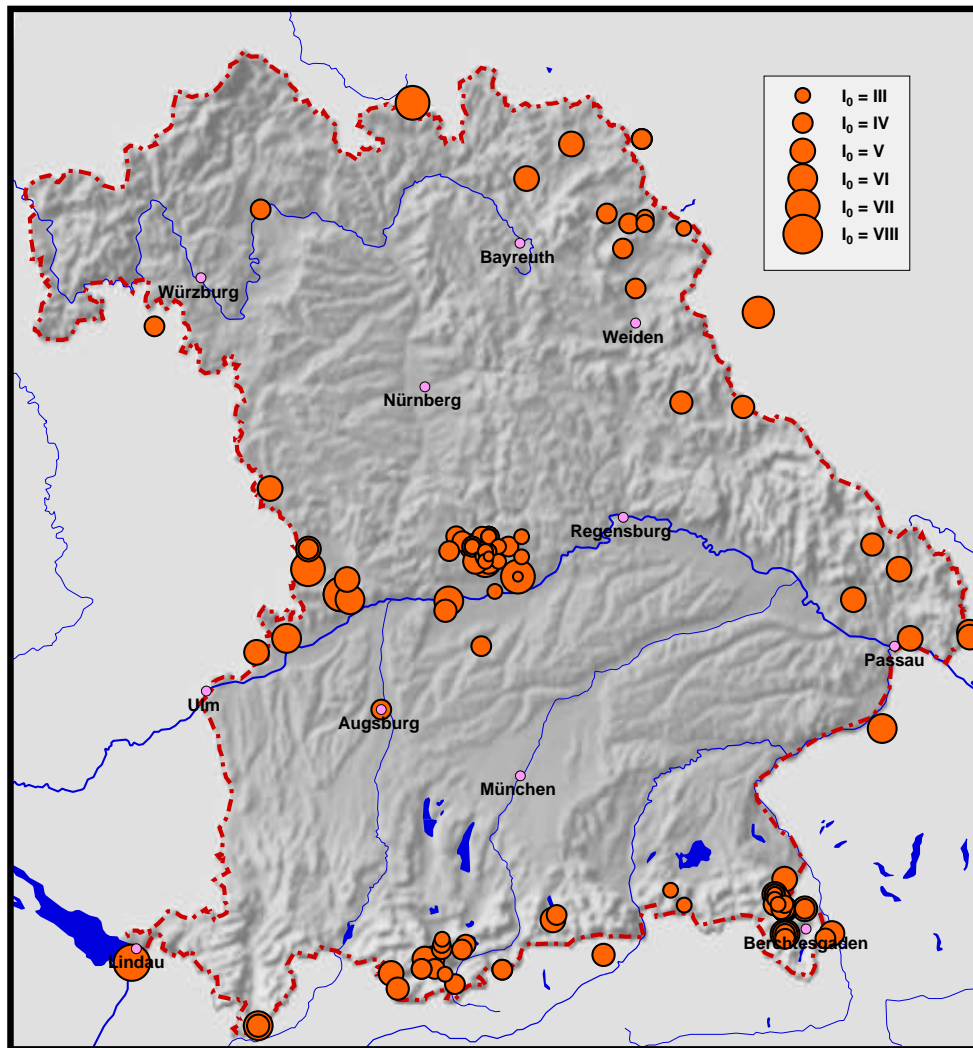


Figure 2.2: Map of earthquakes felt in Bavaria (1000-2002). Circles give the location and the macroseismic intensity [Medvedev *et al.*, 1965] of the events.

The most active region is the Vogtland in NE-Bavaria, where macroseismic intensities¹ of IV were reached. However, the seismicity is mainly concentrated on the territory of the Czech Republic, where the east-west striking Eger rift intersects with the north-south striking Marianske-Lazne fault system forming a zone of weakness in Earth's crust with Tertiary volcanism (comp. Fig. 2.3). Mantle-derived fluids reach the surface in numerous moffettes [Bräuer *et al.*, 2003] in the area up to date. The term "earthquake swarm" was used for the first time in an article on earthquake sequences in the Vogtland by Knett [1899] [for a review on earthquake swarms see e.g. Spicak, 2000; Kurz *et al.*, 2003]. A second area in the north

¹Macroseismic intensity denotes how strongly an earthquake affects a specific place. The Bavarian earthquake catalog is based on the MSK64 scale [Medvedev *et al.*, 1965]

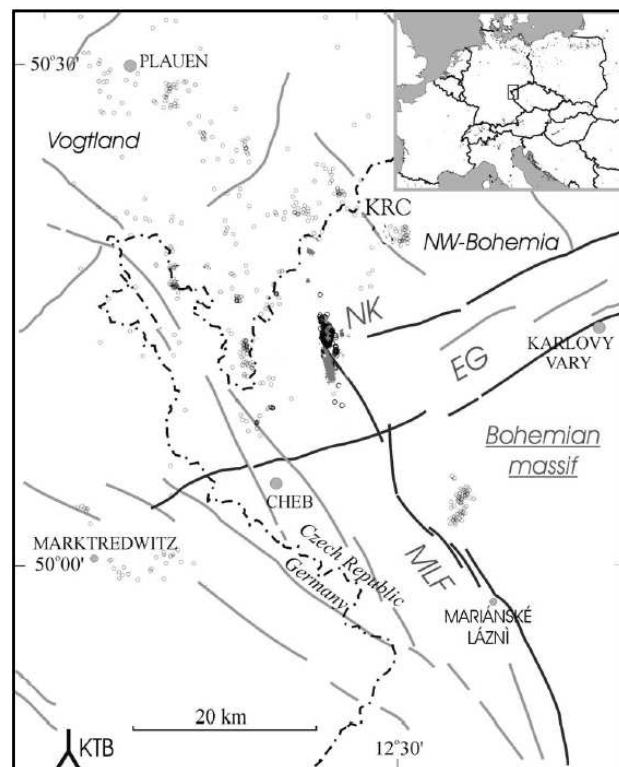


Figure 2.3: Earthquake swarm region of Vogtland/Western Bohemia. Circles denote epicenters of microearthquakes in the period 1991–1999, and by gray crosses for a swarm in 2000. Fault systems are denoted as MLF (Mariánské Lázně fault) and EG (Eger rift) [mod. from *Fischer, 2003*].

of Bavaria, of low seismicity however, is Hohe Rhön with very rare events reaching intensities of only III. No explanation for this activity can be given so far.

In the central part of Bavaria seismicity is concentrated on the southern Franconian Jurassic. Especially the Valley of the Altmühl river has experienced earthquakes of intensity up to VII between the 1914 and 1915. These earthquakes were among the first recorded after the installation of the first Seismometers in Bavaria and are the strongest events known in Bavaria. A likely explanation for this activity might be cavity collapse in Karst, which can be found in this region. Further west the impact structure of the Nördlinger Ries and to the east the area around the city of Passau shows weak activity (intensities III-IV, comp. Fig. 2.2).

The northern margin of the Alps forms a nearly continuous band of seismicity in the South of Bavaria. Concentrations of activity can be seen near the cities of Oberstdorf, Garmisch-Partenkirchen and Bad-Reichenhall.

The latter is further characterized by the occurrence of earthquake swarms, which correlate with above average rainfall events. This phenomenon will be studied in the second part of this work.

The strongest earthquakes in the historic earthquake catalog of Bavaria is an intensity VII-VIII event near the city of Lindau on December 20, 1720. However, a recent revision of the historical sources did point out, that the epicenter was located further west on Swiss territory near the city of Arbon/St.Gallen [SED, 2002].

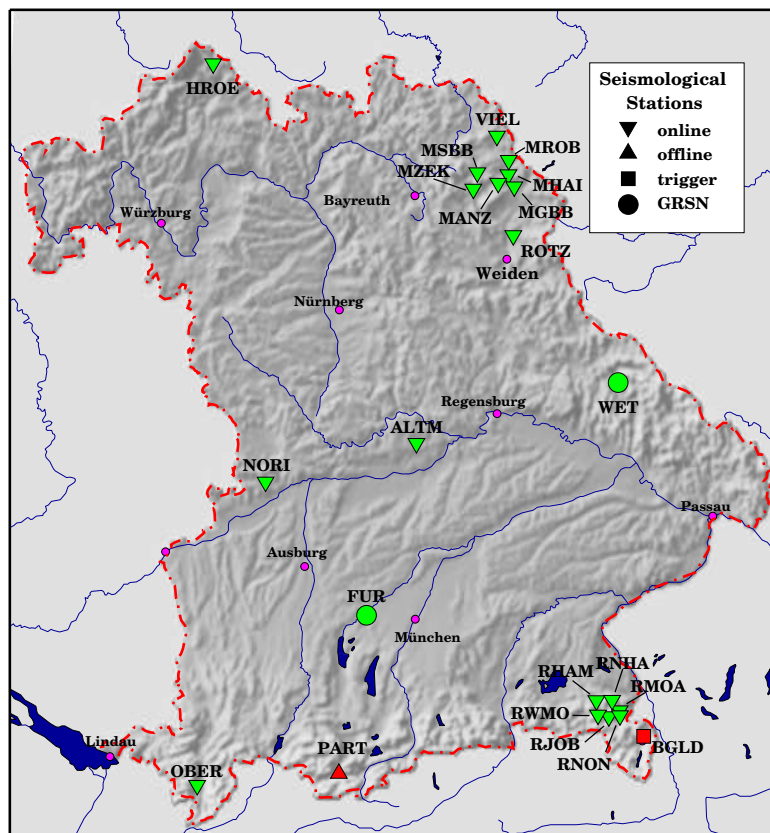


Figure 2.4: Map of the new Bavarian Seismological Network (BayernNetz). Station locations are indicated by symbols explained in the figure. A list of all stations can be found in Table A.1. Individual station sheets with geological maps are collected in Appendix A.

The geometry of the new Bavarian Seismological Network is shown in Figure 2.4. As mentioned above, the network layout is closely oriented on the seismicity. Subnetworks were installed in northern Bavaria around Marktredwitz and in southern Bavaria near Bad Reichenhall to study the phenomenon of earthquake swarms, which occur in these regions. The northern subnetwork consists of five new stations near the city of Marktredwitz

and has an aperture of about 20 km. Additionally, three existing stations in the wider vicinity were updated to the new instrumentation. The southern subnetwork, with a diameter of about 10 km, consists of five new and one updated stations. An existing station in Berchtesgaden, in about 20 km distance, could not be updated because of its vulnerability to lightning strike. Unfortunately, no alternative station site could be identified so far.

Further, single stations were build up in northern Bavaria near Fladungen in the Hohe Rhön, as well as in central Bavaria near Bissingen in the Nördlinger Ries, and near Beilngreis in the Altmühl Valley. Moreover, one station was installed near Oberstdorf (SW-Bavaria) and one updated near Garmisch-Partenkirchen (S-Bavaria). For the latter station, however, no telephone connection could be installed due to interdiction by the landlord. An alternative station location could not be found so far.

Most of the stations were installed in elevated water reservoirs. These sites supply communities with drinking water and offer the infrastructure needed for the installation of the instrumentation. These are electric power supply, lightning protection, and pilot wires which can be used to connect to the public telephone system. Additionally, most of these reservoirs are built under ground, in remote, elevated places and thus offer acceptable sensor-ground coupling and noise conditions. A description of all stations with geological location maps is given in Appendix A.

2.2 Technical Station Design

In the following the design of the seismological station of the Bavarian Seismological Network (**BayernNetz**) is described. First the acquisition hardware, which is identical for all stations, is introduced. This is followed by a presentation of the two sensor types that are in operation in the BayernNetz. Finally, the acquisition software *SeisComP* and additional LINUX-based utilities, necessary for operation and data handling, are discussed.

The technical design of the seismological station of the **BayernNetz** is adopted from the GEOFON project [*Hanka and Kind, 1994*], developed by the GeoForschungsZentrum Potsdam (GFZ), Germany's National Research Center for Geosciences. The flexible, modular and economic concept has experienced a widespread usage in seismological networks in Europe and the

world. To profit from future soft and hardware developments within the GEOFON-community, it was decided to use this concept for the **Bayern-Netz**.

2.2.1 Hardware

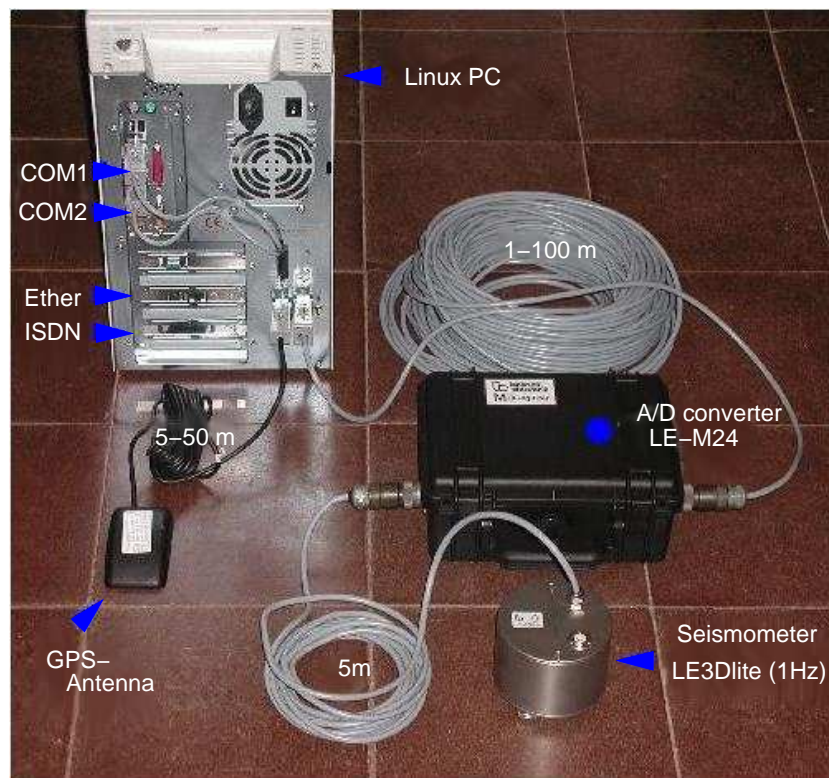
The basic components of a seismological station of the **BayernNetz** are shown in Figure 2.5a. An off-the-shelf Personal Computer (PC) operated by LINUX [Torvalds, 1997], an open-source operating system, is the central unit of the station hardware. Connected via serial link, the core seismological hardware consists of an analog-digital converter and a seismometer. Timing is provided by a Global Positioning System (GPS) receiver, which controls the clocks of the station-PC and the digitizer. Optionally, a weather station can be connected via serial link to the station-PC. Provision of electricity is stabilized by an uninterruptible power supply (UPS). Data transfer and station maintenance is possible via digital telephone line (ISDN) and on-site via Ethernet connection. The equipment will be described in detail in the following.

Station Computer

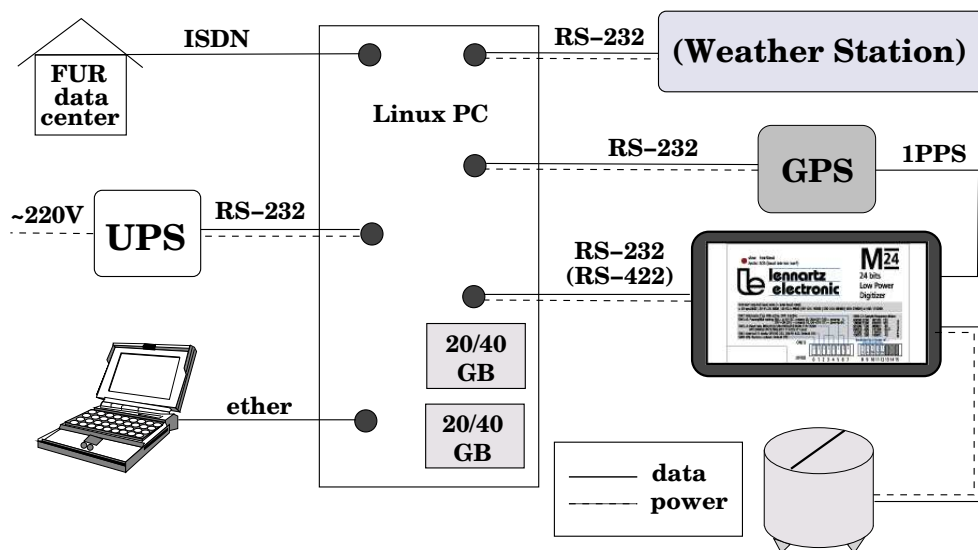
One of the major advantages of the station design implemented in the **BayernNetz** is, that an off-the-shelf PC is used as the central unit of the system. It is run by the open-source operating system LINUX, which allows to implement many freely available software tools without additional costs and assures great flexibility. As mentioned above, the **BayernNetz** was built in two phases. This is why the used PC hardware is slightly different at most of the stations. Additionally, some of the original station-PCs had to be replaced after being damaged by lightning. However, the minimum configuration uses processors with 170 MHz clock rate and has a working memory of 128 MB. The PCs are equipped with two identical hard disks that have a storage capability of 20-40 GB, an Ethernet-card for on-site maintenance, an ISDN-card for communication with the data center and four RS-232 serial ports, two of which are provided by an additional PCI-card².

To assure an easy station installation, the power supply for the Digitizer and the GPS were re-configured to be transmitted via unused pins of the serial connector. For this purpose the PC-internal 12 V DC-power unit was attached to two newly installed serial connectors (9-pin for GPS and 25-pin

²PCI stands for Peripheral Component Interconnect



(a)



(b)

Figure 2.5: Station hardware of the new Bavarian Seismological Network. a) Picture of the hardware components of the stations. b) Schematic diagram explaining the connection between the individual hardware components.

for M24), which were also connected with the two on-board serial ports. In this way it was possible to use one cable for data and power transfer to the

seismological equipment and have unequivocal connectors for the different hardware components.

Analog-Digital Converter

The *Lennartz M24 Digitizer* is a three-channel, 24-bit unit, with a serial output interface that can be switched between RS-232 (potential-based) and RS-422 (current-based) compliance. The latter should in theory allow to have a serial cable length of up to 1000 m. A distance of 500m was successfully tested in the Geophysical Observatory FUR. However, a critical factor for the achievable distance is the adequate transmission of the one-pulse-per-second (PPS) timing signal from the GPS to the M24.

The M24 Digitizer comes packaged in a waterproof, shock resistant suitcase-type box and operates on 12 V DC-power. It has three analog inputs, which are functionally equivalent. The inputs are differential inputs with a maximum input voltage of ± 10 volts. The "native" full scale input voltage is ± 5 volts, but there is a switch-selectable pre-attenuator (factor 2). In addition, there are three possible pre-amplification settings, with a factor of 4 in between them, i.e. the pre-amplification factor can be 1, 4, 16, or 64. For the stations of the **BayernNetz** a factor of 1 was chosen, which results in a Least Significant Bit (LSB) value of $0.596 \mu\text{V}/\text{count}$.

Short Period Seismometer

The standard seismometers used in the **BayernNetz** is the *Lennartz LE3Dlite-1Hz* sensor. This is a negative feedback sensor, which was originally developed at the University of Munich [*Lippmann, 1982*]. The sensor is based on a standard 4.5 Hz geophone, with the eigenfrequency reduced to 1Hz by feeding the negative sensor signal back into the sensor coil. The seismometer is very compact and has proven to be reliable over many years with little need for re-calibration. Technical data of the seismometer are summarized in Table 2.1.

Broadband Seismometer

A second seismometer type used in the **BayernNetz** is the broad band sensor *Streckeisen STS-2* [*Wielandt and Streckeisen, 1982*]. The STS-2 was one of the first widely available broad band sensors of the force balance type.

This means that the external force on the sensor mass is compensated by an electronically generated force in the opposite direction, so that it stays nearly stationary. Since the mass hardly moves, the linearity of the system is very good. The seismometer has become a global standard instrument in broad band seismology. Technical specifications of the seismometer are summarized in Table 2.1.

Sensor	LE3Dlite	STS-2
Components	3, orthogonal	
Eigenfrequency	1 Hz	120 s
Upper frequency limit	80 Hz	50 Hz
Output constant	400 V/m/s	1500 V/m/s
Damping	0.707 critical	
Dynamic range	136 dB	145 dB

Table 2.1: Technical data of Lennartz LE3Dlite and Streckeisen STS-2 seismometers.

Global Positioning System Receiver

Time keeping is a very important issue in seismology, since many seismological methods are based on the measurements of accurate phase arrival times. The **BayernNetz** uses the Global Positioning System (GPS) [e.g., *El-Rabbany*, 2002] for absolute timing of the data.

The *GARMIN GPS-35-HVS* is a 12 channel GPS receiver with embedded antenna. It can track up to twelve satellites at a time while providing one-second navigation updates via RS-232 serial link. These ASCII strings are coded due to NMEA0183 standard [*NMEA*, 2002] and contain the absolute timing information. Additionally, a high-precision one-pulse-per-second (PPS) signal is available with an accuracy of $\pm 1 \mu\text{s}$. The timing concept implemented in the acquisition software by Lennartz uses both timing informations. However, some problems did arise with this concept, which will be described in detail in Section 2.2.2.

Uninterruptible Power Supply

The need of an uninterruptible power supply (UPS) came clear in the months after the installation of the first stations of the **BayernNetz**. Over voltages or short power downs due to lightning strike in the wider vicinity of the

stations did cause hardware damage or left the file system in an undefined state that inhibited the reboot of the station-PC. After installation of the UPS the occurrence rate of this problem reduced to nearly zero.

The *ONLINE YUNTO Q-450* is a interactive uninterruptible power supply (UPS). It provides protection against power failures as well as spike suppression and line noise filtering to protect critical equipment. Communication with the control software *DataWatch*, running on the station-PC, is provided by RS-232 serial link. In case of power failure the UPS can supply power to the acquisition system for 5 min (hardware coded by manufacturer battery would allow 20 min). After this time the operating system is shut down via serial-link command. After power is available again the station-PC boots automatically as set by BIOS option.

Weather Station (optional)

An optional element for the stations of the **BayernNetz** is a weather station, which can be connected to the station-PC via RS-232 serial link. The weather station consists of sensors for precipitation, atmospheric humidity, atmospheric temperature, and atmospheric pressure. The data are digitized every second by a 16 bit A/D-converter coming with the station. All components were delivered by *A. Thies Klima GmbH*.

Because of the unacceptable power consumption of the weather stations, due to the heating of the individual sensors, the original station concept had to be changed. The sensor heating was turned of and a 6.5 Ah accumulator, which is recharged via the 12 V DC-power supply of the station-PC, was placed with the weather station. Further, the sensors and the steel casing, including the *MeteoLog TDL 14* datalogger, were mounted on a two-inch steel pipe, which is usually rammed 50 cm into the ground. With this configuration easy installation and low power consumption were assured and deployment of the weather station in remote areas with low power supply was enabled. The hardware in use in the **BayernNetz** is shown in Figure 2.6.

Data is transfered to the station-PC via RS-232 serial link. Communication with the weather station is in principle possible via a second serial-link connection available at the datalogger. This option is, however, not implemented at the moment, as it would necessitate further serial-link ports at the station-PC not available at present. Unfortunately, this situation does not allow to control the clock of the weather station via the GPS-controlled

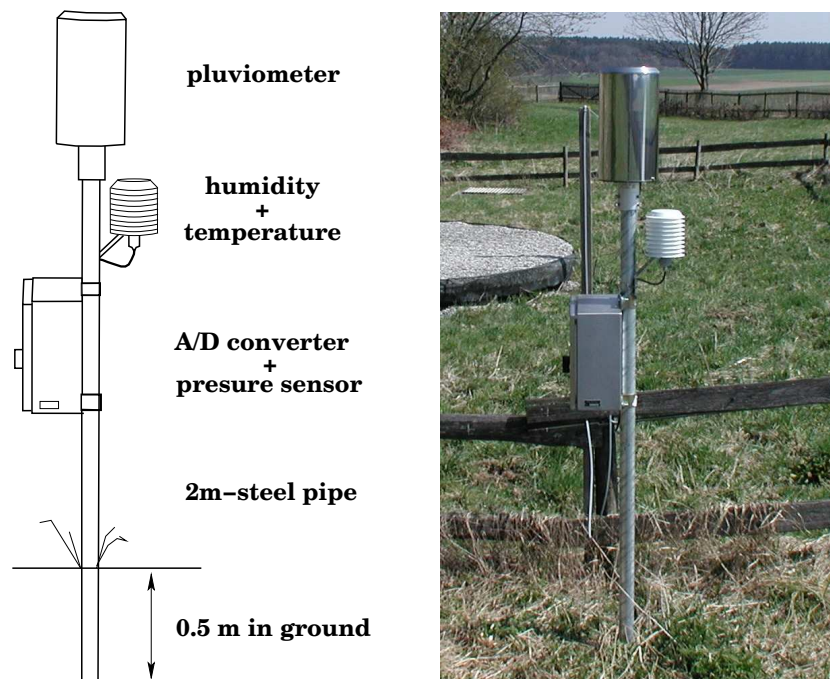


Figure 2.6: Hardware of the weather stations of the new Bavarian Seismological Network. Right) Picture of the hardware components. Left) Schematic diagram explaining the individual hardware components.

station-PC clock. Therefore, the clock has to be set manually during station maintenance. However, so far the accuracy of the weather station clock was sufficient to assure a drift less than 1 s between station visits (usually 3-4 months).

2.2.2 Software

The software for the operation of the **BayernNetz** is a combination of open-source seismological and networking software packages, as well as self-made script-based tools for flow control and visualization. The data acquisition is controlled by the Lennartz software *m24plug* and *SeisComP* of the GFZ Potsdam, which store data in mini-SEED format [Ahern *et al.*, 2006] on the station-PC and provide several quality-control interfaces. Extraction of event data, visualization of seismograms for the internet, and data transfer is done by LINUX-based scripts. An overview of the data flow from the seismometer to the data center and the involved software is given in Figure 2.7. In the following the different software components will be described in more detail.

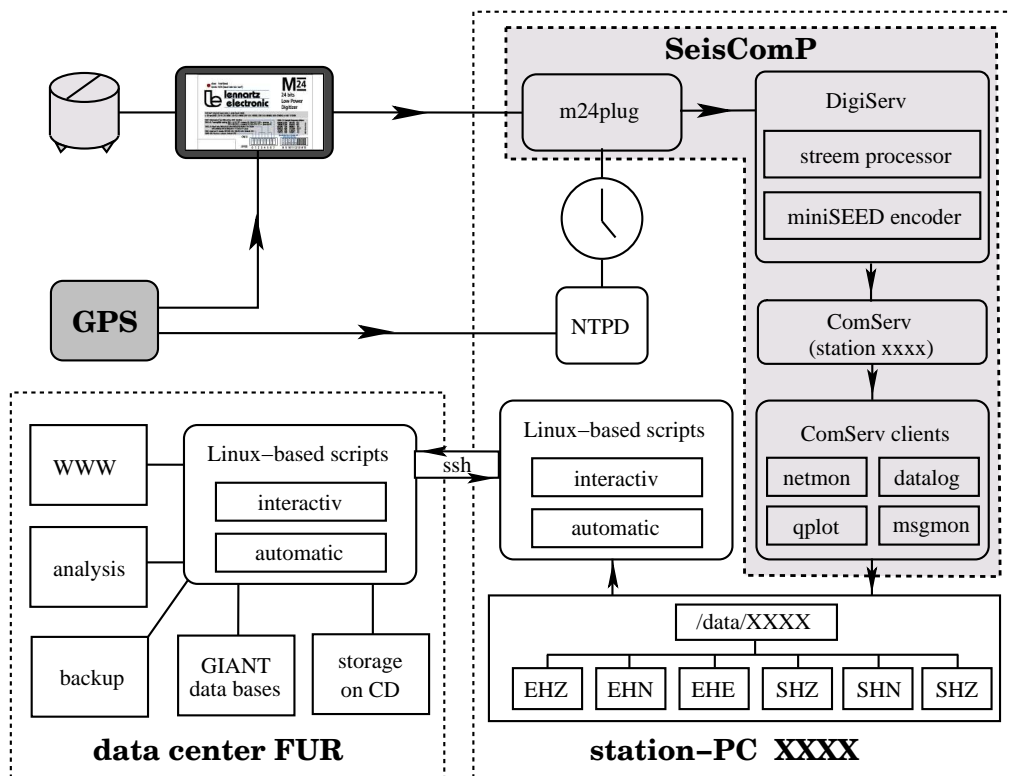


Figure 2.7: Data flow diagram of the Bavarian seismological network. The diagram is divided in three parts that represent the sensors, the station-PC and the datacenter. The dataflow is indicated by arrows.

m24plug and the problematic M24 timing concept

The basic software for data acquisition is the program *m24plug*, which is Lennartz's plugin to the *SeisComP* package. This plugin reads the raw data from the *M24* digitizer, timestamps it, and feeds it into *SeisComP*. However, the timing concept implemented in *m24plug* can cause serious problems after the start-up of the station-PC. Therefore, it will be described here in detail and solutions for an accurate time keeping are given.

As illustrated in Figure 2.7 two sources of timing information leave the GPS receiver. As described earlier, these are a highly accurate pulse-per-second voltage signal (PPS) and a navigation information string (NMEA). The PPS is transmitted to the *M24* digitizer and controls its hardware clock. In the raw data, transmitted from the *M24* to *m24plug*, full-second samples are marked by a special flag. Hence, these samples are known to occur at full seconds with an accuracy nearly as good as the PPS precision of $\pm 1 \mu\text{s}$. However, no absolute timing is available in the *M24* digitizer.

The NMEA string is transmitted from the GPS to the station-PC, where it controls the hardware clock via the *Network Time Protocol Daemon (NTPD)* [Mills, 1991]. *NTPD* was designed to synchronize computers in a network to a trusted time source. Here, it is used to synchronize the station-PC clock to the GPS time by using the NMEA string, which arrives every second via serial link. The *m24plug* software combines the marked full-second samples of the raw data stream with the absolute time information from the PC-clock, which is assured if the clock is off by significantly less than 500 ms. Because of the latency of the serial hardware, the GPS-conditioned PC-clock has only a bad accuracy. However, if the distance of the PC-clock with respect to the reference clock is larger than ± 128 ms, *NTPD* jump sets the PC-clock. This assures a correct association of the marked full-second samples of the raw *M24* data stream.

Yet, a serious problem arises after the restart of the station-PC. The hardware clock is then in an undefined state and time difference to the reference clock may be arbitrary large. Because of the original purpose of *NTPD* statistical checks of the reference time signal are done. Depending on the stability of the reference signal *NTPD* sets the PC-clock to reference time after 15-60 min. As *m24plug* assumes that the PC-clock is correct, the timing of the seismological data is wrong in this time interval and has to be corrected manually. The first version of *m24plug* did even only once check for adjustments of the PC-clock at start-up. After the author brought the problem to the attention of Lennartz Electronics, *m24plug* was changed to check for PC-clock changes at least every 15 minutes.

Additionally, *NTPD* does not trust the reference time signal, when it is offset by more than two hours from the PC-clock. In this situation the clock is not corrected at all and timing of the seismological data is off by an arbitrarily amount of integer seconds. The solution to the latter problems was to set the PC-clock to the time of the dialer-PC in the data center after startup. The dialer-PC provides accurate timing in the range of ± 50 ms, but no statistical analysis of network latency is done in this process. Though, it was now assured that *NTPD* trusted and accepted the GPS-time, it did not solve the problem of probable timing errors in the time interval before that with definite certainty.

Fortunately, the arising timing errors can only be integer seconds. For stations having neighboring stations with reliable, correct timing, these error

can be corrected by comparing seismograms of teleseismic events. If the station distances are sufficiently small, even local earthquakes can be used for this purpose. In this, however, very time consuming way, it was possible to save the very interesting dataset of the year 2002 in the sub-network near Bad Reichenhall.

Possible solution to the problem are (1) to recode *NTPD* to accept GPS reference without further statistical check, which would perhaps introduce new problems of the same kind, or (2) to change the timing concept of the Lennartz *M24* digitizer completely and assign absolute time during the digitization process in the *M24*. However, it was not possible so far to convince Lennartz Electronics to do so.

SeisComP/Seedlink

The *Seismological Communication Processor (SeisComP)* is an initiative of the GEOFON program at the GFZ Potsdam [Hanka *et al.*, 2000]. It is a software package for data acquisition, recording and monitoring, real-time communication and automatic network data processing. The data acquisition part is based on the publicly available *ComServ* software [Quanterra, 2002]. The real-time communication part (*SeedLink*) ensures robust transfer of mini-SEED packages through any TCP/IP-based [e.g., Hunt, 2002] communication channel. Data acquisition plugins for a large number of acquisition systems are presently available and more will be developed. Data export is supported through the *SeedLink* protocol to other *SeisComP* systems. The *SeisComP*, *SeedLink* and plugin software are all publicly available and protected under the GNU license [Free Software Foundation, 1991].

In the **BayernNetz** only the data acquisition part of *SeisComP* is in use. Because of the limited bandwidth and high charges of the ISDN telephone connection between station and data center, data can not be transferred continuously. The concept followed here, is to record two separate data streams with sampling rates of 20 Hz (SH-stream) and 200 Hz (EH-stream) respectively, whereas only the SH-stream is transferred completely. This is done on weekends, when the telephone lines are available without charge. By contrast, only event data is extracted from the EH-stream. The latter was not possible with *SeisComP* at the time of installation and a self-coded solution is used for the **BayernNetz**.

Figure 2.7 illustrates the data flow through the software components of *SeisComP*. Data and logging information is transferred from the plugin

m24plug to the program *DigiServ*, which converts the data to 512-byte mini-SEED packets and generates the two data streams by down-sampling using digital decimation filters. Various sampling rates can be produced by combination of different digital filters available. However, care has to be taken to account for the resulting time delay associated with every filter operation.

The mini-SEED packets are handed over to the *ComServ* server. *ComServ* provides acquisition functionality via its clients. At the stations of the **BayernNetz** *ComServ* clients for start and restart of the acquisition (*netmon*), output of logging messages (*msgmon*), real-time data visualization (*qplot*) and data storage on hard disk (*datalog*) are in use. Data is stored in form of 512-byte-block mini-SEED files on the data partition of the hard disk. The directory structure is illustrated in the bottom of Figure 2.7, the top level directory is named after the station (e.g., XXXX) and contains sub-directories for every component of the two streams (e.g., EHZ for the vertical component of the 200 Hz stream). Inside these sub-directories data is organized in day-files, containing 24 hours of data each.

2.3 The Data Center

In this section the technical design of the data center of the **BayernNetz** at the Geophysical Observatory in Fürstenfeldbruck (FUR) is described. After a brief introduction of the hardware, the LINUX-based software is discussed.

2.3.1 Hardware

The data center of the **BayernNetz** is located in the Geophysical Observatory in Fürstenfeldbruck (FUR), 25 km west of Munich. The seismological stations are connected to the data center via ISDN telephone line. ISDN³ offers two 64 kbit/s digital communication channels per telephone line. At FUR, two ISDN lines are available for the communication with the **BayernNetz** stations. As shown in Figure 2.8, the dialer-PC "wanninger"⁴, handles

³ISDN stands for Integrated Services Digital Network

⁴The dialer-PC is named after "Buchbinder Wanninger" a sketch by the Munich cabaret artist and comedian Karl Valentin (1882-1948). The bookbinder Wanninger is more and more desperately trying to leave his message regarding finished books at the building company Meissner. He is passed on from contact to contact but never reaches the responsible person and has to repeat his introduction with increasing disintegration of speech over and over again

the ISDN telephone lines with two ISDN-cards and routes the connections to the internal Ethernet network of the data center. The dialer-PC also runs the data-center-side scripts for extraction and transfer of data from the stations. Further, incoming data are stored on its hard disk and then transmitted to the internal network.

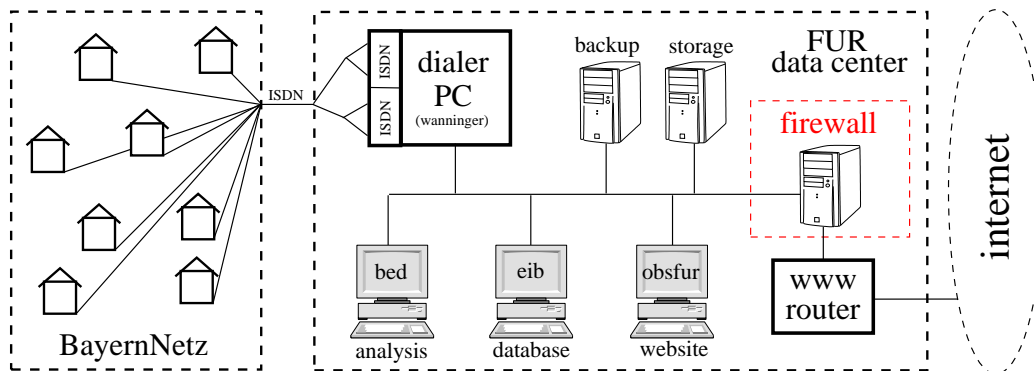


Figure 2.8: Design and dataflow of the data center FUR at the Geophysical Observatory Fürstfeldbruck.

In the data center six LINUX-PCs handle the data management. Interactive analysis software and the event database are available at every computer in the network. However, the main event database for the **BayernNetz** is kept on PC "eib"⁵, whereas project orientated databases are stored on PC "bed"⁶. The website of the Bavarian Earthquake Service, which offers information on the service and current seismicity, is located on PC "obsfur"⁷. Backups of important configuration files, selected user directories and seismological data are stored on four 150 GB hard disks of PC "baybackup". Finally, the data is burned on Compact Disks for permanent storage using the CD-drives of PC "mitch".

All computers of the data center are connected via the Ethernet network of the Geophysical Observatory. This network is linked to the internet by a router-PC, which is maintained by the Leibniz Rechenzentrum (LRZ), the computing center of the Bavarian Academy of Science. However, the LRZ does only provide basic network security measures, which simplifies the intrusion of the network by unauthorized third-party users. Therefore, the network of the observatory had to be protected by a firewall, running on a

⁵eib stands for "Erdbeben in Bayern" (earthquakes in Bavaria)

⁶bed stands for "Bayerischer Erdbebendienst" (Bavarian Earthquake Service)

⁷obsfur stands for "Observatory Fürstfeldbruck"

separate computer. This PC is equipped with one receiving and one sending Ethernet-card. The entire network traffic is bridged via the receiving card through the firewall and transmitted back to the network by the sending card. The firewall filters the network traffic and prevents unauthorized access. The firewall was conceived and configured by R. Leonhard⁸.

2.3.2 Software

As the data transfer is initiated by the data center the necessary software, including scripts running on the station-PCs, is discussed in this section. Main emphasis is, however, placed on the description of self-coded software, whereas the LINUX-based networking programs will only be briefly mentioned. For detailed information on LINUX networking refer to e.g., *Kirch and Dawson* [2000].

Network Security

To assure secure communication between the computers in the network the software package *OpenSSH* [Ylonen, 1995] is used, which is a set of standards and an associated network protocol that allows establishing a secure channel between computers. It uses public-key cryptography to authenticate the computers. Public key cryptography uses a pair of cryptographic keys, designated as public key and private key, which are related mathematically [e.g., *Barrett and Silverman*, 2001]. The two keys have to be generated before the first connection and are then exchanged automatically in later sessions without user interaction. The underlying TCP/IP-based connection - e.g., over ISDN or Ethernet - is handled by the operating system and will not be discussed here.

Additional security of the communication between station and data center is achieved by the configuration of the ISDN connection. Normally connections are initiated by the data center. The station identifies the caller by the transmitted telephone number and only accepts calls from the data center. Additionally, incoming calls are only accepted at the data center if the telephone number transmitted by the opponent is recognized as a station telephone number. If station-side initiation of a connection is necessary,

⁸Honorary system administrator of the Geophysics Institute of the University of Munich.

the station rings once at the data center and disconnects. Hereupon, the data center identifies the station by its telephone number, calls back and establishes the connection. Thereby, only trusted connections are accepted and connection costs are only incurred at the data center.

Data Extraction and Transfer

Although, *SeisComP* offers state-of-the-art technology for data exchange between station and data center, its Data Request Manager (DRM), which handles the extraction of event data from the continuous data streams, was at the time of installation not suited to the needs of the **BayernNetz**. In particular, automated extraction of data on the basis of scripts was hardly possible. Therefore, the data transfer and the interactive extraction on event data was reprogrammed on basis of open-source software and LINUX-based shell scripts.

A huge amount of data is acquired every day in the **BayernNetz**. Approximately 90 MB of mini-SEED data have to be stored on hard disk for the three-component EH-stream (200 Hz) at one station in 24 hours. This corresponds to a transfer volume of ~ 720 Mbit, and, assuming an ideal ISDN connection, would require ~ 3.1 hours transfer time. The download of the complete EH-data of the 21 **BayernNetz** stations via four ISDN channels takes ~ 16.4 hours. This corresponds to approximately 30 Euro of telephone costs per day assuming the cheapest possible connection times. This is far beyond the available budget. Therefore, the data transfer concept realized in the **BayernNetz** is to transmit EH-data on event-basis only, but to download the entire SH-data (20 Hz) of one week on weekends when the telephone lines are free of charge⁹.

Event-Based Data Extraction

The event-based transfer of the EH-data is an interactive process, initiated by the seismologist on duty in the data center. However, as the procedure is based on scripts, it can easily be automated. The seismologist runs the script *cutevent* on the dialer-PC and gives necessary information on extraction time window as well as the desired stations and stream as commandline options. The *cutevent* script, hereupon, establishes connections to the desired stations one after the other, and runs several sub-scripts that prepare the input files

⁹ISDN-XXL telephone rate offered by Deutsche Telekom.

for *SeismicHandler* [Stammler, 1993]. The hard disk of the station-PC is scanned for the appropriate data files, which, depending on the storage capacity, may be up to six months old.

SeismicHandler extracts the data from the mini-SEED data files and converts it to GSE format [GSETT-3, 1997]. After this, the GSE files are compressed with the software *gzip* [Gailly and Adler, 1993]. A *gzip*-compressed GSE file has a smaller file size than the original mini-SEED file and is therefore used for data transfer. The extracted time windows are sent to the data center and stored on the hard disk of the dialer-PC, where they are available for analysis and import into the data base. Scripts and configuration files for the data extraction can be found on the Supplement CD and are listed in Appendix B.

Transfer of Continuous Data

Backward access on the EH-data is limited to a maximum time range of three to six months, depending on the storage capacity of the station-PC. Local event data, however, can be accessed at any time, as it is stored in the **BayernNetz** data base in the data center. Teleseismic and regional event data are normally not stored in the data base. However, experience shows that requests for these data from the scientific community frequently arrive after the maximum access time has already passed. Therefore, archiving the recorded SH-data is of paramount importance for being able to contribute to various seismological research problems.

The recorded SH-data is transferred to the datacenter on a weekly basis in an automated process. On Saturdays, at 1:11 local time, the LINUX-program *cron*¹⁰ starts the script *get_20Hz_data* on the dialer-PC that establishes connections to all stations and transfers the SH-data of the last seven days. During the SH-data download, three stations are connected to the data center at any time, leaving only one ISDN-channel open for additional tasks (e.g., the regular download of seismogram images for visualization on the internet). The download of the SH-data takes approximately 2.5 hours per station, which sums up to approximately 17 hours to transfer the SH-data of the entire network for the last seven days. The scripts and configuration files for the data transfer can be found on the Supplement CD and are listed in Appendix B.

¹⁰*cron* provides the possibility to start software at user-defined times.

The transfer algorithm is simple but works fine if telephone connections are stable. However, frequently pilot wires of bad quality had to be used to connect the **BayernNetz** stations to the public telephone network, which reduces the reliability of the telephone connection. Furthermore, no controls mechanism for complete data transfer or initiation of recalls in case of unattainability of single stations is implemented. The solution to this problem would be to use *SeisComP* for the transfer of the continuous SH-data. As SeisComP uses well-established internet protocols for exchanging data, lossfree transfer of the data is assured. This concept was implemented during a network-wide software update in 2004, when J. Wassermann took over the responsibility for the **BayernNetz**.

2.4 Public Presentation of the Data

One of the main objectives of the **BayernNetz** is to pass on earthquake information to authorities and the public. For this purpose a webpage was created that provides general information on the project "Bavarian Earthquake Service" as well as near-real-time data visualization. Browsing seismological data is possible via an interactive navigation interface. Additionally, two information centers were put up in northern and southern Bavaria that present seismological information in slide shows and on posters. Furthermore, information on global seismicity is provided on the webpage of the Institute of Geophysics of the University of Munich. These public information platforms will be described in the following.

2.4.1 Homepage of the Bavarian Earthquake Service

In Germany the number of internet users is rising constantly. Thus, the proportion of Germans regularly using the internet increased from 6.5% to 53.5% between 1997 and 2003 [*Eimeren et al.*, 2003]. The internet is therefore an efficient instrument to transfer information to a broad public.

The internet presents of the Bavarian Earthquake Service offers general background information on the project history and seismology as well as detailed information on the **BayernNetz** and the Bavarian seismicity. The website visitor can fill in a macroseismic questionair, find usefull links as well as answers to frequently asked questions, and can contact the experts via email. Many members of the Geophysics Institute in Munich contributed

to the content of the webpages. Therefore, only the data section of the homepage will be described in the following, as it was developed by the author.

Navigation

The data section of the **BayernNetz** homepage can be accessed via the item "Daten*live*" in the main navigation menu. The associated webpage can be divided into four elements as indicated in Figure 2.9 by numbered ellipses and referred to in the following. The data navigation menu (1) allows to choose which type of data to display in the page body (4). As discussed below, seismograms, spectrograms, GPS positions and weather data may be displayed. The station navigation menu (2) allows to select the station to be displayed. It is divided into three parts, which represent the geometry

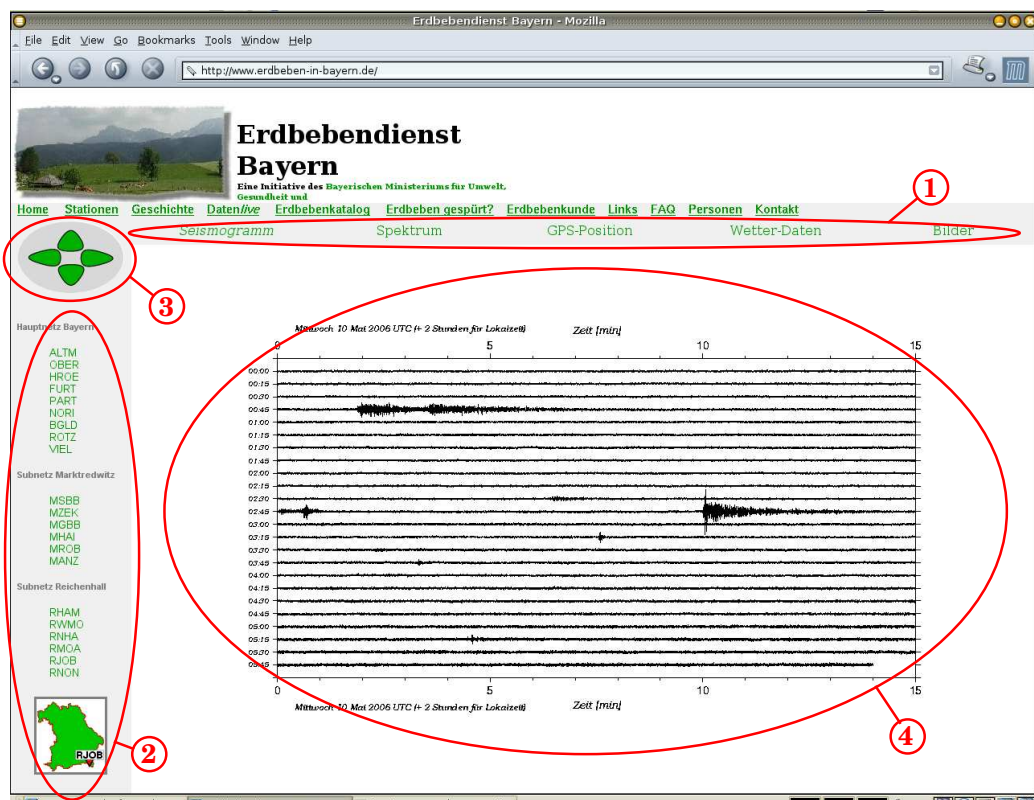


Figure 2.9: Data section of the Bavarian Earthquake Service homepage. Numbered ellipses indicate: 1) data navigation menu; 2) station navigation menu; 3) interactive navigation tool (*inav*) to browse the data of the last seven days (up-down) and all stations (left-right); 4) page body for data display; The address of the homepage is: <http://www.erdbeben-in-bayern.de>.

of the **BayernNetz**. The top part lists the main network stations that are not associated with the subnetworks in Marktredwitz and Bad Reichenhall, which are listed in the two lower parts. At the bottom of the station navigation menu a miniature map of Bavaria shows the location of the station currently displayed.

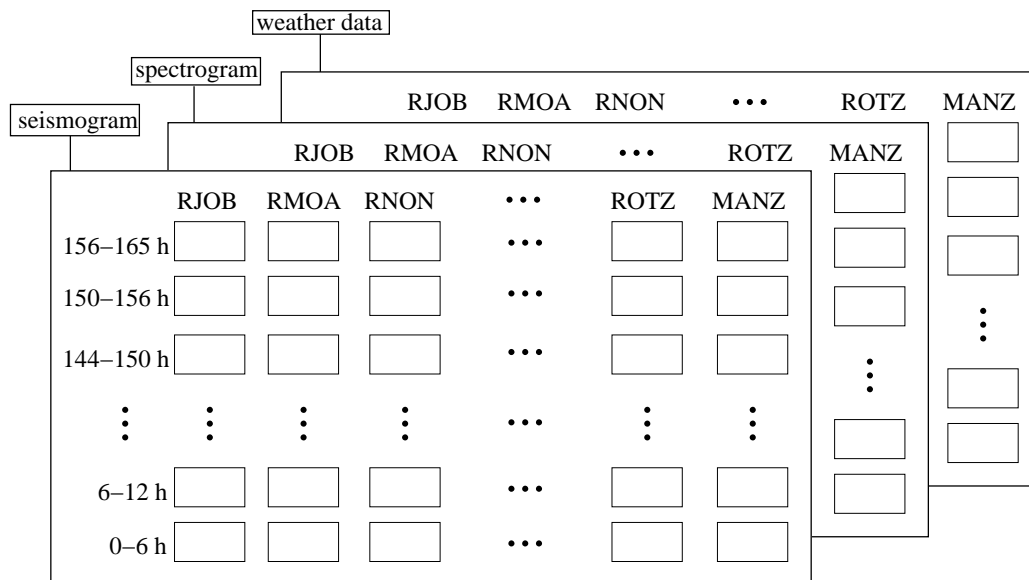


Figure 2.10: Virtual matrix structure of data display. Columns represent temporal ordering, whereas rows correspond to different stations. The structure is identical for the different data types. Using the arrow buttons of the *inav* the user can brows through the data.

The *interactive navigation tool (inav)* (3 in Fig. 2.9) is used to browse the **BayernNetz** data of the last seven days. The data are visualized in form of GIF images [CompuServe Inc., 1990] created with the open-source mapping software *GMT* [Wessel and Smith, 1991]. The four arrows of the *inav* can be used to navigate through a virtual matrix structure of these GIF images. Figure 2.10 shows how the virtual matrix is organized. Columns represent temporal ordering, whereas rows correspond to different stations. The structure is identical for the different data types. Using the arrow buttons of the *inav* the user can brows through the data. The *inav* arrows pointing up and down are used to navigate back and fores in time. Whereas the *inav* arrows pointing left and right switch between stations. Changing the displayed time interval will leave the station and data type unchanged. Furthermore, changing the data type will leave the current station and time unchanged. Equivalently, switching the station will not change the currently

displayed time interval and data type. This enables the user to directly compare data of different stations and to find correlated signals.

The *inav* is implemented as a *JavaScript* [e.g., *Flanagan, 2002*] program, which, based on interactive user input and the current display status, determines the appropriate GIF file and reloads all effected parts of the webpage. The *JavaScript* program is part of the HTML-source of the homepage and is included in the Supplement CD.

Seismogram, Spectrogram, GPS and Weather Data

The software creating the GIF images to be published in the internet is running on the station-PC. The LINUX-program *cron* starts the software in 30 minute time intervals, and creates plots of ground motion data, weather data and GPS position data. In the following the data types displayed at the **BayernNetz** homepage are introduced considering as example the recordings of station RJOB that belongs to the Bad Reichenhall subnetwork.

The most essential data visualized on the **BayernNetz** homepage are seismograms. These are timeseries of the recorded ground motion. In the case of the **BayernNetz** they represent the ground oscillation velocity, because of employment of electro-dynamic seismometers in the entire network. Six hour seismograms of the vertical component of the SH-stream are created, using the script *day_traces_bin*. As illustrated in Figure 2.11, they are composed of 15 minute seismogram rows, which are arranged in temporal from the top to bottom. The diagrams are successively filled as data becomes available.

The frequency content of a time series can be displayed in a spectrum. Combining spectra of consecutive small time windows of a longer time series results in a spectrogram, which allows to visualize temporal changes in the frequency content of the time series and can help to identify earthquake signals and sources of noise. As shown in Figure 2.12, the vertical axis represents frequency, whereas the horizontal axis represents time. For being able to use only integer values for annotation, the frequency axis is converted into a period axis below 1 Hz. Spectra are calculated by Fast Fourier Transform [*Cooley and Tukey, 1965*] of five minute time windows. Thereafter, the colorscaled spectra are aligned on the time axis, to form the spectrogram. The mean and maximum ground motion amplitude of the five minute time windows is displayed in two semi-logarithmic graphs on top of

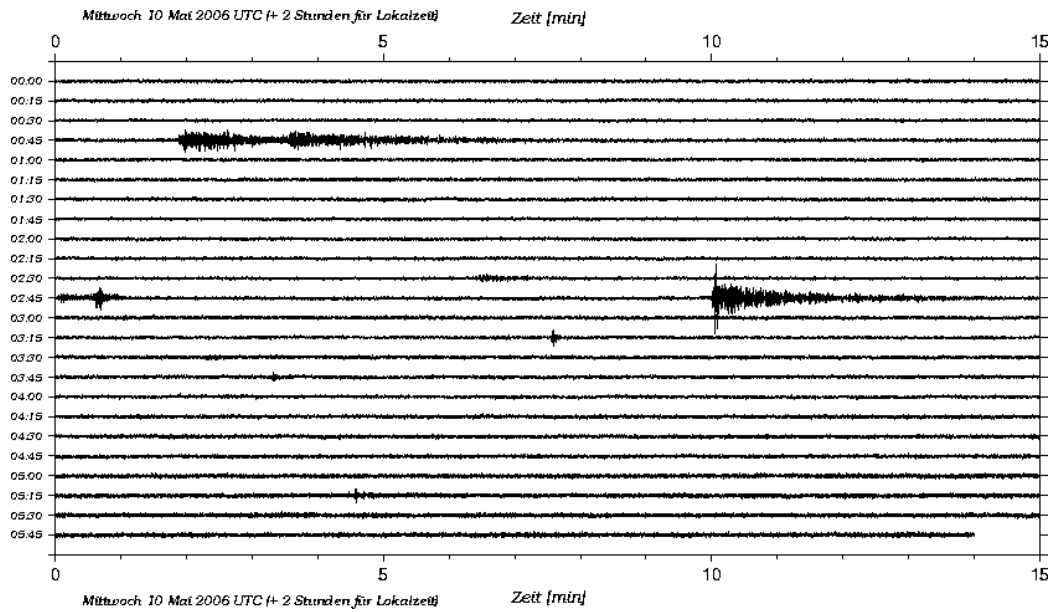


Figure 2.11: Example for seismogram data display on the **BayernNetz** homepage. One digram shows six hours of the vertical SH-stream seismogram. In each row 15 min of data are displayed. Starting times are indicated on the left. Several earthquakes can be seen in the seismogram plot:

2006-05-10 00:44:41	M=4.7	40.17° N	19.59° E	Albania
2006-05-10 02:42:55	M=6.1	52.53° N	169.31° W	Aleutian Islands
2006-05-10 02:54:33	M=4.5	40.23° N	21.21° E	Greece
2006-05-10 03:22:31	M=0.4	47.76° N	12.88° E	Bad Reichenhall

the spectrogram. These graphs help to compare the strength of different signals and to judge the time dependent ambient noise level.

Several common patterns are present in the spectrogram in Figure 2.12. The first six hours of the spectrogram shown in Figure 2.12, represent the data displayed in the seismogram in Figure 2.11. The earthquakes, indicated in the seismogram in Figure 2.11, can be identified as vertical lines in the spectrogram and as peaks in the mean and maximum ground motion graphs. The signal of a local event, characterized by the continuation of the vertical line in the spectrogram to higher frequencies, can be seen in the center of Figure 2.12 ($\sim 10:00$ UTC¹¹). Additionally, a band of elevated signal energy in the period range of 1-10s represents microseism, which is a faint earth tremor caused by storm systems and ocean waves [e.g., *Essen et al.*, 2003]. Furthermore, a band of high frequent, narrow-banded energy around 5 Hz in

¹¹Universal Time Coordinated

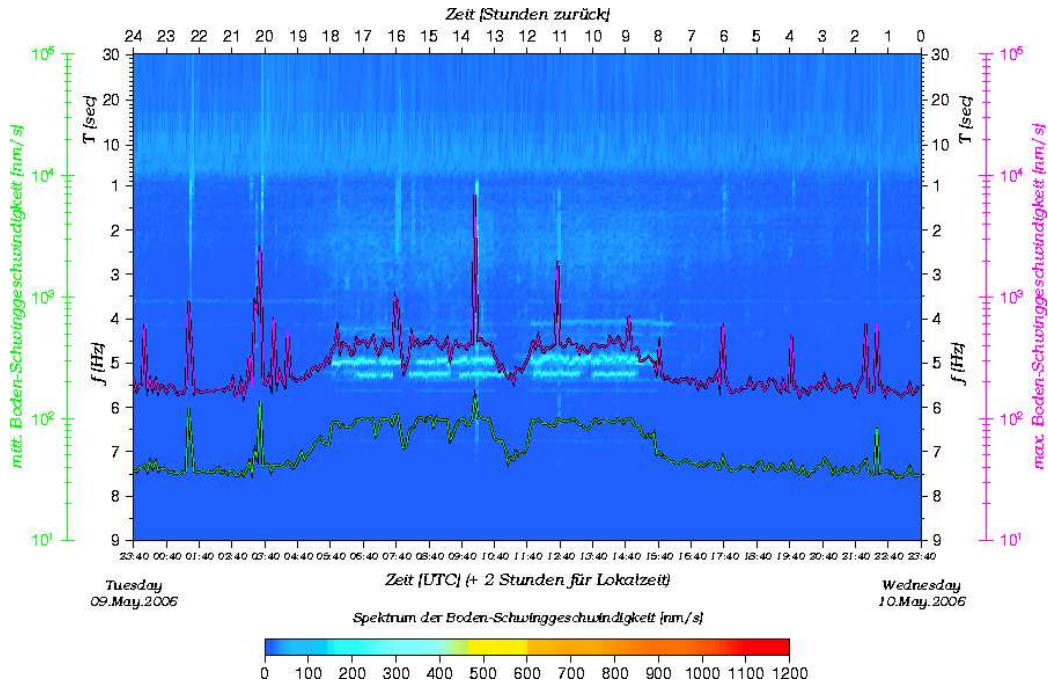


Figure 2.12: Example for spectrogram display on the **BayernNetz** homepage. Color coded spectrogram of the vertical SH-stream data. Frequency axis vertical, time axis horizontal. Spectra are calculated from 5 min time windows. Mean (green) and maximum (red) ground velocity in nm/s are given in semi-logarithmic graphs. The first six hours correspond to the seismogram shown in Figure 2.11. Time is indicated in UTC at the bottom and in hours from present at the top.

the time range between $\sim 6:00$ - $\sim 16:00$ UTC, is caused by a sawing mill in several kilometer distance of the seismological station. Working hours and lunch break can clearly be identified in the spectrogram and the graphs of mean and maximum ground motion.

Figure 2.13 shows the GPS position data. Although, this data is normally not used, highly accurate coordinates of the station locations were derived from its longtime average. The figure shows a map view of the minutely derived GPS position marked by red points. The center of the map corresponds to the current median position, which is also annotated at the map borders. The distance from the median position in meters is indicated by the map grid. Further, the distances from the median position for the North-South and East-West directions are plotted as two time series. The constance of the GPS position can be used as an indicator for the quality of the GPS signal and the reliability of the time reference for the **BayernNetz** stations.

Three stations of the subnetwork in Bad Reichenhall are equipped with weather stations. Their data is displayed in four diagrams shown in Figure 2.14. Time series for relative atmospheric humidity, precipitation, air

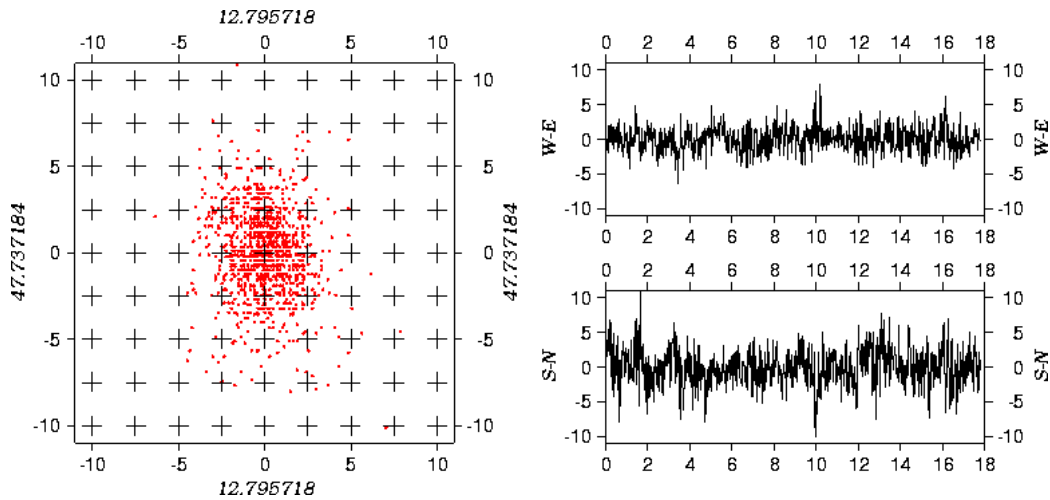


Figure 2.13: Example for GPS position display on the **BayernNetz** homepage. Left: Map view of minutely GPS positions (red). Mean position and distance in meters are indicated. Right: Time series of the east-west and north-south distance from the mean position.

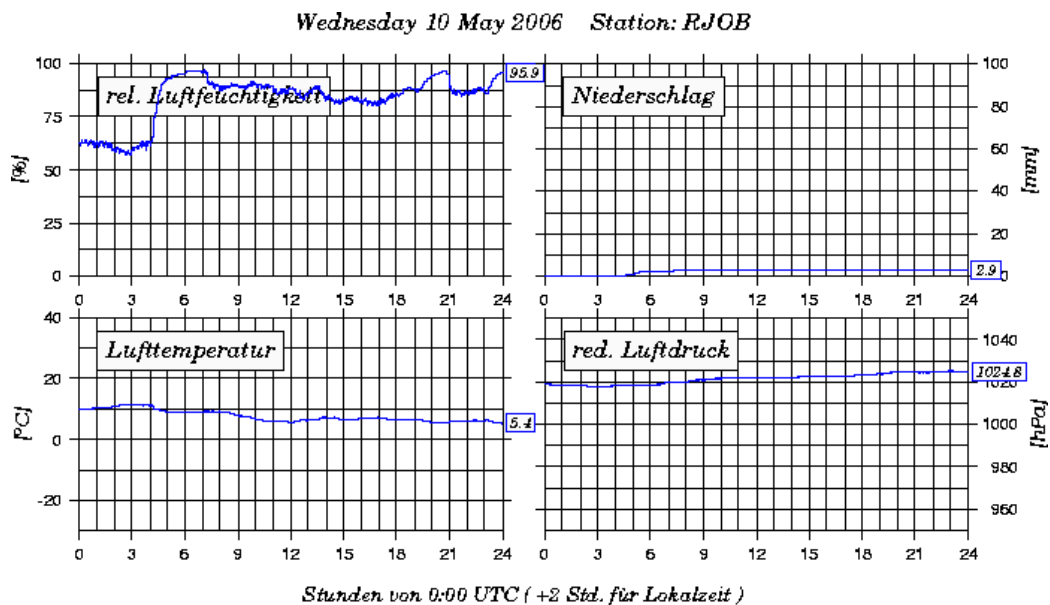


Figure 2.14: Example for weather data display on the **BayernNetz** homepage. Time series of rel. atm. humidity (upper left), precipitation (upper right), air temperature (lower left) and rel. atm. pressure are shown. Current value of meteorologic parameters indicated in boxes at end of time series.

temperature and relative atmospheric pressure are shown. The current value of the individual meteorological parameters is indicated in boxes at the end points of the time series. The data of the weather stations is analyzed to study the correlation between rainfall and earthquake activity observed in the Bad Reichenhall area (comp. Part II)

Public Information Centers



Figure 2.15: Picture of the info center of the **BayernNetz** at the site of the German Continental Deep Drilling Program (KTB). Monitor with slide show of earthquake information in the center. Two poster walls with presentations on scientific projects hide the info-PC.

Additional to the distribution of earthquake information via the internet, two public information centers offer background information and near-realtime data of the Bavarian Earthquake Service. One information

center is located at the Geocenter of the German Continental Deep Drilling Program (KTB) in Windischeschnebach, N-Bavaria . The Geocenter is a little museum that explains the goals and results of the KTB and offers the opportunity to visit the former drilling derrick. The second information center is located in the historic salt refinery of Bad Reichenhall. Both localities are major tourist attractions in their area and assure high visitor rates.

The seismogram and weather data, that are also displayed on the **BayernNetz** homepage, are shown in a slideshow on the computer (info-PC) of the information center. Additional information is given in text slides and figures. The slideshow is HTML-based, and can easily be configured and updated from the data center of the **BayernNetz**, which is connected to the information centers via ISDN telephone line. The seismogram and weather data images are transferred on a regular basis from the dialer-PC in the data center to the information centers. Presentations on current research in seismology at the University of Munich and background information on the **BayernNetz** are given on two poster walls, which are installed around the info-PC in such a way that only its monitor is visible as shown in Figure 2.15.

2.4.2 Homepage of the Geophysics Institute

Information, which focuses on global seismicity can be found on the homepage of the Geophysics Section of the Department of Earth and Environmental Sciences of the University of Munich (<http://www.geophysik.uni-muenchen.de>). Here, data of the GRSN broadband station FUR, which is located at the data center of the **BayernNetz** at the Geophysical Observatory in Fürstentfeldbruck are displayed. As the webpage focuses on strong teleseismic earthquakes, which may generate seismograms of more than one hour length, but have a low-frequent signal content, it was decided to display 24 hours seismogram and spectrogram plots. The websites are automatically generated by LINUX-based scripts and open-source software on the website-PC "obsfur" in the data center of the **BayernNetz**.

Figure 2.16 shows the 24 h seismogram plot of December 5, 2005. Earthquake source parameters are downloaded from the website of the Swiss Seismological Service, where earthquake location information from many earthquake services in the world is collected in near-realtime. Locations and source times of the earthquakes of the last 24 hours are used to calculate theoretical arrival times of the seismic phases at FUR using the earth

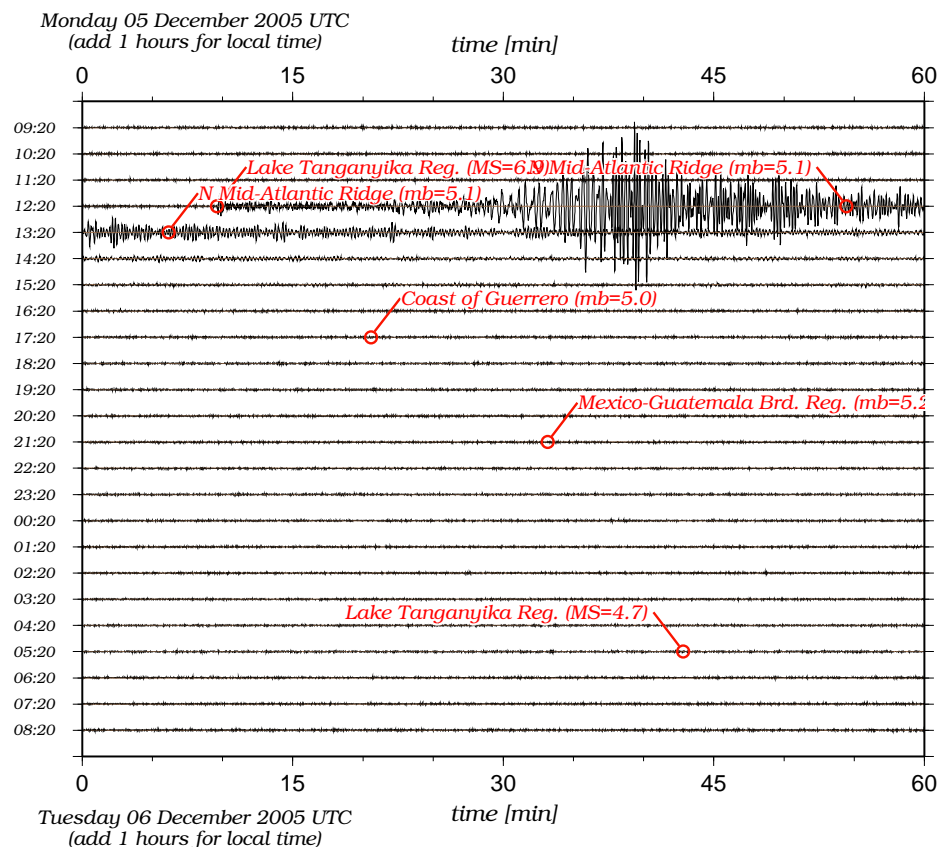


Figure 2.16: Example of the 24h-seismogram plot of the Geophysics Institute homepage. In each row 60 min of data are displayed. Starting times are indicated on the left. The theoretical arrival times of several earthquakes labeled. the seismogram is scaled to the maximum amplitude in the 24 h trace. The dominant event is a M6.9 earthquake from the Lake Tanganyika Region in Africa.

model *iasp91* and the software *ttimes* [Kennett and Engdahl, 1991]. The arrival times are then marked in the seismogram plot and labeled with the source region name and the magnitude of the event. The markers represent clickable hyperlinks to a webpage with 30 minute zooms of the seismograms. The dominant event in Figure 2.16 is a M6.9 earthquake from the Lake Tanganyika Region in Africa.

Figure 2.17 shows the spectrogram of the ground motion displayed in Figure 2.16. The spectrogram has the same structure as those displayed on the **BayernNetz** homepage, already described in Section 2.4.1. The spectrogram shown is dominated by low frequent surface waves of the Lake Tanganyika earthquake, which circle the earth for more than four hours. Surface wave signals of the other earthquakes labeled in Figure 2.16 can also be identified in the long period part of the spectrogram. A constant band

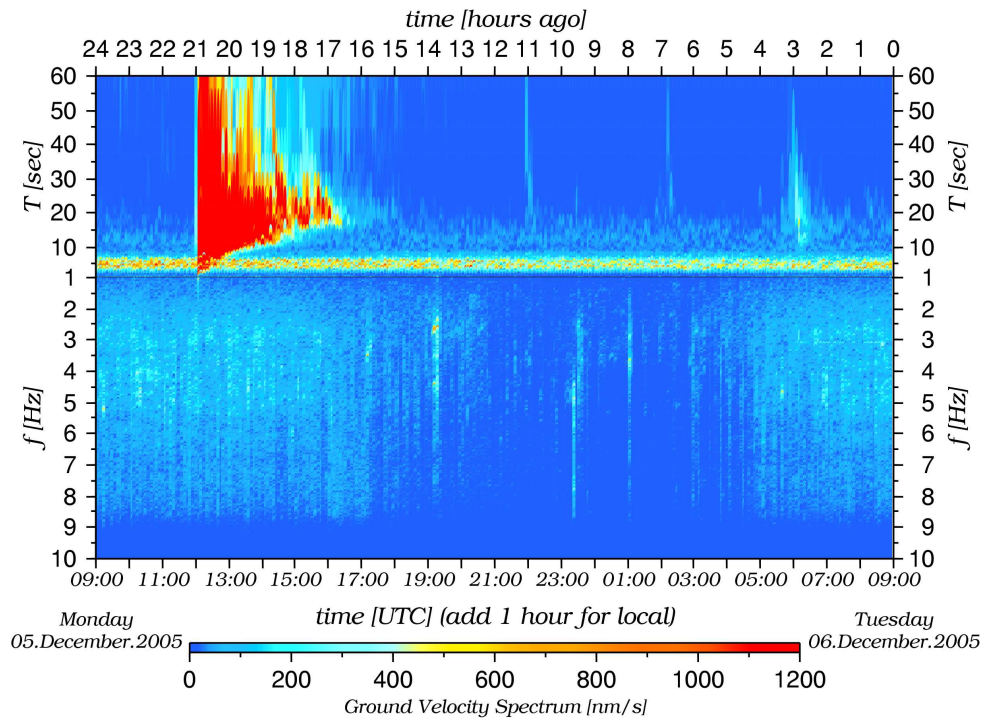


Figure 2.17: Example of the 24h-spectrogram plot of the Geophysics Institute homepage. The spectrogram is dominated by low frequent surface waves of the Lake Tanganyika earthquake, which circle the earth for more than four hours.

of elevated energy in the period range between 1-10s represent microseism. This band also separates teleseismic and regional earthquakes from local events in the spectrogram. The raised ambient seismic noise level during working hours can clearly be identified in the high-frequency part of the spectrogram.

Following the link "Current Seismicity" on the homepage of the Geophysics Institute leads to a webpage where the global earthquake locations of last the 24h are displayed. A world map containing major plate boundaries of Earth's crust is generated automatically with the open source mapping software *GMT* [Wessel and Smith, 1991].

As an additional service the menu item "News Ticker" links to the internet service *Google*, where press releases are searched for the occurrence of the word "earthquake". The search results are listed in temporal order and linked to the original news webpages. This service allows to rapidly access information on possible damage and casualties related to the earthquake listed

Last automatic update : Tuesday 06 December 10:21 UTC

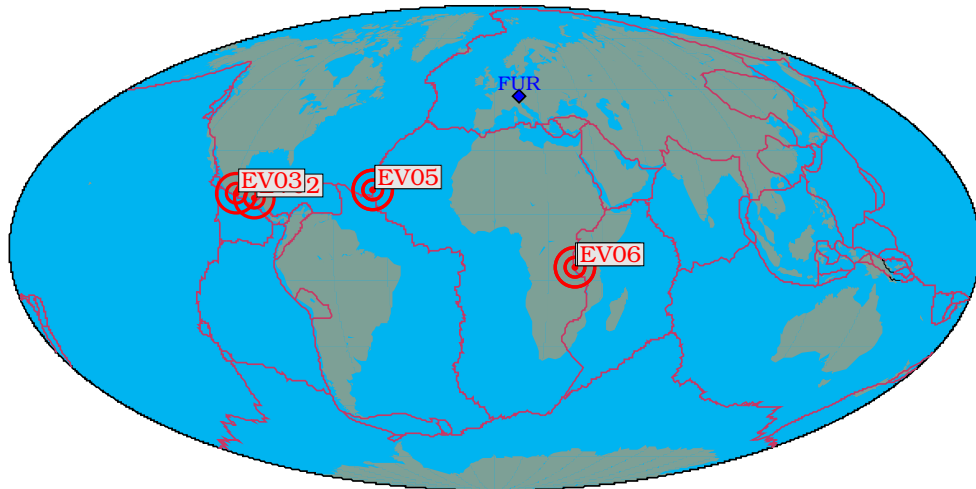


Figure 2.18: Example of the 24h-seismicity world map of the Geophysics Institute homepage. Epicenters are marked by concentric circles. The Lake Tanganyika earthquake is indicated by the label EV06.

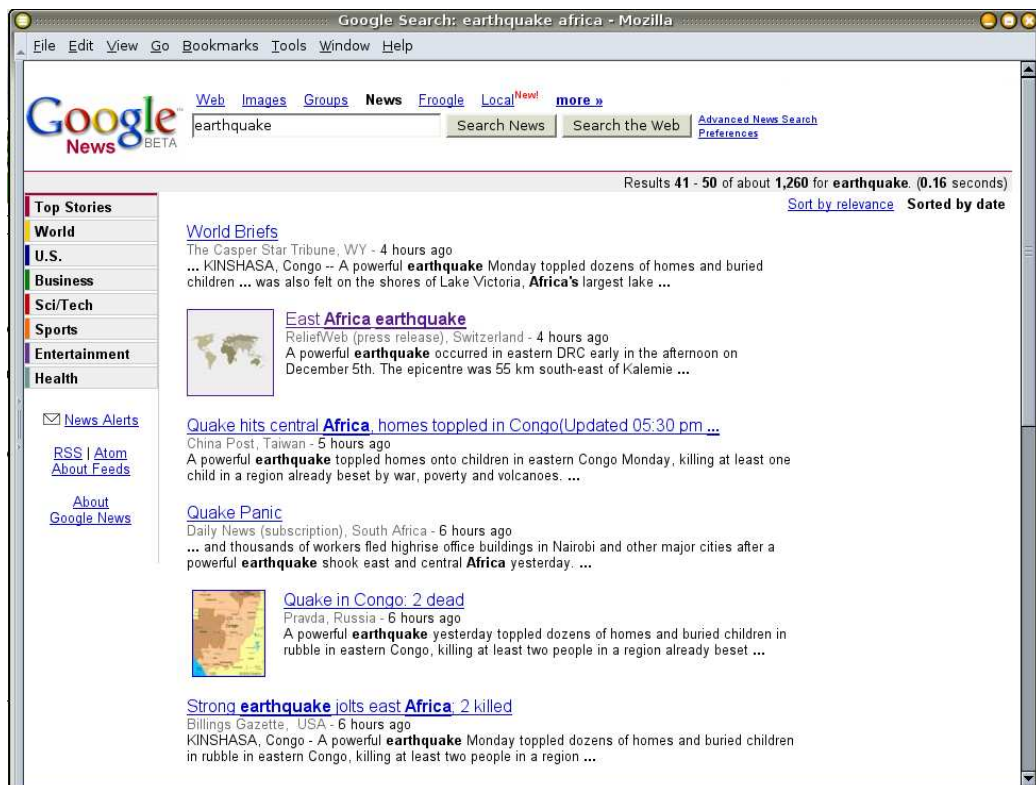


Figure 2.19: Example of the Google news ticker linked on the Geophysics Institute homepage. The Lake Tanganyika earthquake dominates the messages.

on the homepage. Figure 2.19 shows the search results of December 6, 2005, which are mainly related to the Lake Tanganyika event. It is also interesting to follow the reaction of the media after major earthquakes, which normally increase the number of reports on even tiny events that would otherwise not have been reported. Another enjoyable thing to read in the news ticker, is the non-earthquake related use of the word earthquake in many fields of everyday life.

2.5 Network Performance and Outlook

The key objectives of the new Bavarian Seismological Network were: (1) to update the instrumentation of the Bavarian seismological network to record local events with high resolution, (2) to increase the station density in areas of permanent seismic activity to be able to get reliable earthquake location and magnitude, (3) to install a data center at the Geophysical Observatory in Fürstfeldbruck to store and analyze data, and (4) to develop an infrastructure for the information of authorities and public.

As outlined in the previous section these goals were achieved successfully. The new Bavarian Seismological Network now provides a modern tool of seismological research and earthquake monitoring. The equipment of six existing stations was updated to state-of-the-art instrumentation and 15 new stations were installed. Thus, the seismological data of all 21 stations can be accessed at any time via telephone line and is presented in near-realtime on the internet. Furthermore, the network sensitivity was increased, which is indicated by the decrease of the statistically derived magnitude completeness threshold in the subnetwork of Bad Reichenhall to $ML=0.5$. However, a definite value for the entire Bavarian network can, not yet be given, as the number of recorded earthquakes is statistically insufficient at present.

A data center was installed at the Geophysical Observatory in Fürstfeldbruck, 25 km west of Munich, where the data of the new Bavarian Seismological Network is analyzed and stored. The data center is connected to the seismological stations via ISDN telephone line and can access the stations for data extraction and configuration purposes at any time. Highly sampled data is stored at the data center in an event data base, whereas a low-frequent sampled data-stream is transferred to the data center completely on a weekly basis.

Earthquake related information and seismological data is presented to the public on two internet portals. The homepage of the Bavarian Earthquake Service focuses on the seismicity of Bavaria and adjacent areas, whereas the homepage of the Geophysical Institute of the University of Munich places its main emphasis on global seismicity. Near-realtime seismogram data and current earthquake information is given on both websites. Additionally, two information centers were installed at the Geocenter in Windischeschenbach, N-Bavaria and in the salt museum in Bad Reichenhall. At these centers, posters and automatic slide shows give information on the seismicity of Bavaria.

The new Bavarian Seismological Network is also already accepted as an important scientific research instrument by the scientific community, as indicated by numerous data requests of scientists from many neighboring countries. Data exchange with the following institutions and project may stand as an example: Vogtland-project (Germany + Czech Rep.), Austrian earthquake service (ZAMG, Vienna), North Italian seismological network (OGS, Trieste), SZGRF (BGR, Hannover), earthquake service of Baden-Württemberg (LED, Freiburg).

The successful installation and good performance of the new Bavarian Seismological Network must, however, be considered as a first step toward a efficient earthquake monitoring instrument. At present analysis of the seismological data is an interactive process, which consists of: manual identification of an earthquake occurrence, manual download of the seismological data from relevant stations, interactive analysis of the data and manual estimate of the earthquake location and magnitude. The reason for this is mainly, that the seismological data is not available at the data center in real-time. Otherwise, already developed software could automatically screen the data, identify earthquake signals, analyze them and estimate the location and magnitude of the earthquake. The realization of this concept is, however, strongly dependent on the availability of fast internet connections between station and the data center, and last but not least, on the financial budget available to the Bavarian Earthquake service.

Part II

The 2002 Mt. Hochstaufen Earthquake Swarms

Chapter 3

Meteorological triggering of earthquake swarms at Mt. Hochstaufen, SE-Germany

A growing body of evidence suggests that fluids are intimately linked to a variety of faulting processes. Yet, the particular mechanisms through which fluids and associated parameters influence the stress regime and thus the seismicity of a particular area are not well understood. We carry out a study of the spatio-temporal behavior of earthquakes, fluid-related parameters (groundwater levels) and meteorological observables (precipitation) in the swarm earthquake area of Bad Reichenhall, southeastern Germany. The small volume in which the earthquakes take place, almost yearly occurring earthquake swarms and a permanent, seismo-meteorological monitoring network, provide nearly controlled experimental conditions to study the physics of earthquake swarms and to infer characteristic properties of the seismogenic crust. In this paper we (1) describe this fairly unique study area in terms of geology, seismicity and atmospheric conditions; (2) present two cases of earthquake swarms that seem to follow above-average rainfall events; and (3) examine the observed migration of hypocenters with a simple pore-pressure diffusion model. We find significant correlation of seismicity with rainfall and groundwater-level increase, and estimate an average hydraulic diffusivity of $D = 0.75 \pm 0.35 \text{ m}^2/\text{s}$ for Mt. Hochstaufen in 2002.

This chapter was published as: KRAFT, T., J. WASSERMANN, E. SCHMEDES AND H. IGEL (2006), *Meteorological triggering of earthquake swarms at Mt. Hochstaufen, SE-Germany*, *Tectonophysics*, **424** (3-4), pp.245–258, doi:10.1016/j.tecto.2006.03.044

3.1 Introduction

By observing hydrothermal precipitants in mineral veins, mining geologist had for centuries achieved a quantitative appreciation of the role of fluid pressure in counteracting normal stress during faulting. The seminal paper by *Hubbert and Rubey* [1959] stands out as the foundation work in structural geology applying the concept of effective stress [*Terzaghi*, 1923] in a quantitative manner to faulting in fluid-saturated rock. They identified the development of fluid pressures to near-lithostatic levels as an important mechanism for lowering the strength of overthrust faults.

In recent years, hydromechanical coupling has been proposed as a possible explanation for several geological phenomena [e.g., *Neuzil*, 2003], including the anomalous weakness of many major faults, fault creep, slow earthquakes, or afterslip [e.g., *Sleep and Blanpied*, 1992; *Byerlee*, 1993]; silent slip events observed by GPS surveys [e.g., *Kodaira et al.*, 2004]; seismicity patterns of aftershocks [e.g., *Nur and Booker*, 1972; *Miller et al.*, 2004] and remote triggering of earthquakes by transient dynamic stress fields [e.g., *Prejean et al.*, 2004]. Direct evidence of the effects of fluid pressure on fault stability has come from earthquakes induced in intraplate regions (e.g., reservoir induced seismicity [e.g., *Howells*, 1974; *Ferreira et al.*, 1995; *Talwani*, 2000], fluid injections in wells [e.g., *Baisch et al.*, 2002; *Rothert and Shapiro*, 2003] and increase in hydraulic head or stream discharge connected with microseismicity [e.g., *Roeloffs et al.*, 2003; *Manga et al.*, 2003].

Another phenomenon that is thought to be linked to hydromechanical coupling is the occurrence of earthquake swarms. These are sequences of earthquakes that often start and end gradually and in which no single earthquake dominates the size [*Scholz*, 1994]. Earthquake swarms are a globally observed phenomenon and are commonly associated with volcanic regions [*Sykes*, 1970]. The temporal evolution of swarm activity can not be described by any simple law, as e.g. the Omori law for aftershock sequences. Furthermore, the frequency-size distributions of earthquake swarms are normally characterized by unusually large b-values [*Sykes*, 1970].

Several mechanisms have been proposed for earthquake swarm generation. *Mogi* [1963] suggested that in highly fractured regions stress concentrations around fractures promote failure already under small stresses without the occurrence of large rupture surfaces. Other models are based on the Mohr-

Coulomb failure theory in its effective stress formulation. *Hill* [1977] proposed a model for volcanic regions, which assumes a system of magma-filled dikes interconnected by stress-field-oriented fractures that rupture under certain pore pressure conditions in the dike. *Yamashita* [1999] suggested that swarm-like sequences could be created by fluid flow from localized high pressure compartments controlled by permeability increase due to fracturing.

In this study we investigate the spatio-temporal behavior of earthquakes, groundwater levels, precipitation and their correlations in the swarmquake area of Bad Reichenhall, in southeastern Germany. The aim of this paper is (1) to describe this fairly unique study area in terms of geology, seismicity and atmospheric conditions; (2) to present two cases of earthquake swarms that seem to follow above-average rainfall events; and (3) to examine the observed migration of hypocenters with a simple pore-pressure diffusion model.

3.2 The Study Area

3.2.1 Geography, Morphology, Tectonics and Geology

The Staufen Massif is an east-west striking mountain chain in southeastern Germany, northwest of Bad Reichenhall. The highest summit on this 10 km long ridge between the communities of Piding and Inzell is Mt. Hochstausfen (1775m). Though situated directly at the morphological northern margin of the Alps, its morphology is of a remarkably High-Alpine character, which is emphasized by the high topographic gradients of the northern and southern flanks, as well as the low lying Reichenhall Basin in the south. The difference in altitude between the city of Bad Reichenhall and the summit of Mt. Hochstausfen is nearly 1200m.

We will only briefly outline the tectonic setting and the geology of the Staufen Massif, a detailed description can be found in e.g., *Erhardt* [1931], *Henrich and Zankl* [1981] and *Weede* [2002]. The Northern Calcareous Alps (NCA), a part of the Austroalpine Mega-Unit, are an elongate fold-and-thrust belt with a complex internal structure and are classically subdivided into four nappe units: the Bavaric, Tirolic, Lower- and Upper Juvavic Units [Fig. 3.1, for details e.g., *Tollmann*, 1976]. The Staufen Massif is part of the Tirolic facies, which overthrusts the intensely folded Bavaric Unit. In the eastern part of the Staufen Massif the Bavaric Unit was completely traversed. There, the Tirolic Unit is in direct contact with the Flysch Zone

in the North. The southern border to the Juvavic Units is built by the northeast striking Saalach Western Fault and Kugelbach Zone. The later widens in the east to form the Reichenhall Basin with salinar sequences of remarkable thickness, which explain the increased mobility of the tectonic units in the region [Zankl and Schell, 1979].

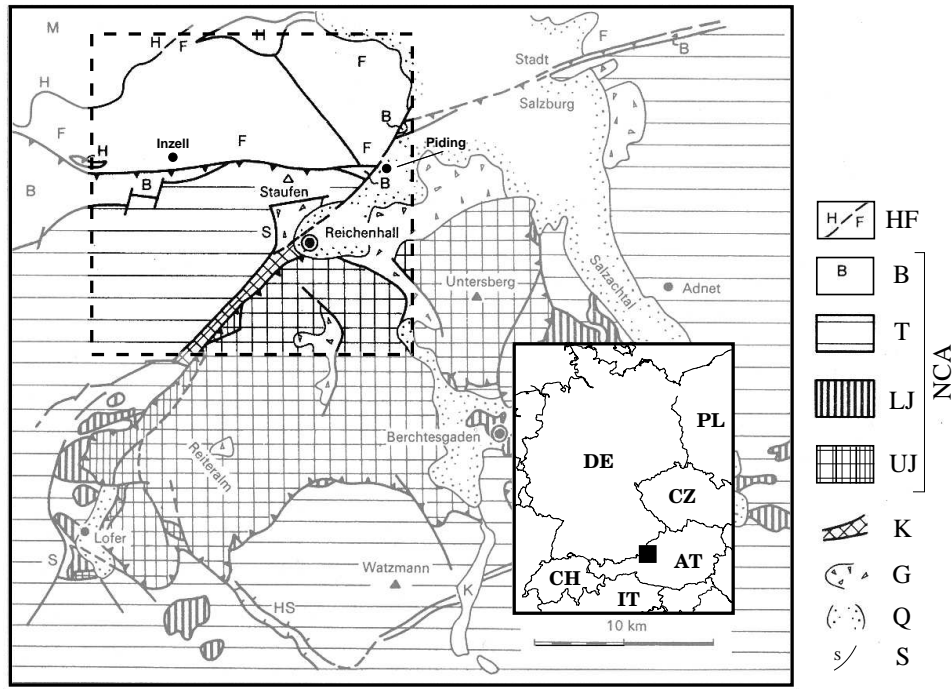


Figure 3.1: Tectonic map of the region around the study area [modified from Bögel and Schmidt, 1976]. The classical subdivision of the Northern Calcareous Alps (NCA) in four nappe units is indicated. The study area is marked by a dashed square. The insert map gives the geographical location of the tectonic map. **HF** Helvetic Unit and Flysch Zone; **B** Bavaric, **T** Tirolic, **UJ** Upper and **LJ** Lower Juvavic Units; **K** Kugelbach Zone; **S** Saalach Western Fault; **G** Gossau conglomerates; **Q** Quaternary sediments.

The Staufen Massif is made up of a stratigraphic sequence from the lower to middle Triassic (Fig. 3.2). It predominantly consists of limestone and dolomite, which in some stratigraphic units alternate with marl, clay and sandstone. The summit region consists of Wettersteinkalk (limestone), which shows distinct signs of Karst formation. Haselgebirge, a leached and weathered breccia of evaporitic permo-triassic sediments, can be found in some outcrops on the northern flank of the Staufen Massif and in the Reichenhall Basin. Presumably, Haselgebirge also exists in the innermost fold

cores of the Staufen Massif [Weede, 2002]. A schematic cross section and stratigraphy of Mt. Hochstaufen is shown in Figure 3.2.

Geologic evidence for mass movements at the southern flank of Mt. Hochstaufen was recently summarized by Weede [2002]. Large east-west striking open fractures can be found near the summit of Mt. Hochstaufen. They reach a length of several hundred meters and openings of up to three meters. Speleologists were able to follow those fractures to a depth of nearly 100 meters below the surface [Glaser, 2004]. Gravitational collapse and/or subsidence due to leaching of the Haselgebirge are debated as causative processes.

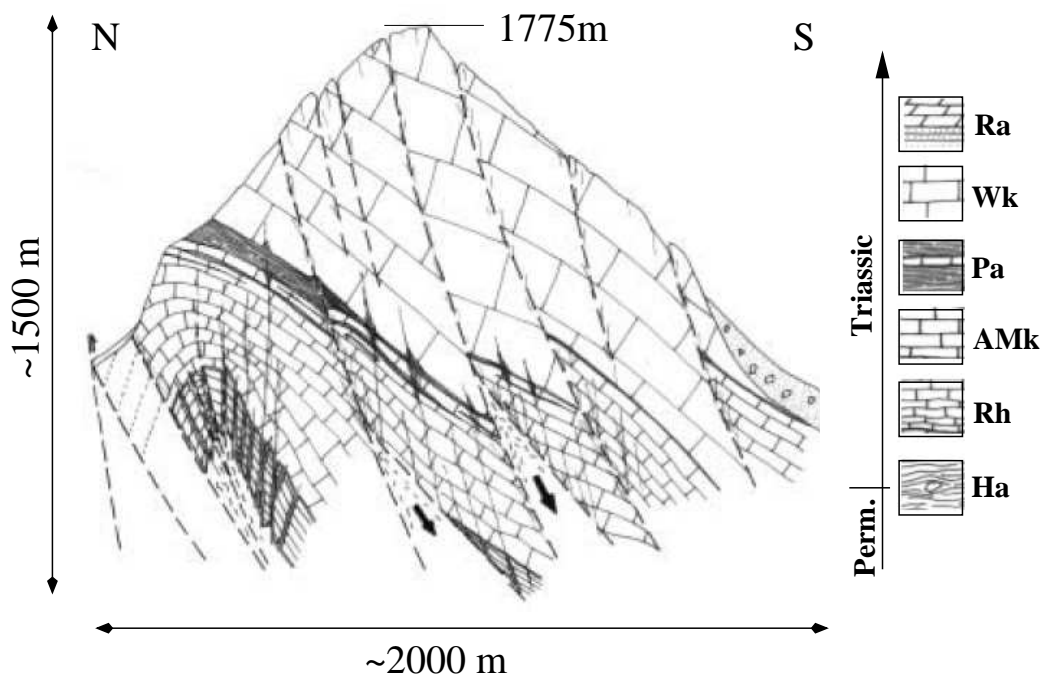


Figure 3.2: Schematic geological cross section of Mt. Hochstaufen [modified from Weede, 2002]. **Ra:** Raibler Formation; **Wk:** Wettersteinkalk (Limestone); **Pa:** Partnach Formation; **AMk:** Alpine Muschelkalk (Limestone); **Rh:** Reichenhall Formation. For a detailed lithology refer to *Henrich and Zankl* [1981].

3.2.2 Previous Studies and Seismicity

Reports of felt earthquakes in the area of Bad Reichenhall range back to October 16th, 1390, which is also the first record in the Bavarian earthquake catalog. Although the list of macroseismically observed earthquakes is certainly not complete, all of the 30 reported events (Fig. 3.3) were surely only felt in the vicinity of the city of Bad Reichenhall. The maximum intensity

reached was $I_0 = V$ on the macroseismic scale. As illustrated in Figure 3.3, the majority of these earthquakes occurred in the summer months which are also characterized by having the highest average precipitation values.

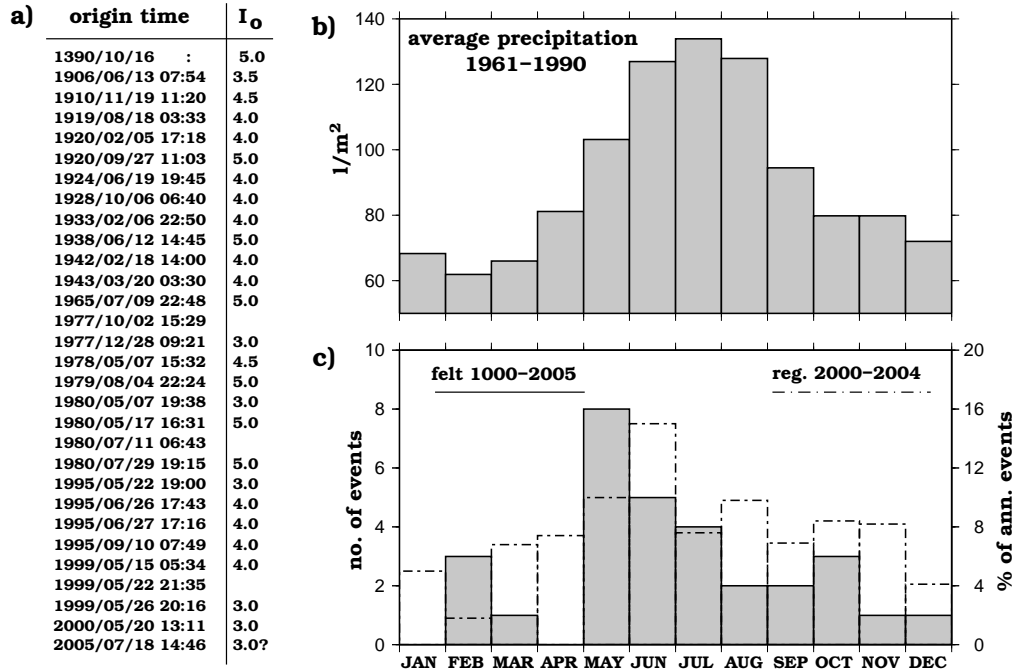


Figure 3.3: Macroseismicity of the Bad Reichenhall area between 1000 and 2005. **a)** List of origin time and maximum macroseismic intensity I_0 of earthquakes reported felt in Bad Reichenhall. **b)** Precipitation in the reference period 1961 to 1990 for the Alps [Fuchs et al., 1999]. **c)** Histogram of earthquakes in a) and dash dotted histogram of monthly percentage of annually registered earthquakes between 2001 and 2004 at station STAU.

This observation and the confined anomalous character of the seismic activity encouraged first interpretations considering the local geological setting. Giessberger [1918] proposed cavity collapses caused by solution of salt from the Haselgebirge formation in the Reichenhall Basin as a causative mechanism. Schmedes [1979] additionally suggested corresponding processes during Karst formations of the Lattengebirge mountains in the south and gravitational subsidence of the overlying rock due to leaching of the Haselgebirge formation.

In February 1972 a short period seismometer was installed in the old salt refinery in Bad Reichenhall. The instrument had only a vertical component which did not allow earthquake location or determination of focal mecha-

nisms. Nevertheless, *Schmedes* [1979] was able to verify the temporal pattern in seismic activity characterized by relative quiescence in the beginning of the year and an annual maximum in summer. He also reported for the first time on the occurrence of earthquake swarms in the Bad Reichenhall area.

A mobile network consisting of digital seismograph stations was installed in a widespread area around Bad Reichenhall in 1978 [*Schmedes*, 1979]. Using data of this network from the time period from 1978 to 1980, *Nöthen* [1981] showed that the seismicity of the study area was mainly concentrated in the Staufen Massif north of Bad Reichenhall. He concluded from calculated focal mechanisms that tectonic slip events dominate the seismicity and excluded the earlier proposed explanation of cavity collapses.

On June 26th, 1995, a magnitude $ML=2.7$ earthquake was located and felt in Bad Reichenhall. The next day the University of Munich installed a dense mobile seismological network around the Staufen Massif. In a detailed study of the recorded data of the two months deployment time *Schwarzmann* [1996] found that the seismicity is confined to shallow depth (above 2.5 km) and concluded from the variety of calculated focal mechanisms that it was bound to different independent fault planes. She also found weakly significant ($c_{max} = 0.6$, c_{max} : maximum cross correlation coefficient) and close correlation ($c_{max} = 0.8$) of seismicity with precipitation and associated groundwater level for a 15 years period starting in 1980, and suggested a causal connection between seismicity and rainfall in the study area.

However, what was missing is a long-term observation of the Bad Reichenhall area in terms of seismicity, meteorological parameters and associated hydrological observables. Only the recording of complete swarm sequences by such a dense and permanent "seismo-meteorological" network can help to identify and understand the processes that drive swarm-type seismicity in the Staufen Massif.

3.2.3 Seismo-Meteorological Network

Previous studies, mentioned above, have emphasized the need of multi disciplinary and permanent monitoring of the Bad Reichenhall area. Beginning in 2001 a "seismo-meteorological" network was installed in the study area. It consists of three parts which are described in the following.

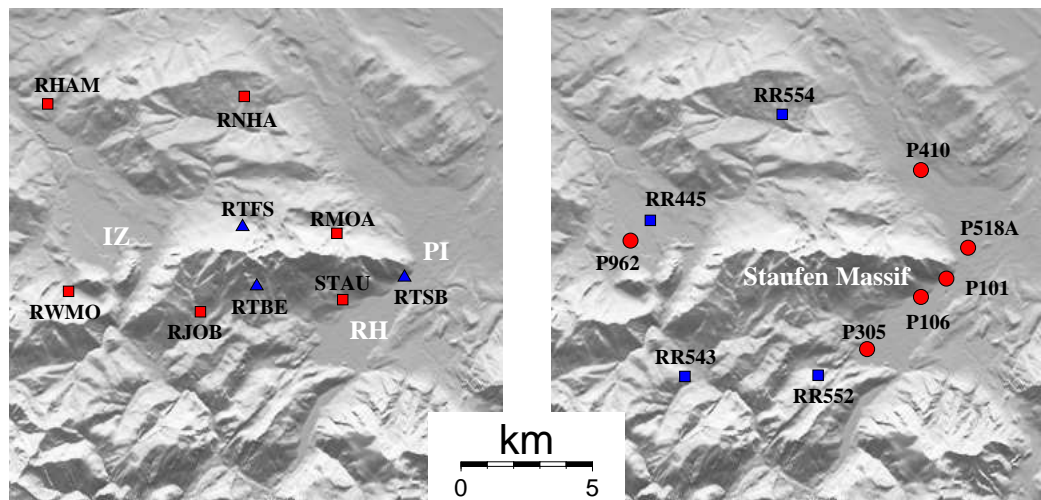


Figure 3.4: Seismo-meteorological network around Mt. Hochstaufen. Map borders: lon. $12^{\circ}40' - 12^{\circ}57'E$; lat. $47^{\circ}40.5' - 47^{\circ}55.5'N$. **Left:** Map of permanent (squares) and mobile (triangles) seismological stations recording in 2002. The cities Inzell (IZ), Piding (PI) and Bad Reichenhall (RH) are indicated. **Right:** Hydrological (circles) and meteorological (squares) stations.

Seismology:

In 2001, the University of Munich in cooperation with the Geological Survey of the Bavarian State installed a new seismological network in Bavaria. It now consists of 21 stations which send their data in near real time to the data center in the Geophysical Observatory in Fürstfeldbruck via telephone line. A subnet consisting of six short period stations was installed around the Staufen Massif. To close some gaps in the station coverage, arising from the high level of infrastructure required for the permanent stations (power and telephone lines), we installed three additional mobile stations starting in mid-April 2002. All mobile stations were deployed in open field close to the source region of the swarm-earthquake activity. Data was recorded in continuous mode with a sample rate of 125Hz and 200Hz. All station locations are given in Figure 3.4.

Meteorology:

The German Weather Service (DWD) operates a dense network of meteorological stations in Germany. In our study area four pluviometer stations are available. Precipitation is read off manually every 24 hours at 6:30 local time. Data of these stations was made available by the DWD in digital form. A map of all stations can be found in Figure 3.4.

Hydrology:

The Bavarian Bureau of Water Resources (WWA) and the SüdSalz GmbH (SUD, salt refinery in Bad Reichenhall) provided data of groundwater gauges located around the Staufen Massif. The wells are between five and fifty meters deep. The three shallow wells operated by the WWA in our study area register the groundwater level on paper records. In the Bad Reichenhall basin the groundwater level in several deep wells is read off by SUD manually on a daily basis. The data was provided in the form of error-corrected plots, which were scanned and digitized for further analysis. The resolution of both datasets is one centimeter in groundwater level and approximately one day in time. All groundwater well positions are given in Figure 3.4. Information on station coordinates and instrumentation as well as access to near-realtime seismograms is available via internet (www.erdbebendienst.de).

3.3 The 2002 Earthquake Swarms

In March and August 2002, intense rainfall events led to severe flooding in Central Europe, causing an economic damage of 18.5 billion Euro [*Munich Re Group*, 2003]. Precipitation in the study area exceeded the monthly average within 48h, respectively 24h, during these events. As illustrated in Figure 3.6 and Figure 3.7a,b the seismicity in the Hochstaufen mountain range increased significantly after both rain events. A detailed analysis of the resulting earthquake swarms, which were recorded with the "seismo-meteorological" network, will be presented in the following.

3.3.1 Data Analysis, Derivation of Velocity Model

An event list generated automatically at station STAU (southern flank, permanent) and manually at station RTFS (northern flank, mobile) built the basis for the extraction of local earthquakes (epicentral distances smaller than ~ 15 km) from the continuous recordings. Extracted waveforms were usually one minute in length, and stored in an event database in GSE format using the software package GIANT [*Rietbrock and Scherbaum*, 1998].

We manually picked arrival times of P- and S-phases for all recorded earthquakes. The accuracy of the best readings reached the sampling distance (0.05-0.08 s). Weights from 0 (best) to 4 (neglected; uncertainty > 0.3 s) were assigned to the arrival-times. Local magnitudes were calculated after *Bakun and Joiner* [1984]. Estimates of hypocentral distance from the dif-

ference of arrival times of the P- and S-phases allowed magnitude estimates for events recorded only at one station. Such events were identified as being local earthquakes by the similarity to waveforms of events recorded on more than one stations.

A homogeneous half-space velocity model was derived in a coupled hypocenter-velocity inversion using the VELEST algorithm [Kissling *et al.*, 1994] for well determined events. These were defined by having a station gap less than 180° and a number of travel-time observations ≥ 6 , and were found in repeated VELEST runs. The resulting so-called *minimum-1D-velocity model* ($v_p = 5.6\text{km/s}$; $v_s = 3.1\text{km/s}$; $v_p/v_s = 1.81$) represents the least-squares average velocity of the region that is sampled by seismic rays [Kissling *et al.*, 1994]. The derived velocity model oversimplifies the velocity structure of the study area. However, we think its use is justified for standard earthquake location because the seismicity and the seismological network are predominantly confined to one lithological unit (Northern Calcareous Alps), having a small source volume, and a close station spacing respectively.

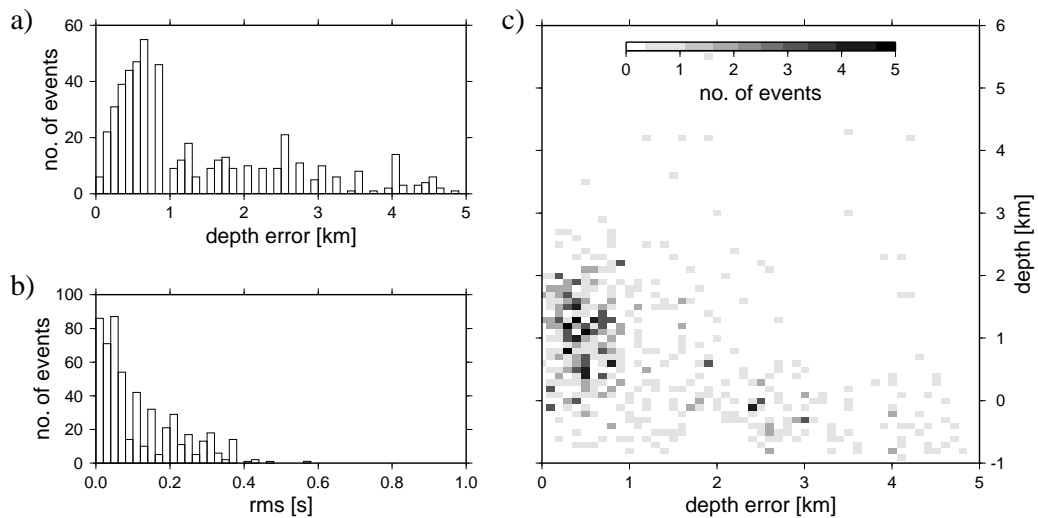


Figure 3.5: Location error obtained with Hypo71 [Lee and Lahr, 1975] and the *minimum-1D-velocity model* for Mt. Hochstaufen earthquakes in 2002. Histogram of **a)** root-mean-square (rms) error sum of differences between and calculated observed travel times, and **b)** depth error. **c)** Scatter plot of depth error versus hypocenter depth.

The *minimum-1D-velocity model* was used for standard earthquake location with the program Hypo71 [Lee and Lahr, 1975]. 546 earthquakes with a

minimum of six observed arrival-time readings could be located. As topography was not taken into account, the calculated depth $d_{H71}(j)$ represents the depth below the average elevation $\Delta_{mean}(j)$ of the stations contributing to the solution. The absolute depth $d(j)$, which is used in the following, is then calculated for each event j as $d(j) = d_{H71}(j) - \Delta_{mean}(j)$. The overall mean station elevation is -793m (depth positive down).

Figure 3.5 illustrates the location quality obtained for the 2002 Hochstaufen earthquakes. The root-mean-square (rms) errors of the differences between calculated and observed travel times are small, mainly below 0.1 s (Fig. 3.5b), and indicate good quality of onset-time determination. For the majority of the events the depth errors, calculated with Hypo71 [Lee and Lahr, 1975], is less than 1 km (Fig. 3.5a) indicating fairly good location results. Greater errors are observed especially for very shallow events above and slightly below sea level (Fig. 3.5c). This is due to the fact, that for shallow events the relative travel-time error is larger than for deep events, because the travel times become very short. In the following derivation of hydraulic parameters we will therefore introduce weighting and neglect events with depth errors greater than 3 km.

3.3.2 Observed Seismicity

In 2002, 1171 earthquakes were recorded in the study area. The strongest event had a magnitude of $ML = 2.4$ on April 10. From the magnitude-frequency statistics we assume the recorded dataset to be complete down to a magnitude of $ML = -0.5$. The epicenters of the located events are diffusely distributed over the Staufen Massif (Fig. 3.6). Their source depths rarely exceed 3 km below sea level (Fig. 3.7d). We estimated the stability of the location result by relocating the events using different initial hypocenters. For the majority of the events a lateral change of less than 500m was observed.

The spatio-temporal behavior of the seismicity is illustrated in Figure 3.7. Figure 3.7a displays the mean of four pluviometers operated by the DWD in the study area (see Fig. 3.4). Most of the events can be assigned to swarm-quake phases in March and August, which were following above-average rainfall events. Both events were characterized by exceeding the monthly average of precipitation within 48h, respectively 24h. The number of earthquakes per day in Figure 3.7b illustrates the seismic activity. It increased roughly coincident with the onset of the intense rain events. In both cases

seismicity reached its maximum approximately ten days after their onsets and stayed on an elevated level for several weeks.

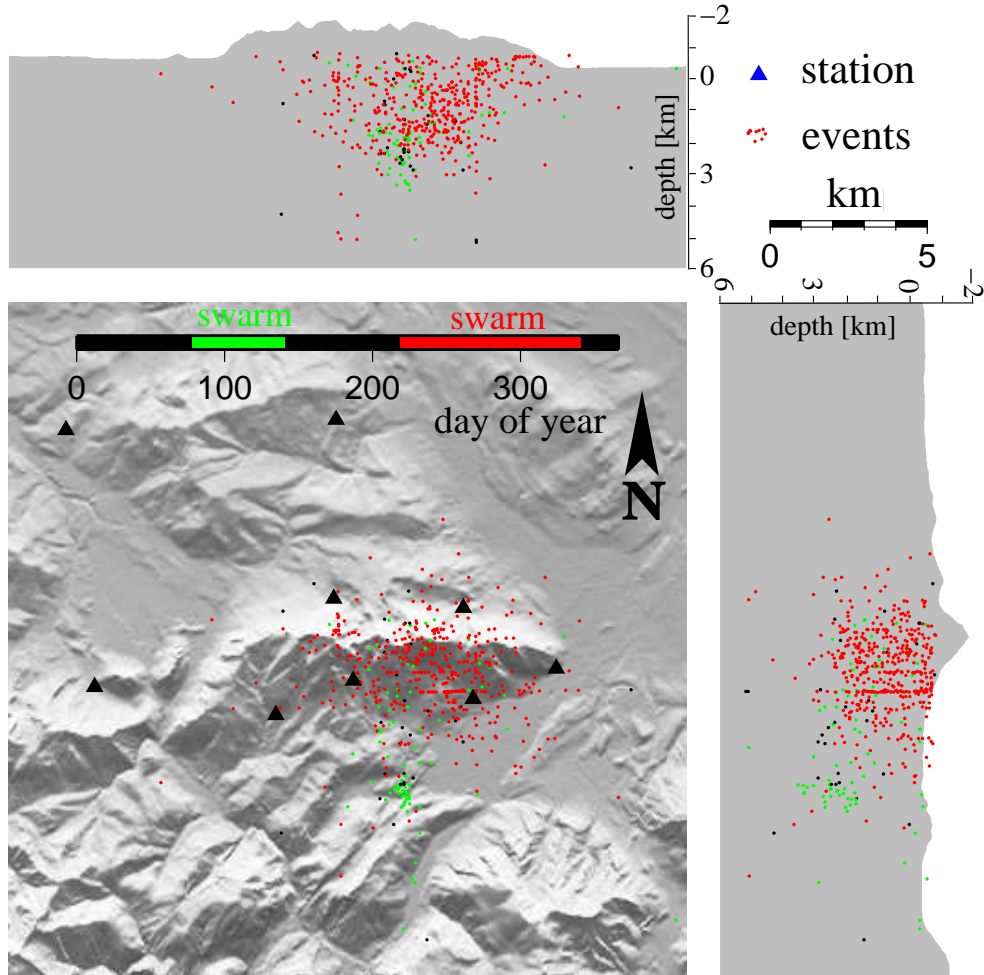


Figure 3.6: Epicenters of 546 earthquakes in 2002 located using Hypo71[*Lee and Lahr, 1975*] and the derived *minimum-1D-velocity* model. Colors identify two swarm-earthquake periods. Green: March swarm (~ 80 events); red: August swarm (~ 430 events); black: background seismicity (~ 40 events). Triangles mark seismological stations installed in 2002. Map borders: lon. $12^{\circ}40' - 12^{\circ}57'E$; lat. $47^{\circ}40.5' - 47^{\circ}55.5'N$. E-W and N-S profiles through the summit of Mt. Hochstaufen (1775m)

The first swarm in March was mainly concentrated on a small volume of approximately one cubic kilometer. The centroid was located further south and in a significantly less elevated region as usually observed in earlier studies and for the subsequent swarms in August (see Fig. 3.6). This may be due to the fact that precipitation in the elevated parts of the study area

fell as snow or an interaction of the beginning snowmelt with the intense rainfall in the lower part of the study area.

The second earthquake swarm starting in August can be divided into three sub-swarms. The first one contains most of the recorded earthquakes. Within this sub-swarm the data suggests a migration of hypocenters over time. From very shallow depth west of the summit region of Mt. Hochstaufen they move to depths of 2.5 km in a southeast direction within about five days. The hypocenter migration is illustrated by red arrows in Figure 3.7d-f. The increased seismicity makes it difficult to clearly identify a similar behavior for the following sub-swarms.

However, as illustrated in Figure 3.8 each swarm and sub-swarm can be associated with an event of strong rainfall, as well as increasing groundwater level. To assure the comparison of evenly sampled time series within comparable frequency bands, we preprocessed the time series of precipitation (R, Fig. 3.7a), seismicity (EG, Fig. 3.7b), and groundwater-level increase rate (ΔG^+) with gaussian filters of different lengths (see Tab. 3.1). Further, lower threshold levels (see caption to Fig. 3.8) were introduced to reduce uncorrelated background noise. Figure 3.8 visualizes the resultant normalized time series for a filter length of ten days as colorcoded horizontal bars. The seismicity bar was time shifted by ten days according to best-lagged cross-correlation result (see Tab. 3.1). Clearly the good temporal agreement of maxima in the different timeseries (vertical white stripes) can be seen.

The quantitative results of the cross-correlations for the different time series preprocessed with different filter lengths are given in Table 3.1. Best time lags between nine and eleven days for seismicity against precipitation and ΔG^+ are obtained. Precipitation and ΔG^+ correlated best with zero delay. The cross correlation coefficients (c_{max}) increase with increasing filter length due to smoothing of the time series. Consequently however, the accuracy of the delay time estimation decreases. To balance this tradeoff for visualization we choose a filter length of 10 days in Figure 3.8, which results in $c_{max} > 0.70$ for all timeseries and still allows their detailed comparison.

Cross-correlation analysis assumes a linear relation between time series, which can only be a first order approximation in our case. However, the significant correlation of seismicity with precipitation and ΔG^+ , and its time delay of 9–11 days suggest, that diffusive hydraulic processes can trigger

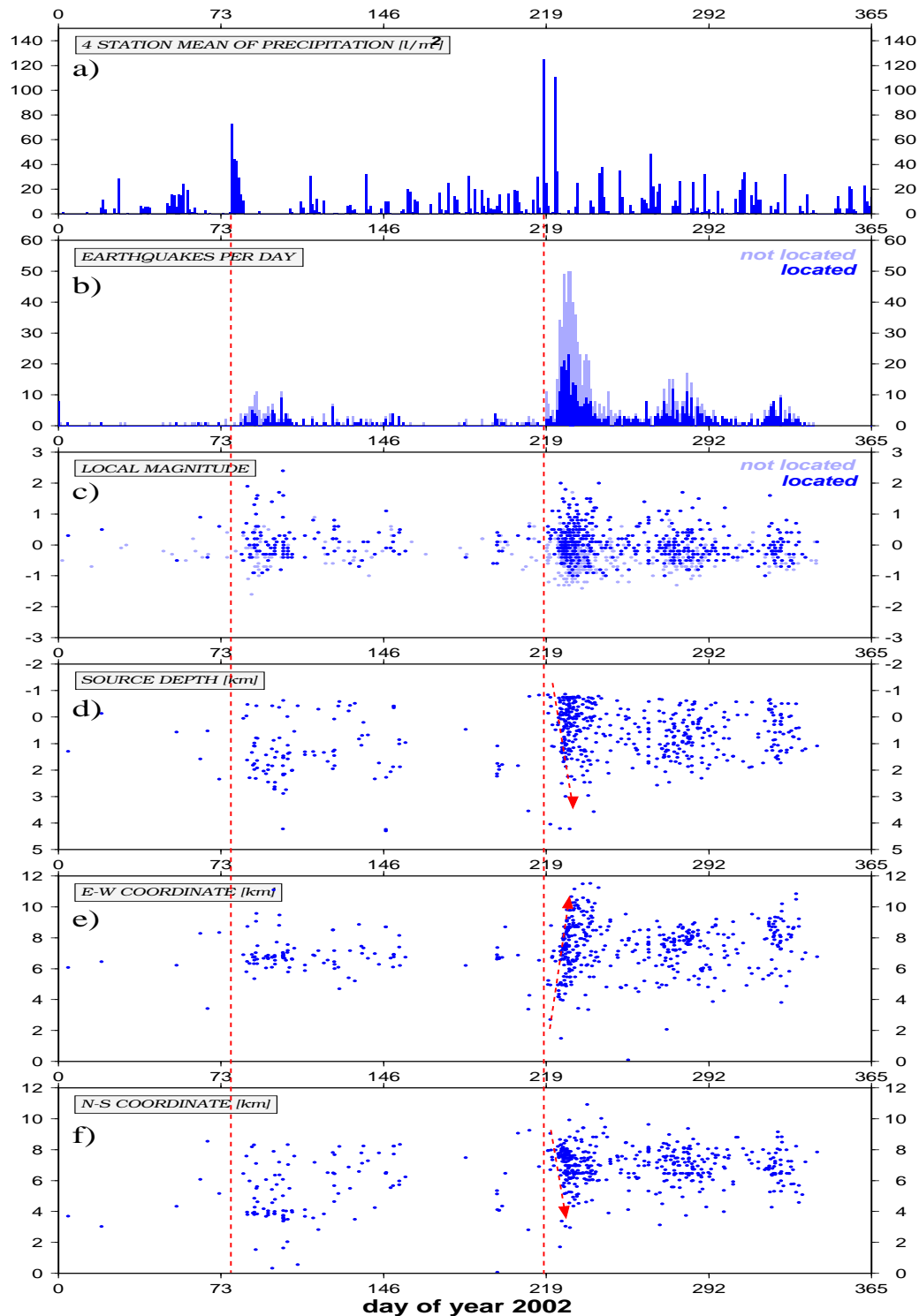


Figure 3.7: Spatio-temporal development of the seismicity in 2002. Vertical red lines mark the onsets of intense rain events in March and August. Dashed arrows illustrate the migration of hypocenters with time into depth (d), to the east (e), and to the south (f) for the first sub-swarm in August.

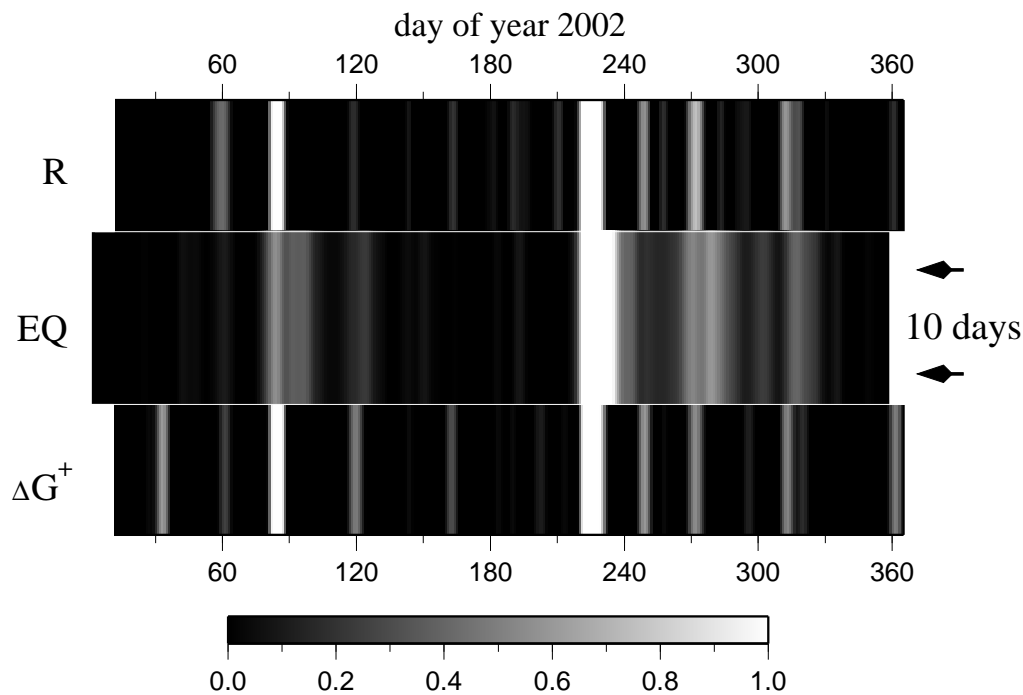


Figure 3.8: Gray scaled normalized time series of precipitation \mathbf{R} , seismicity \mathbf{EQ} , and increase rate of groundwater level of well P518A in Piding (see Fig. 3.4) ΔG^+ for 2002. Time series are gaussian filtered (10 days). Lower thresholds: R: 8%; EQ: 2%; ΔG^+ : 18% (and upper threshold for this figure: EQ: 50%) were applied. \mathbf{EQ} is time shifted by 10 days for maximum correlation (compare Tab. 3.1). The gray scale used is indicated.

swarm-type earthquake activity in the Staufen Massif. We will discuss a possible mechanism in the following.

3.4 Hydrological Interpretation

It is widely accepted, that increase in pore fluid pressure reduces the shear strength of a porous medium by counteracting normal stress. This is known as the concept of effective stress originally formulated by *Terzaghi* [1923]. If a porous medium is stressed to nearly critical values even a small increase of pore pressure can provoke failure [e.g., *Segall*, 1985; *Roeloffs*, 1988; *King et al.*, 1994; *Harris*, 1998].

Pore-pressure diffusion as triggering mechanism has been proposed for many case studies; e.g., aftershocks of strong earthquakes [e.g., *Nur and*

Gauß	1	4	8	10	15	20
EQ/R	9 (0.44)	9 (0.55)	10 (0.74)	10 (0.78)	11 (0.83)	11 (0.87)
$EQ/\Delta G^+$	9 (0.47)	9 (0.60)	10 (0.67)	10 (0.72)	11 (0.78)	11 (0.83)
$R/\Delta G^+$	0 (0.66)	0 (0.89)	0 (0.94)	0 (0.94)	0 (0.95)	0 (0.95)

Table 3.1: Cross-correlation result for precipitation \mathbf{R} , seismicity \mathbf{EQ} , and increase rate of groundwater level of well P518A in Piding (see Fig. 3.4) ΔG^+ for 2002. Time series are gaussian filtered (length of filter in days is given in the first row). Lower thresholds: R: 8%; EQ: 2%; ΔG^+ : 18% were applied. Best time lags in days and corresponding maximum cross-correlation coefficient (in parenthesis) are given.

[Booker, 1972; Bosl and Nur, 2002; Shapiro et al., 2003], reservoir induced [e.g., Howells, 1974; Ferreira et al., 1995; Talwani, 2000], and fluid-injection induced [e.g., Shapiro et al., 1997; Rothert and Shapiro, 2003] earthquakes, changes of water table or stream discharge connected with microseismicity [e.g., Costain and Bollinger, 1991; Lee and Wolf, 1998; Braitenberg, 2000], intraplate earthquake swarms [e.g., Parotidis et al., 2003], as well as observations of seasonality in seismicity correlated with snowmelt [e.g., Saar and Manga, 2003; Wolf et al., 1997] or precipitation [e.g., Roth et al., 1992; Muco, 1995, 1999; Ventura and Vilaro, 1999].

We also assume that pore-pressure diffusion is a possible mechanism for triggering swarm activity in our study area. Consequently, as a first step we model the intense rain events as step increases in fluid pressure at the surface of a homogeneous half space and consider one-dimensional diffusion only. In doing so we will follow the notation and definition given in the review paper by Kümpel [1991].

The time-dependent interaction of fluid flow and rock deformation is described by the theory of poroelasticity [Biot, 1962]. In a source free, homogeneous half space, with scalar hydraulic diffusivity D , the low frequency evolution of pore pressure P due to irrotational flow can be described by the diffusion equation [e.g., Wang, 2000]:

$$\frac{\partial P}{\partial t} = D\nabla^2 P \quad (3.1)$$

For a periodic pore pressure variation $P(0, t) = P_s \exp(i\omega t)$ at the surface of the half space the solution to Eq. (3.1) is given by [e.g., *Wang*, 2000, pp.140-143]:

$$P(z, t) = P_s \exp(-z\sqrt{\frac{\omega}{2D}}) \exp(i\omega(t - \frac{z}{\sqrt{2\omega D}})) \quad (3.2)$$

This is a plane wave with attenuation coefficient equal to $\sqrt{\omega/(2D)}$ and with a velocity of $\sqrt{2\omega D}$. Z is depth, t is time and ω angular frequency.

An estimate of diffusivity D can be obtained using the following logic, originally formulated by *Shapiro et al.* [1997]: A first order approximation of the injection signal (increase of pore pressure at the surface due to intense rainfall) is a rectangular pulse starting at the same time as the rain event $t = 0$ and ending at some time $t = t_e$ after the end of precipitation. However, for an earthquake triggered at time $t = t_0$ the evolution of the injection signal for times $t > t_0$ is not relevant. Hence, for this event the injection signal duration can be set to t_0 . The dominant frequencies of the power spectrum of a rectangular pulse with duration t_0 are in the range $0 \leq \omega \leq 2\pi/t_0 \equiv \omega_0$. From Eq. (3.2) one finds that the propagation velocity of pore pressure variations is proportional to $\sqrt{\omega}$. Further, we expect that even a small increase in pore fluid pressure can trigger seismicity. Consequently, we set $\omega = \omega_0 \equiv 2\pi/t_0$ to calculate the velocity of a triggering front behind which seismicity can be induced from Eq. (3.2). Doing this for the time range $t_0 \in [0, t]$ we find the time-depth dependence of the triggering pore pressure front:

$$z = \sqrt{4\pi Dt} \quad (3.3)$$

Hydraulic diffusivity can now be estimated by finding the triggering front parabola of form Eq. (3.3) that best separates the area of elevated seismicity from the background seismicity in a time-depth plot.

Figure 3.9 shows time-depth plots for the intense rain events of March 19th, August 6th, September 23rd, and a stack of the three, including all located earthquakes of the following 40 days. This time window length was chosen to separate the sub-swarms in August. Delays between the rain events and the increase of seismicity seem to be indicated in Figs. 3.9a-d. However, a comparison with Figure 3.7b shows, that these gaps arise from

the lack of locateable events for that time. The delayed seismicity of the March swarm can be observed in both figures. There are several possible explanations for this which will be discuss below.

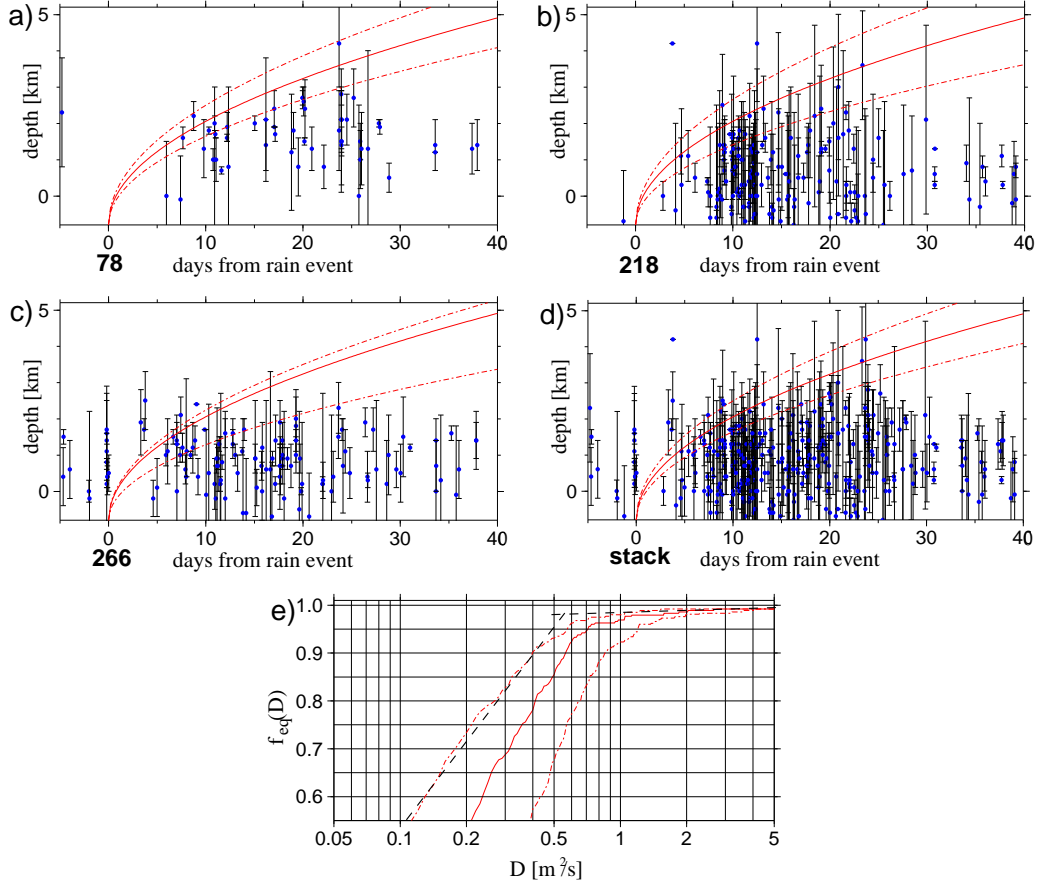


Figure 3.9: Time-depth plots for three earthquake swarm of 2002. Depth uncertainties due to standard earthquake location are indicated by error bars. Best fitting parabolas are shown for located depth plus error, located depth (solid), and located depth minus error. **a)** March 19th (day of year (doy) 78). D : $1.0 \text{ m}^2/\text{s}$, $0.75 \text{ m}^2/\text{s}$, and $0.55 \text{ m}^2/\text{s}$. **b)** August 6th (doy 218). D : $1.1 \text{ m}^2/\text{s}$, $0.75 \text{ m}^2/\text{s}$, and $0.45 \text{ m}^2/\text{s}$. **c)** September 23rd (doy 266). D : $0.85 \text{ m}^2/\text{s}$, $0.75 \text{ m}^2/\text{s}$, and $0.4 \text{ m}^2/\text{s}$. **d)** Stack of a, b, and c. D : $1.0 \text{ m}^2/\text{s}$, $0.75 \text{ m}^2/\text{s}$, and $0.55 \text{ m}^2/\text{s}$. **e)** Fraction $f_{eq}(D)$ of events below the triggering front parabola for stacked rain events ($D \in [0.05 \text{ m}^2/\text{s}, 5 \text{ m}^2/\text{s}]$). Dashed lines approximate $f_{eq}(D)$ (here e.g., upper error estimate), intersection point gives best estimate for D .

The fraction $f_{eq}(D)$ of events below the triggering front parabola was calculated as a function of diffusivity D in the range $0.05 \text{ m}^2/\text{s} \leq D \leq 5 \text{ m}^2/\text{s}$. Weights ($w = \frac{3-\Delta z}{3}$) were applied according to the depth location error Δz , and events with $\Delta z \geq 3 \text{ km}$ were neglected. In a semi logarithmic plot $f_{eq}(D)$

can be approximated by two straight lines (Fig. 3.9e), whose intersection point corresponds to the best estimate of D . The method was verified using different synthetic data sets composed of randomly distributed data points obeying the depth dependence in Eq. (3.3) and random background noise of different levels.

The best fitting parabolas are superimposed on the time-depth diagrams in Figs. 3.9a-d. We find a value of $D \simeq 0.75 \text{ m}^2/\text{s}$ in all investigated cases. Upper and lower error estimates for hydraulic diffusivity were derived by repeating the described algorithm for data sets with Δz added and subtracted. Extreme values for D are obtained for August 6th ($D = 1.1 \text{ m}^2/\text{s}$) and for September 23rd ($D = 0.4 \text{ m}^2/\text{s}$).

3.5 Discussion and Conclusion

The observations and first interpretations presented above indicate that seismicity in the Staufen Massif is influenced and partially even triggered by meteorological parameters. This is true for the long-term behavior of seismicity, as well as for episodic swarm-type activity as e.g., in March and August of 2002.

The comparison of long-term precipitation and seismicity in Figure 3.3 reveals the similarity in the annual record of both observables. The highest seismic activity is observed in the summer months, which are characterized by having the highest annual precipitation (Fig. 3.3b,c). The macroseismic record has insufficient events to be statistically significant. However, a maximum seems to develop in May, which precedes the maximum precipitation.

An explanation might be, that larger earthquakes are more likely to occur after periods of relative quiescence (the winter months) during which stress decomposition by small shocks is reduced. In Figure 3.3 also the maximum of the recorded seismicity seems to be ahead of the long-time average of the precipitation with a maximum in June. However, this may only reflect the fact that the time range for the recorded seismicity is much shorter than that for precipitation. Whether a similar explanation as given for macroseismicity above holds for microseismicity can not be answered until continuously recorded seismicity is available for a comparable range of time.

The high correlation of short-term episodic intense-rainfall events and swarmquake activity in 2002 is illustrated in Figure 3.8. Almost every rain

event matches a corresponding event in the time-shifted seismicity record. Nonlinear coupling of seismicity and precipitation as well as groundwater-level increase is most likely, because of the observed variances of delay times and amplitudes of the individual events. Furthermore, there are precipitation events and groundwater-level increases that are not followed by seismicity. Possibly some are too weak to trigger earthquakes (e.g., day of year (doy) 210), others might be too close to preceding events that already reduced the available stresses and the medium needs more time to develop into a critical state again (e.g., doy 250).

We have shown that precipitation and groundwater-level increase show maximum cross-correlations with seismicity when delayed by 9-11 days. However, the time series are dominated by the two major peaks in March and August. The result is therefore only significant for these events. More sophisticated techniques have to be applied in further analysis to decipher the nonlinear coupling relations.

The increase of seismicity in March seems to be delayed by 6 days relative to the rain event on March 19th. This might have several reasons. (1) The mobile stations were for the first time installed in mid-April 2002, therefore the sensitivity of the network may have been reduced before that time. (2) In March, snow covered the elevated parts of the mountain, and the delay may also reflect differences in the catchment region compared to the August swarms. (3) The main source region for the March swarm is offset to the south and deeper than the average seismicity in the August swarm. This region might in the upper part not be as sensitive to pore pressure changes as Mt. Hochstaufen. The data set of 2002 does not allow to distinguish between the different possibilities, and future studies have to answer this question.

The maximum depth of the main seismic activity seems to be correlated with the base of the Northern Calcareous Alps. Present knowledge suggests that this overthrust fault lies at a depth of ~ 3 km [Angenheister *et al.*, 1972; Will, 1975], which corresponds well with the observed seismicity. Whether diffusion is hindered by an impermeable interface at this depth or if the medium is further from a critical state in the region beneath this boundary can so far only be speculation.

The maxima of the earthquake swarms on the other hand seem not to be correlated with any structural feature. The Figs. 3.7d-f, showing the

spatio-temporal evolution of seismicity, should give an indication if such a correlation would exist. At the present stage, location uncertainties may disguise small-scale structural features, but, as discussed below, our data set offers the opportunity to apply relative-relocation techniques which will hopefully sharpen our view in the future.

We have presented a hydrological interpretation of the observed hypocenters depth-migration and derived hydraulic diffusivity $D = 0.75 \pm 0.35 m^2/s$. Additional uncertainty may arise from the fact, that we did not try to separate fluid induced and background seismicity at this stage, which can be achieved on a statistical basis [*Hainzl and Ogata, 2005*]. However, our estimate corresponds well with results obtained by other researchers from analysis of seismicity patterns by pore pressure diffusion modeling [e.g., *Ventura and Vilaro, 1999; Parotidis et al., 2003; Saar and Manga, 2003; Rothert and Shapiro, 2003; Hainzl and Ogata, 2005; Parotidis et al., 2005*]. These results range between $0.1 m^2/s$ and $10.0 m^2/s$.

As already mentioned, our simplified hydrological model can only represent a first order approximation and the derived D has to be understood as an average over the studied volume. In the complex geological setting of the Staufen Massif D has to be calculated in the form of an anisotropic tensor [e.g., *Rothert and Shapiro, 2003*], and probably has a highly heterogeneous character. Furthermore, D might not be constant in time, because dynamic rupture can change porosity and increase permeability [e.g., *Miller et al., 2004*].

In order to improve the hydrologic model in these directions more precise earthquake location is essential. Our dataset includes many events characterized by very similar waveforms, which can be used to calculate highly accurate relative earthquake locations [e.g., *Fremount and Malone, 1987; Poupinet et al., 1984*] and to improve the velocity model [e.g., *Zhang and Thurber, 2003*]. Integrating data of a very dense seismometer network operating in Summer 2004, these techniques will allow to sharpen the pattern of seismicity.

As a final remark we want to report, that on July 15th, 2005, an intense rain event comparable to the August 2002 event triggered an earthquake swarm in the Staufen Massif. It was accompanied by a magnitude $ML = 2.7$

earthquake on July 18th, which was felt in Bad Reichenhall. Until the end of July more than 200 microearthquakes were recorded.

Acknowledgements

This study was to a major part supported by the Bavarian Ministry for Environment and by the Geological Survey of the Bavarian State. Toni Kraft was partially supported by the German Research Foundation (DFG) and the EU Community initiative INTERREG III B Alpine Space Programme SISMOVALP. Data was provided by the German Weather Service, SüdSalz GmbH in Bad Reichenhall and the Bavarian Bureau of Water Resources in Traunstein. We thank the Bavarian Forest Administration for permitting the installation of mobile stations and access to forest roads. Special thanks are expressed to the communities of Bad Reichenhall, Inzell, Piding, Teisendorf, and Siegsdorf, to the tourist club "Die Naturfreunde", as well as to Mr. Waigl and Mrs. Kerkmann for the permission to install seismological stations on their properties. Special thanks for support, accommodation and the good times goes to "Hansi" Pauli and to landlord and landlady of the Stoaneralm. We like to thank the following persons for giving logistic and technical support throughout the study and field campaign: Werner Bauer, Peter Danecek, Teresa Reinwald, Dr. Martin Beblo, Martin Feller, Dr. Erwin Geiß, Gunnar Jahnke and Christian Verard.

We thank Tomas Fischer, an anonymous reviewer and Sebastian Hainzl for their helpful comments, which improved the original version of the manuscript.

Chapter 4

High-Precision Relocation and Focal Mechanism of the 2002 Mt. Hochstaufen seismicity

The 2002 seismicity of Mt. Hochstaufen, SE-Germany, is characterized by several swarm-type earthquake sequences that follow above average rainfall events. First investigations have recently provided indication, that the rain events triggered this swarm-type activity. We present a detailed relocation of the 2002 seismicity, which is composed of (1) cluster analysis, (2) multi-event semi-automatic phase repicking, (3) probabilistic location in a pseudo-3D-velocity model with topography and (4) master event relocation. Furthermore, focal mechanisms of selected events are derived by taking into account the first-motion polarities of P, SV and SH-waves. We introduce a simple methodology to test the stability and estimate the variance of the focal mechanisms solutions. Location uncertainties of less than one hundred meters were achieved. The hypocenters are mainly concentrated between 1000m above and 4000m below sea level and aligned on two planes, which, however, can not be associated with geological structures with reasonable certainty. Swarm-type activity follows above average rain events and shows a depth migration of hypocenters over time. Evidence that the rain events triggered the earthquake swarms is reported by Hainzl et al. (2006) on basis of our relocation. The derived focal mechanisms seem to indicate an influence of the Saalachtal Fault Zone on the stress regime of the study area.

This chapter was published as: KRAFT, T., J. WASSERMANN AND H. IGEL (2006), *High-precision relocation and focal mechanism of the 2002 rain-triggered earthquake swarms at Mt. Hochstaufen, SE-Germany*, *Geophys. J. Int.*, doi:10.1111/j.1365-246X.2006.03171.x, in press.

4.1 Introduction

Observations of several decades indicate, that the seismicity of the Staufen Massif, SE-Germany, is influenced by meteorological parameters, i.e. the longtime record of annual variation of seismicity and precipitation are well correlated [*Schwarzmann et al.*, 2001]. A further characteristic of the area is the occurrence of earthquake swarms that seem to follow above average rainfall events. In 2002, a newly installed permanent seismological network recorded several complete swarm-type earthquake sequences, which followed above average rain events. Based on first results of their analysis of this data set, *Kraft et al.* [2006a] recently suggested reduction of frictional fault strength due to increase of pore pressure caused by diffusion of rain water to seismogenic depths as causative mechanism.

The spatial and temporal distribution of earthquakes can provide information on the tectonic regime and the material properties of an area. However, precise earthquake hypocenter locations are required to study the processes that trigger seismic activity. Location results of the 2002 Mt. Hochstaufen seismicity were until now based on manually determined absolute arrival times, a homogeneous half-space velocity model derived by joint hypocenter-velocity inversion and a location algorithm not taking into account the rough topography of the study area.

Improvement of the precision and reliability of earthquake locations can be achieved by adapting the velocity model to better represent the actual geological and topographic setting of the study area. Yet, the majority of available location algorithms uses layered velocity models and only account for lateral variations in velocity and topography by introducing static station corrections. These corrections represent an average of observed travel-time residuals for seismic waves arriving from spatially distributed sources. This means, that they can not correctly represent azimuthal variations of the seismic velocities. On the other hand, such algorithms are not able to take advantage of the three-dimensionality of the station distribution in rough topography, and to decide whether shallow hypocenters are located above or

below the mean station elevation. We overcome the afore mentioned drawbacks by using a pseudo-3D-velocity model with high-resolution topography and a probabilistic, non-linear earthquake location method, originally formulated by *Tarantola and Valette* [1982]. An additional major advantage of this method is that it provides complete description of the location uncertainty estimates.

We can further improve the location accuracy by applying cross-correlation techniques to identify groups of events with very similar waveforms and derive highly accurate relative phase-onset times. Very similar wave forms of different events recorded at one station indicate that the hypocenters and focal mechanisms are nearly identical [e.g., *Geller and Mueller*, 1980]. It is therefore possible to use the master-event technique to calculate relative earthquake locations for a group of similar events with respect to a master event with high accuracy. Absolute earthquake location can then be calculated from the solution of the probabilistic, non-linear earthquake location for the master event.

The fault-plane orientations and slip directions of earthquakes can provide important information about fault structure at depth and the stress field in which the earthquakes occur [e.g., *Gephart and Forsyth*, 1984]. Reliable fault-plane solutions can be obtained by observing the first-motion polarities of the P-wave, when many observations with good azimuthal coverage are available. In a less denser station network additional information can be gained by analyzing the first-motion polarity of SV and SH-component of the S-wave in three-component seismograms. However, the stability of the obtained focal mechanisms has to be carefully tested. We introduce an algorithm similar to that proposed by *Hardebeck and Shearer* [2002] for pure P-polarity datasets and test the stability of the focal mechanism solution by accounting for wrong polarity readings.

4.2 Study Area and Data

The Staufen Massif is situated at the northern margin of the Alps near the town Bad Reichenhall in SE Germany (Fig. 4.1). It belongs to the elongated fold-and-thrust belt of the Northern Calcareous Alps (NCA) and its geology is dominated by lower to middle Triassic limestone and dolomite with bedding planes dipping 60° to the south, approximately. The Staufen Massif builds a part of the thrust front of the NCA onto the Flysch Zone, a

sequence of shales rhythmically interbedded with sandstones. This east-west striking geological border at the northern foot of the mountain chain is also characterized by a prominent contrast of seismic velocities. In the south the Saalach Fault Zone (SFZ), a major sinistral strike-slip zone with an offset in the order of 12-15 km, primarily active in late-Oligocene and Miocene time [Frisch and Gawlick, 2003], separates the Staufeu Massif from the topographic low of the Reichenhall Basin with salinar sequences of remarkable thickness, which explain the increased mobility of the tectonic units in the region. A schematic tectonic map of the study area is shown in Figure 4.1.

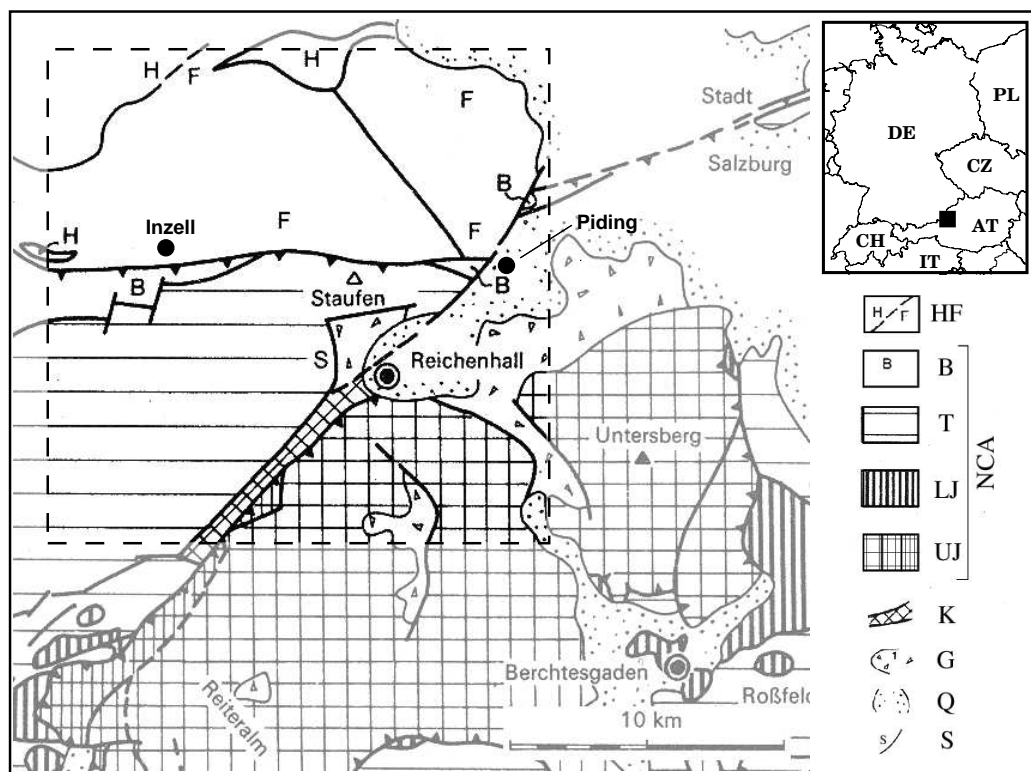


Figure 4.1: Tectonic map of the region around the study area [modified from Bögel and Schmidt, 1976]. The classical subdivision of the Northern Calcareous Alps (NCA) in four nappe units is indicated. The study area is marked by a dashed square. The insert map gives the geographical location of the tectonic map. **HF** Helvetic Unit and Flysch Zone; **B** Bavarian, **T** Tirolic, **UJ** Upper and **LJ** Lower Juvavic Units; **K** Kugelbach Zone; **S** Saalach Western Fault; **G** Gossau conglomerates; **Q** Quaternary sediments.

Further, geologic evidence for mass movements at the southern flank of Mt. Hochstaufer was recently summarized by Weede [2002]. Large east-west striking open fractures near the summit of Mt. Hochstaufer reach a length

of several hundred meters, openings of up to three meters and depths of at least hundred meters. Gravitational collapse and/or subsidence due to leaching of the Haselgebirge formation, an evaporitic breccia, are debated as causative processes.

Observations of several decades indicate, that the seismicity in this area is influenced by meteorological parameters, i.e. the longtime record of annual variation of seismicity and precipitation correlate well [*Schwarzmann et al.*, 2001]. A further characteristic of the area is the occurrence of earthquake swarms that seem to follow above average rainfall events. The seismicity is mainly concentrated on the Staufen Massif, whereas the surrounding is characterized by relative low seismic activity.

Starting in 2001 a permanent seismological network was installed in the area of Mt. Hochstaufen to study this phenomenon in detail. The network consists of six permanent and three mobile stations equipped with short-period three-component seismometers. Additionally, data of four pluviometers and several ground-water wells around the Staufen Massif are available (refer to *Kraft et al.* [2006a] for details). A location map of all stations is shown in Figure 4.2.

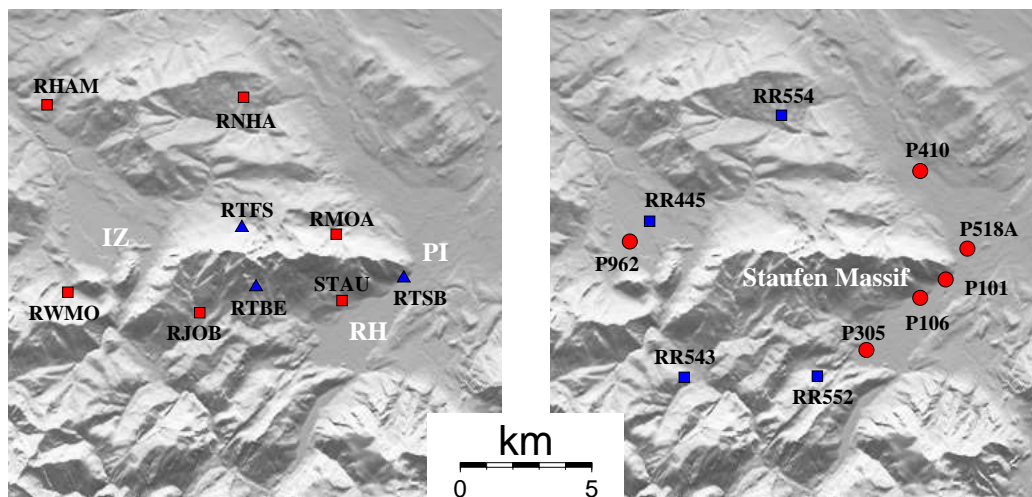


Figure 4.2: Seismo-meteorological network around Mt. Hochstaufen. Map borders: lon. $12^{\circ}40'$ - $12^{\circ}57'E$; lat. $47^{\circ}40.5'$ - $47^{\circ}55.5'N$. **Left:** Map of permanent (squares) and mobile (triangles) seismological stations recording in 2002. Cities of Inzell (IZ), Piding (PI) and Bad Reichenhall (RH) are indicated. **Right:** Hydrological (circles) and meteorological (squares) stations.

In March and August 2002, intense rainfall events led to severe flooding in Central Europe, causing an economic damage of 18.5 billion Euro [*Munich Re Group*, 2003]. Precipitation in the study area exceeded the monthly average within 48h, respectively 24h, during these events. As illustrated in Figure 4.3 the seismicity in the Staufen Massif increased significantly after both rain events. It rose roughly coincident with the onset of the intense rain. In both cases seismicity reached its maximum approximately ten days after the onsets and stayed on an elevated level for several weeks.

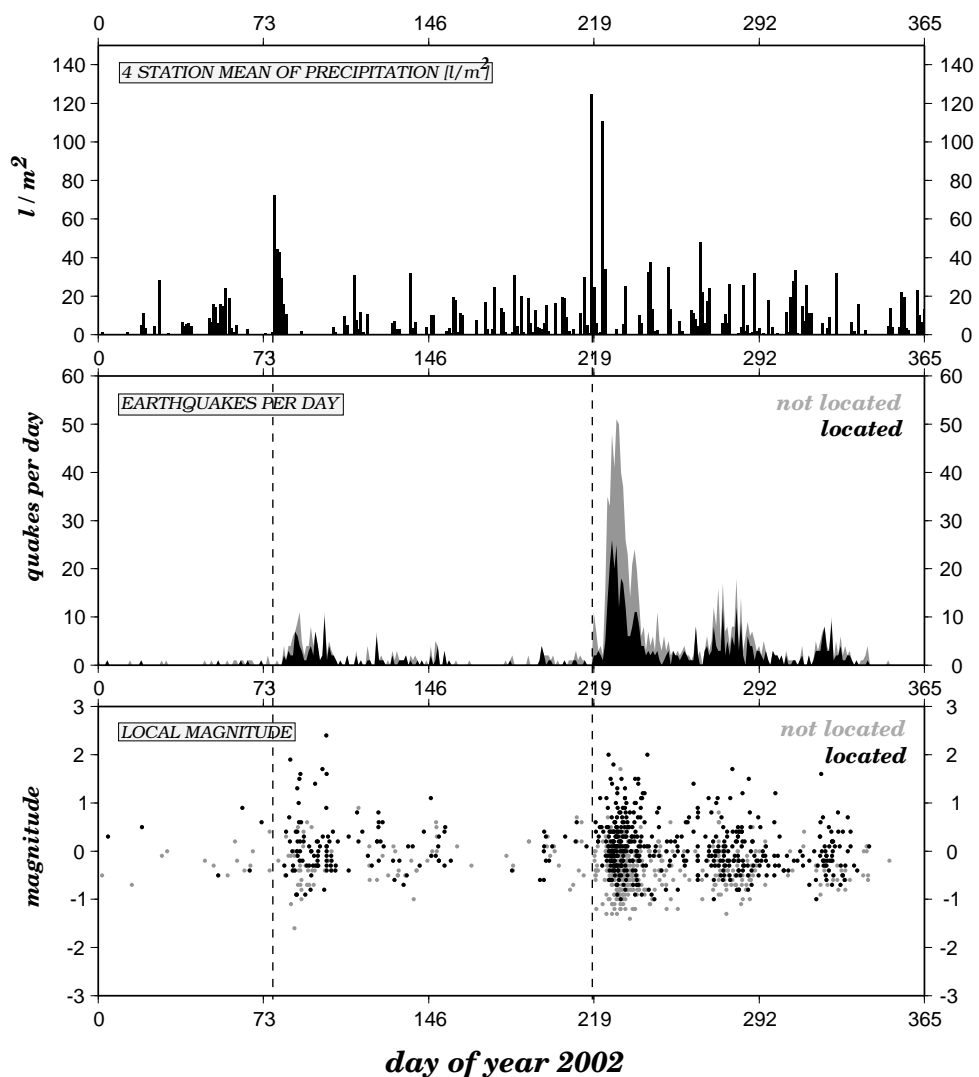


Figure 4.3: Spatio-temporal development of the seismicity in 2002. Vertical red lines mark the onsets of intense rain events in March and August. 612 located events (black), 559 not located events (gray).

In 2002, a total of 1171 earthquakes was recorded in the study area. The strongest event had a magnitude of $M_l=2.4$ on April 10. The magnitude-frequency statistic follows the Gutenberg-Richter law with a typical b-value of 1.1 ± 0.1 for magnitudes larger than $M_l=-0.2$. Below this value the distribution deviates from the Gutenberg-Richter law indicating incomplete data collection. The seismicity is very shallow and rarely exceeds 3km (b.s.l.). Swarm-type seismicity phases can be identified, which follow the intense rain events in March and August. The August swarm can further be divided in at least three subswarms [*Kraft et al.*, 2006a].

The seismological data set consists of several families of earthquakes characterized by very similar wave forms. This indicates that these events have nearly identical hypocenter locations and focal mechanisms. Several techniques exist, which take advantage of wave-form similarity to compute highly accurate relative earthquake locations [e.g., *Aster and Rowe*, 2000, and references therein]. We use a combination of those techniques to identify clusters of similar events and to reduce location uncertainty in the data set.

4.3 Cluster Analysis

Small earthquakes that are characterized by very similar waveforms recorded at the same station should only be separated by distances less than a quarter of their dominant wavelength [e.g., *Geller and Mueller*, 1980]. Hence, in order to identify groups of closely spaced earthquakes in the data set, wave-form similarity served as a measure of hypocenter proximity in a hierarchical cluster analysis, which will be outlined in the following.

For every earthquake time windows of length 7 s starting 1 s before the P-onset were extracted from the vertical component records of station STAU, which was the station that recorded the most events of the 2002 data set [*Kraft et al.*, 2006a]. Further, we applied a bandpass filter (3 - 20 Hz) and cross-correlation to quantify the similarity of different seismograms using the GIANT analysis system [*Rietbrock and Scherbaum*, 1998]. The resultant set of maximum cross-correlation coefficients c_{ij} for every possible combination of events $i, j \in [1, N]$ ($N = 1171 =$ number of events) were arranged to form a square symmetric similarity matrix \mathcal{C} . A visualization of the similarity matrix \mathcal{C} is shown in Figure 4.4a.

The shape of \mathcal{C} can be interpreted as follows: (1) Squares representing sets of highly similar events are aligned on the diagonal, indicating that sim-

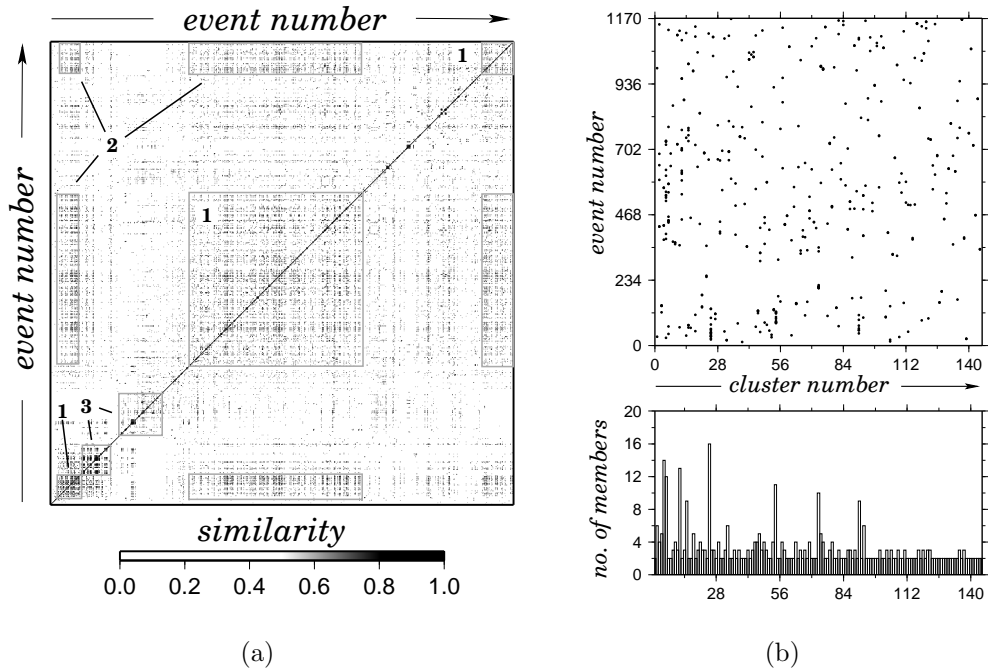


Figure 4.4: **a)** Similarity matrix \mathcal{C} for events in 2002 obtained from cross-correlation of STAU vertical seismograms. Gray scale indicates maximum cross-correlation coefficient. Event numbering is in temporal order. Highlighted areas and numbering corresponds to the discussion in the text. **b)** Clusters obtained from similarity matrix \mathcal{C} by pairwise single linkage clustering with threshold $c_{ij} \geq 0.8$. Cluster numbering follows decreasing similarity. Top: Members of the 145 clusters. Bottom: Number of members per cluster.

ilar events are as well clustered in time. (2) Off-diagonal rectangular areas partly link the main-diagonal squares, suggesting reactivation of seismogenic regions over time. (3) Some main-diagonal squares spanning a range of low event numbers seem only be weakly linked to other elements, indicating a concentration of seismicity to a different source region in the corresponding time period. This interpretation is supported by the results of *Kraft et al.* [2006a], which found that the March swarm was located further south and deeper than most of the remaining seismicity in 2002.

The similarity matrix \mathcal{C} built the basis of a hierarchical cluster analysis, where in an iterative process similar entities (events or groups of events represented by the relevant rows and columns of \mathcal{C}) were repeatedly joined to form a hierarchical tree, beginning by merging the most similar waveforms. The similarities between the newly formed group and all other entities were calculated using the pairwise single linkage technique [e.g., *de Hoon et al.*, 2004], where the similarity between two entities was defined as the highest

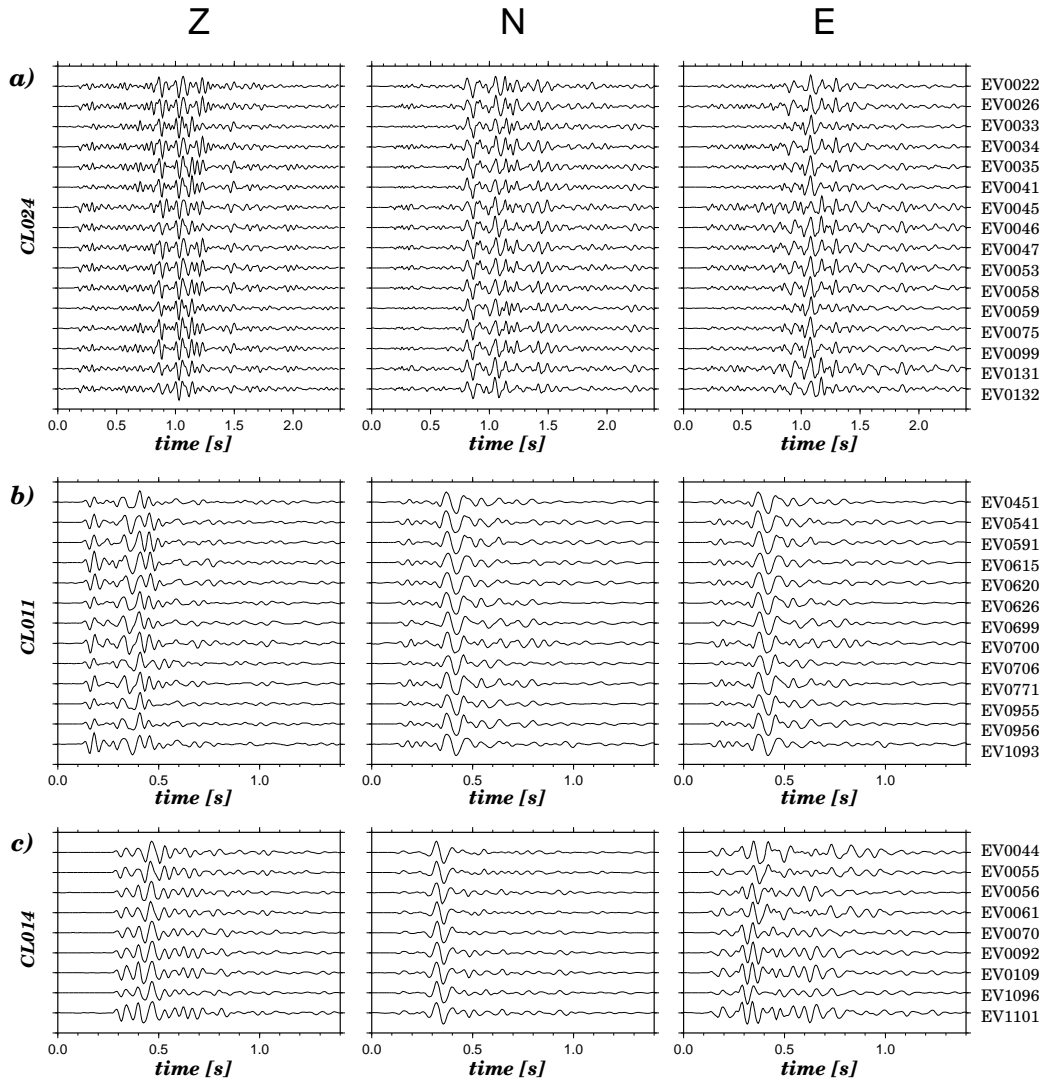


Figure 4.5: Example seismograms of station STAU from three clusters found in 2002. The clusters are representative of the March (CL024) and the August swarm (CL011 and CL014). The waveforms were bandpass filtered (3-20 Hz), scaled to maximum trace amplitude and aligned for maximum cross-correlation. Magnitudes can range from $M_l = -0.8$ to $M_l = 1.6$ (CL014). For each cluster the three orthogonal components of ground velocity are shown (vertical: Z, horizontal: N = North, E = East). Please note the different window lengths in a), b) and c) given in seconds.

similarity among the pairwise similarities between their members. The joining process was repeated until a user-defined lower similarity threshold of $c_{ij} \geq 0.8$ was reached.

In total 145 clusters were identified, with a minimum of two and up to 16 members. Figure 4.4b+c illustrate how many and which events were joined to

form clusters. Seismogram examples of representative clusters of the March swarm (CL024) and the August swarm (CL011 and CL014) are shown in Figure 4.5. Even though, only the vertical component (Z) was considered in the cluster analysis, cluster members are characterized by having very similar wave forms also in the horizontal components. Although, the magnitudes can range from $M_l=-0.8$ to $M_l=1.6$ inside the clusters (e.g., CL014), the similarity is preserved over the complete length of the seismograms. This indicates that for the observed magnitude range, the waveforms are nearly independent of the source-time function and are predominantly influenced by the Green function of the medium and the focal mechanisms. However, because of the high waveform similarity the latter two seem to be nearly identical within a cluster. This motivates and justifies the methodology described in the following.

4.4 Multi-Event Semi-Automatic Phase Repicking

Comparing similar waveforms can provide highly accurate relative phase arrival times. Thereby, the time difference between the arrivals of the same phase at one station for different earthquakes is derived by cross-correlation in the time or in the frequency domain [e.g., *Poupinet et al.*, 1984; *Deichmann and Garcia-Fernandez*, 1992]. However, these relative arrival times have to be related to some master phase onset determined from single event picking when absolute arrival times are desired. Yet, the accuracy of onset times determination can be significantly improved when comparing a number of similar phase-aligned seismograms simultaneously [*Rowe et al.*, 2002].

We performed a multi-event semi-automatic phase repicking within the clusters identified beforehand. Seismograms of all cluster members were component-wise aligned with respect to the event with the largest magnitude (master event) using the analysis software Seismic Handler [*Stammler*, 1993]. All seismograms were then phase-wise cross-correlated with the master event and realigned for the time lag corresponding to the maximum cross-correlation coefficient cc_{ij} . The window lengths for this correlations was chosen interactively, assuring the alignment of even noisy seismograms. If necessary, the master phase onset time was corrected manually. The slave phase-onset times were calculated by adding the cross-correlation derived time differences to the time of the master phase-onset. Phase weights were

derived by incrementing the picking weight obtained for the master-event phase according to the value of cc_{ij} as listed in Table 4.1.

W_{pick}	$\Delta t[s]$	δW_{pick}	c_{ij}	NonLinLoc
0	≤ 0.01			
1	≤ 0.05	+0	≥ 0.8	$\delta v = 0.2$ km/s
2	≤ 0.10	+1	≥ 0.5	$\Rightarrow \delta T = 0.05$ s
3	≤ 0.30	+2	≥ 0.3	[Moser <i>et al.</i> , 1992]
4	≤ 0.60	+3	else	
5	≤ 2.00			$\Delta = 0.5$ km
6	else			

Table 4.1: Uncertainty/phase-weighting scheme for picking, cross-correlation and NonLinLoc Gaussian error estimation. Picking weights (W_{pick}) assigned according to picking uncertainty Δt . Cross-correlation phase weights were derived by incrementing (δW_{pick}) the picking weight of the master phase according to the cross-correlation value c_{ij} . The values δT and Δ represent the travel time error due to velocity model uncertainty [Moser *et al.*, 1992] and a correlation length corresponding to wavelength of real velocity variations [Tarantola and Valette, 1982]. Both values are used by NonLinLoc to calculate the covariance matrix of the calculated traveltimes [Lomax *et al.*, 2000].

We checked the derived onset times by calculating arrival-time differences of P-phases and S-phases (dt_p and dt_s) with respect to station STAU for every event and available station. Within one cluster these arrival-time differences for one station should be nearly identical. Further, the ratio dt_s/dt_p should correspond to the ratio of the seismic velocities (v_p/v_s). Events that violated these criteria were excluded from further analysis. After this selection 51 clusters with $\max\{dt_p, dt_s\} \leq 0.03$ s remained. Figure 4.6 shows a normalized cumulative histogram of the 314 standard deviations $\sigma^{cl}(dt_p, dt_s)$ derived from the sets of dt_p and dt_s . The 95%-level is indicated by a dash-dotted line and demonstrates that $\sigma^{cl}(dt_p, dt_s) \leq 0.012$ s holds for over 95% of the data. This indicates a very good agreement of the phase-arrival times of different events of one cluster at the individual stations.

Encouraged by this fact, we calculated synthetic phase-arrival times for missing stations of individual cluster members. This was done by adding $dt_{p,s}$, derived for the master event, to the phase arrival time at station STAU of the corresponding event. Weights for these synthetic phases were calculated

by increasing the master phase weight by two (comp. Table 4.1). In this way we assured that the location uncertainties derived for events with synthetic arrival times were adequately high. Using this procedure, the number of locatable earthquakes was increased from 546 to 612.

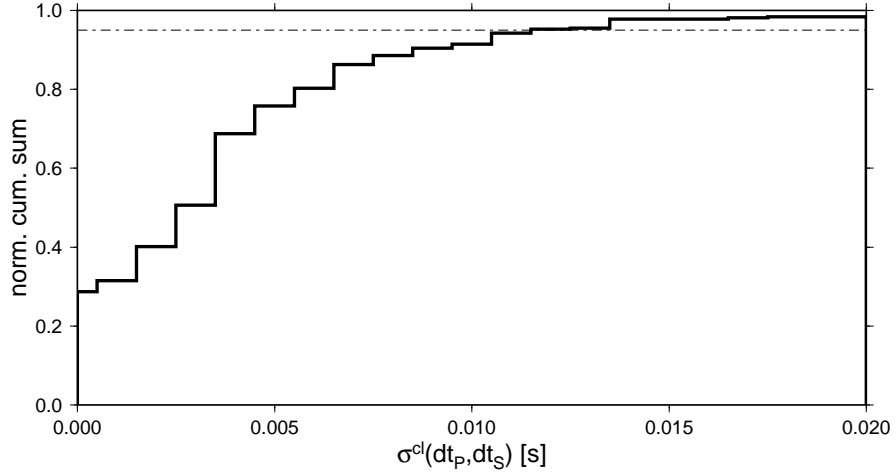


Figure 4.6: Normalized cumulative histogram of standard deviations $\sigma^{cl}(dt_p, dt_s)$ of the 314 analyzed sets of dt_p and dt_s from 51 clusters. As indicated by the dashed line, $\sigma^{cl}(dt_p, dt_s) \leq 0.012$ s holds for more than 95% of data.

4.5 Earthquake Relocation

4.5.1 Probabilistic Earthquake Location

Based on the data set described above, we calculated probabilistic locations for Mt. Hochstaufen earthquakes using the software package NonLinLoc [Lomax et al., 2000]. As the study area is characterized by a strong north-south velocity contrast and a rough topography, we composed the velocity model of two homogeneous quarter-spaces with realistic topography. Compressional seismic wave velocities (v_P) were taken from seismic refraction studies in the Eastern Alps [Will, 1975; Bleibinhaus and Gebrande, 2006]. A typical velocity for the Flysch Zone ($v_P = 3.6$ km/s) was assigned to the northern part of the model, whereas $v_P = 5.8$ km/s, typical for the NCA, was used in the southern part. Above the topography, which was taken from a 50×50 m digital elevation model provided by the Geodetic Survey of the Bavarian State [LVG-Bayern, 2000], the velocity was set to $v_P = 10^{-6}$ km/s. This was necessary, because a slowness model had to be specified for input in NonLinLoc. For conversion from compressional to shear wave velocity model the

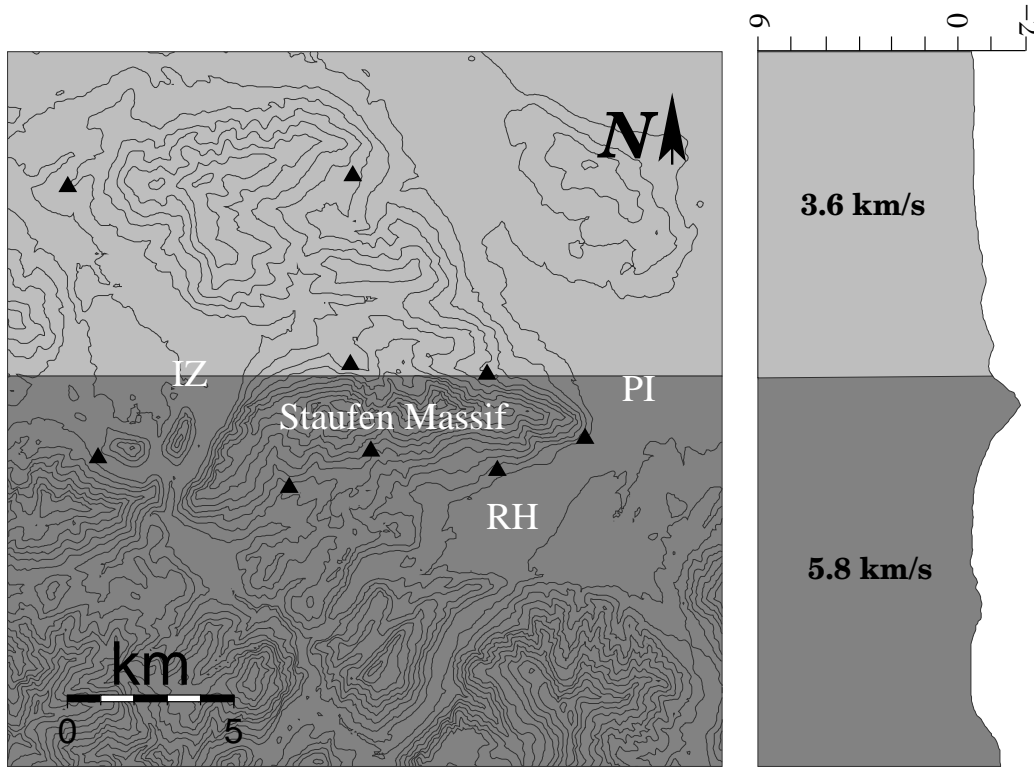


Figure 4.7: Pseudo-3D-velocity model with topography used for probabilistic nonlinear earthquake location. Velocities for the P-wave are given in the cross section. Seismological stations are indicated by triangles.

ratio $v_p/v_s = 1.81$, derived in a previous study [*Kraft et al.*, 2006a], was used. The velocity model was discretized with a grid spacing of 100 m. The model dimensions and the geographical setting are given in Figure 4.7.

The location algorithms implemented in NonLinLoc follows the probabilistic formulation of inversion and the equivalent methodology for earthquake location [e.g., *Tarantola and Valette*, 1982; *Moser et al.*, 1992; *Wittlinger et al.*, 1993; *Lomax et al.*, 2000]. *Tarantola and Valette* [1982] showed, that the complete probabilistic solution to the inverse problem can be expressed as a posteriori probability density function (PDF) in an easy way, if the calculated and the observed arrival times are assumed to have Gaussian uncertainties expressed by covariance matrices [C_T and C_d in *Tarantola*, 2004, p. 35], and if the a priori information on the origin times is taken as uniform. This assumption allows a direct, analytical evaluation of the PDF for the spatial location and the origin time as well as comprehensive uncertainty and resolution information. A complete description of the underlying

theory can be found in *Tarantola* [2004].

For every station of the 2002 Mt. Hochstaufen network theoretical travel times to all grid points of the velocity model were calculated using a Huygens-principle finite-difference algorithm [*Podvin and Lecomte*, 1991]. We used the nested grid search algorithms, implemented in NonLinLoc, to obtain the PDF, which represents the complete probabilistic spatial solution to the earthquake location problem. The PDF indicates the uncertainty in the spatial location due to Gaussian picking and traveltimes calculation errors as well as the network–event geometry. The maximum-likelihood point of the complete, non-linear location PDF was selected as the hypocenter solution and Gaussian error estimates were calculated by Singular Value Decomposition (SVD) of the combined covariance matrixes [$C_D = C_T + C_d$, *Tarantola*, 2004,p. 35].

In Figure 4.8 four examples for a posteriori probability density functions are given. The PDFs are scaled to have unit probability when integrated over the final search grid (horizontal: 5×5 km; vertical: 7 km). A typical event of the March swarm (Figure 4.8a) and the master event of cluster CL024 as a typical event of the August swarm (Figure 4.8b) represent examples of good location results. All but one Stations (RTBE) contribute to the solution. The PDF are of elliptical shape and have a strong maximum resulting in small confidence volumes. The largest event of 2002 on April 10 reaching a magnitude of $M_l=2.4$ is unfortunately an example for a badly confined event (Figure 4.8c). Resulting from the lack of mobile stations and down-weighted arrival-time picks of remote stations especially the depth has a large uncertainty.

For some events that only had few arrival-time readings of low quality a second maximum of the PDF can develop above the surface as shown in Figure 4.8d. This is due to the fact, that the volume above the topography can absorb uncertainties in the input data because of its very low velocity. The super-topographic maximum sometimes dominated the PDF and leads to wrong location results. Therefore, events of this kind were excluded from further analysis.

Figure 4.9 illustrates the quality of the location result in form of normalized histograms of the root mean square residual of calculated to observed arrivaltimes (RMS) and estimated Gaussian confidence intervals of hypocenter location (erh and ehz, representing lateral and vertical uncertainty) . For 90% of the 612 located events location uncertainties are smaller than

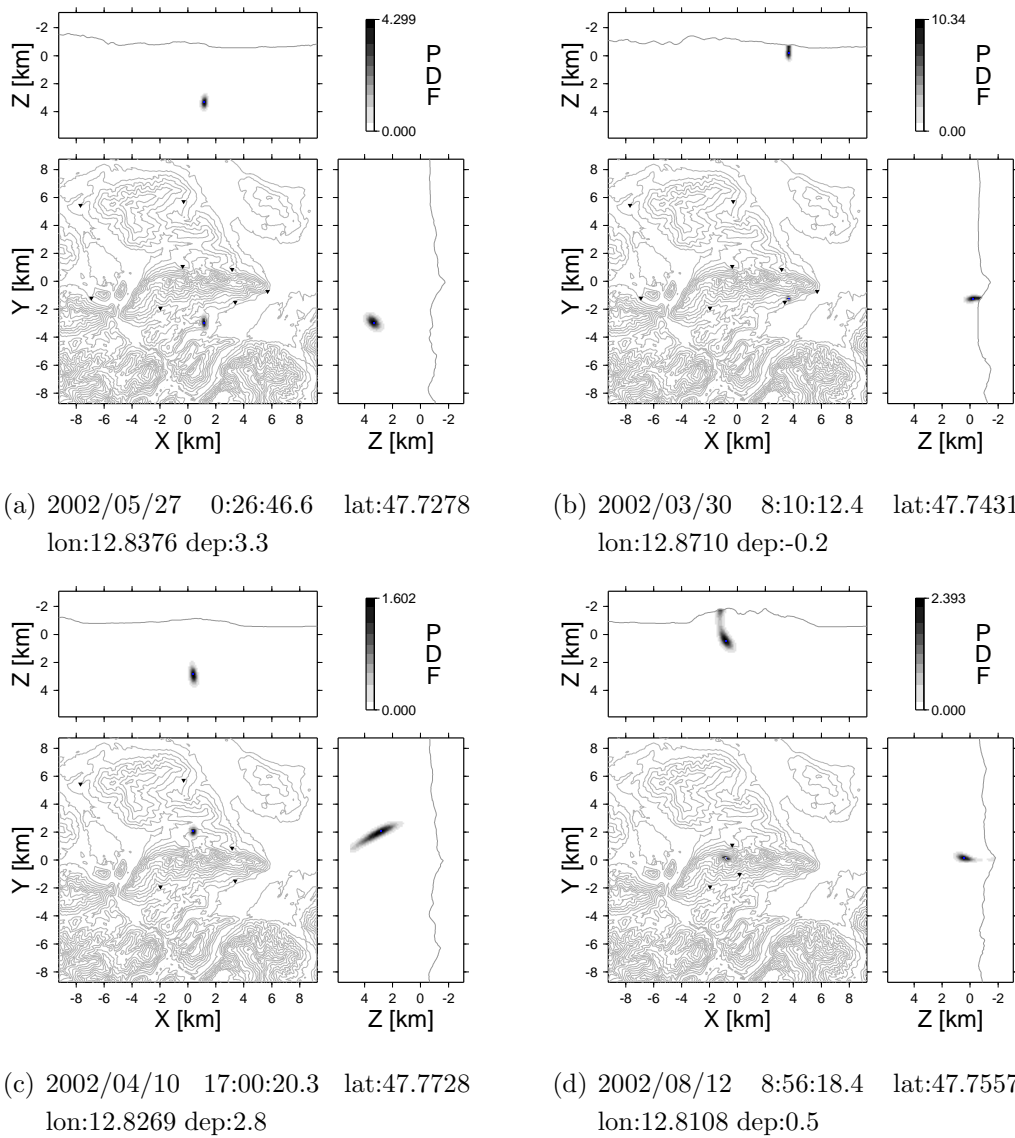


Figure 4.8: Probabilistic location result for a) a representative event of the March swarm, b) the master event of cluster CL024 having the most members, c) the largest event $M_l=2.4$. d) Due to the non-zero velocity above topography, PDFs of badly constrained events tend to have a second maximum above the surface. These kind of events were excluded if the super-surface maximum was the maximum-likelihood point of the PDF.

0.7 km and the RMS less than 0.12 s. For 75% of the data are $eh_z < 0.4$ km, $er_h \leq 0.6$ km and $RMS < 0.1$ s. This indicates that for the great majority of events the absolute location are already of good quality. In the following we will take advantage of the results of the cluster analysis and calculate relative location of all cluster members with respect to their master events.

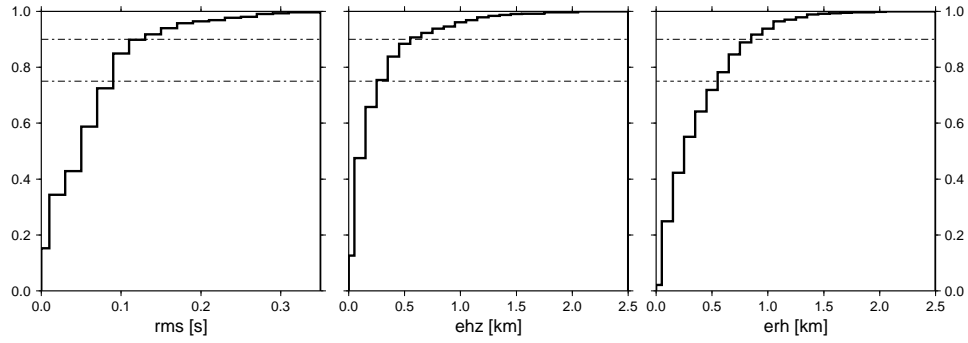


Figure 4.9: Error analysis of the probabilistic earthquake location. Normalized cumulative histograms of 67% confidence intervals of hypocenter depth (ehz), horizontal coordinates (erh) and root mean square arrival-time residual (RMS) are shown. As indicated by the dash-dotted lines, for 90% of the located events $\text{RMS} < 0.12$ s, $\text{ehz} \leq 0.6$ km and $\text{erh} < 0.7$ km.

4.5.2 Master Event Location Technique

The master-event location technique, as all multiple-event location procedures, assumes that if the hypocentral separation between a set of earthquakes is small compared to the event-station distance and the scale length of heterogeneity, then the ray paths between a source region and a station are similar and the error introduced by incorrect assumptions regarding velocity structure has a nearly constant value for times measured at the same station [e.g., *Wolfe*, 2002].

The cluster analysis described above has identified 143 clusters of at least two similar events. Within these clusters we expect the conditions for master-event locations to be fulfilled when excluding stations that are too close to the hypocenters. This can easily be achieved by choosing a lower threshold for the arrival-time difference of P- and S-phase (dt_{sp}) at a station. To assure a minimum event-station distance of 2 km this threshold was set to $dt_{asp} = 2 \text{ km} * (v_p/v_s - 1)/v_P \geq 0.28$ s, using $v_P=5.8$ km/s and $v_P/v_S=1.81$.

The governing equation for master-event location can be derived from the geometrical setting shown in Figure 4.10. The relationship between the arrival-time differences of a phase (P or S) from master event (M) and the same phase from the slave event (S_j) at station i can be expressed as:

$${}^i dt_{p,s}^{S_j} = \Delta T^{S_j} - \frac{\mathbf{L}^{S_j} \cdot {}^i \mathbf{n}^{S_j}}{v_{p,s}} \quad (4.1)$$

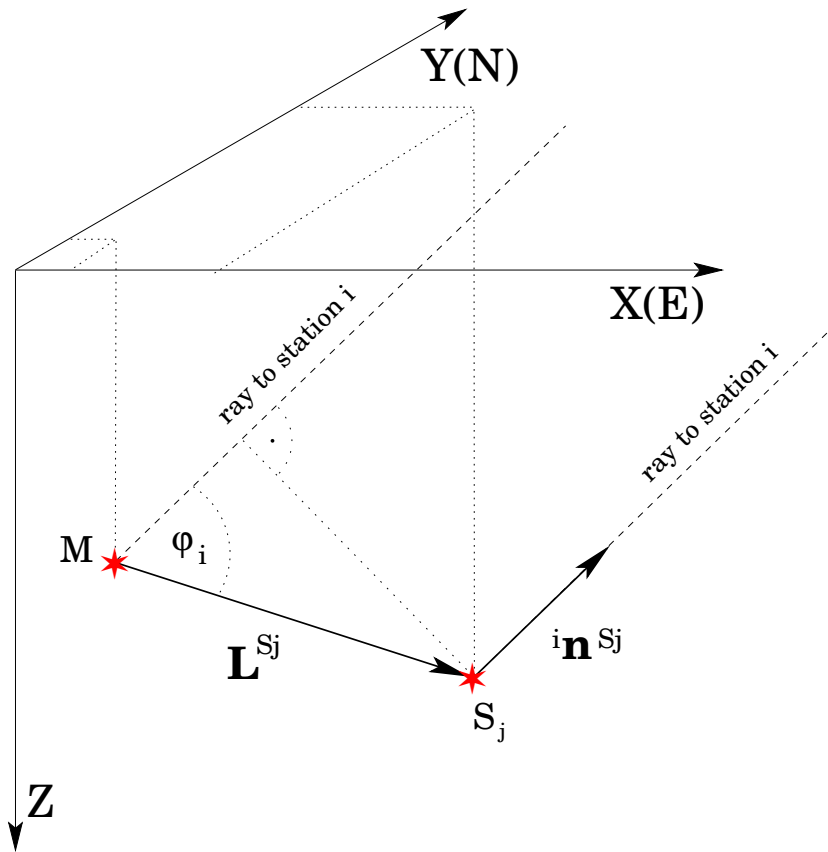


Figure 4.10: Geometrical layout for master-event technique. **M**: master event; **S**: slave event; $\mathbf{L} = (x, y, z)^T$: relative location vector; ${}^i \mathbf{n}$: unit vector pointing to station **i**.

Where ΔT^{S_j} is the difference in origin time between master and slave event, \mathbf{L}^{S_j} and ${}^i \mathbf{n}^{\text{S}_j}$ are the vectors defined in Figure 4.10, and $j \in [1, k_c]$ and $i \in [1, l_c]$ with k_c and l_c the cluster-specific numbers of slave events and observing stations.

For every master-slave event pair of a cluster $2l_c$ equations for ${}^i dt_{p,s}^{\text{S}_j}$, weighted by the cross-correlation coefficient cc_{MS_j} (comp. Section 4.4) obtained for the corresponding events and phases [e.g., *Waldhauser and Ellsworth, 2000*], were combined in linear systems of the form:

$$\mathbf{d}^{\text{S}_j} = \mathcal{G}^{\text{S}_j} \cdot \mathbf{m}^{\text{S}_j} \quad (4.2)$$

Taking a closer look at one master-slave pair, the data vector \mathbf{d}^{S_j} , model vector \mathbf{m}^{S_j} and matrix \mathcal{G}^{S_j} , when dropping the super-script S_j and sub-script c for brevity, expand to:

$$\begin{pmatrix} {}^1 dt_p \\ {}^1 dt_s \\ \vdots \\ {}^l dt_p \\ {}^l dt_s \end{pmatrix} = \begin{pmatrix} 1 & -\frac{{}^1 n_x}{v_p} & -\frac{{}^1 n_y}{v_p} & -\frac{{}^1 n_z}{v_p} \\ 1 & -\frac{{}^2 n_x}{v_s} & -\frac{{}^2 n_y}{v_s} & -\frac{{}^2 n_z}{v_s} \\ \vdots & \vdots & \vdots & \vdots \\ 1 & -\frac{{}^l n_x}{v_p} & -\frac{{}^l n_y}{v_p} & -\frac{{}^l n_z}{v_p} \\ 1 & -\frac{{}^l n_x}{v_s} & -\frac{{}^l n_y}{v_s} & -\frac{{}^l n_z}{v_s} \end{pmatrix} \cdot \begin{pmatrix} \Delta T \\ x \\ y \\ z \end{pmatrix}$$

Within one cluster the linear systems for the k_c master-slave event pairs can be combined to one system of the form:

$$\begin{pmatrix} \mathbf{d}^{S_1} \\ \mathbf{d}^{S_2} \\ \vdots \\ \mathbf{d}^{S_{k_c}} \end{pmatrix} = \begin{pmatrix} \mathcal{G}^{S_1} & \mathcal{O} & \dots & \mathcal{O} \\ \mathcal{O} & \mathcal{G}^{S_2} & \dots & \mathcal{O} \\ \vdots & \vdots & \ddots & \vdots \\ \mathcal{O} & \mathcal{O} & \dots & \mathcal{G}^{S_{k_c}} \end{pmatrix} \cdot \begin{pmatrix} \mathbf{m}^{S_1} \\ \mathbf{m}^{S_2} \\ \vdots \\ \mathbf{m}^{S_{k_c}} \end{pmatrix}$$

which will briefly be referred to as

$$\mathbf{d}^{\text{MS}} = \mathcal{G}^{\text{MS}} \cdot \mathbf{m}^{\text{MS}} \quad (4.3)$$

Using *Matlab*[®] [2005], these linear systems were solved by calculating the generalized inverse [Moore, 1920; Penrose, 1955] $(\mathcal{G}^{\text{MS}})^+$ of \mathcal{G}^{MS} and assessing the optimal estimate of \mathbf{m}^{MS} in a least square sense by computing

$$\mathbf{m}_{\text{est}}^{\text{MS}} = (\mathcal{G}^{\text{MS}})^+ \cdot \mathbf{d}^{\text{MS}} \quad (4.4)$$

Under the assumption that the data are uncorrelated and have equal variance σ_d^2 , error estimates for the relocated slave events can be derived by plugging $\mathbf{m}_{\text{est}}^{\text{MS}}$ into Equation 4.3 to obtain an estimate of the data vector $\mathbf{d}_{\text{est}}^{\text{MS}}$, and calculating the sample variance s as an estimate of the true data variance σ_d^2 [e.g., Menke, 1989]:

$$s = \frac{1}{2l_c - 4} (\mathbf{d}_{\text{est}}^{\text{MS}} - \mathbf{d}^{\text{MS}})^2 \quad (4.5)$$

An estimate for the model co-variance matrix $\mathcal{S}_{m_{\text{est}}}^2$ can than be obtained from:

$$\mathcal{S}_{m_{\text{est}}}^2 = \sigma_{d_{\text{est}}}^2 \cdot ((\mathcal{G}^{\text{MS}})^T \cdot \mathcal{G}^{\text{MS}})^{-1} \quad (4.6)$$

Master-event relocations for representative clusters are shown in Figure 4.11. Unfortunately the estimated errors are of comparable size as the distances between master and slave events. This prohibits a detailed interpretation of the geometrical distribution of the events within a cluster.

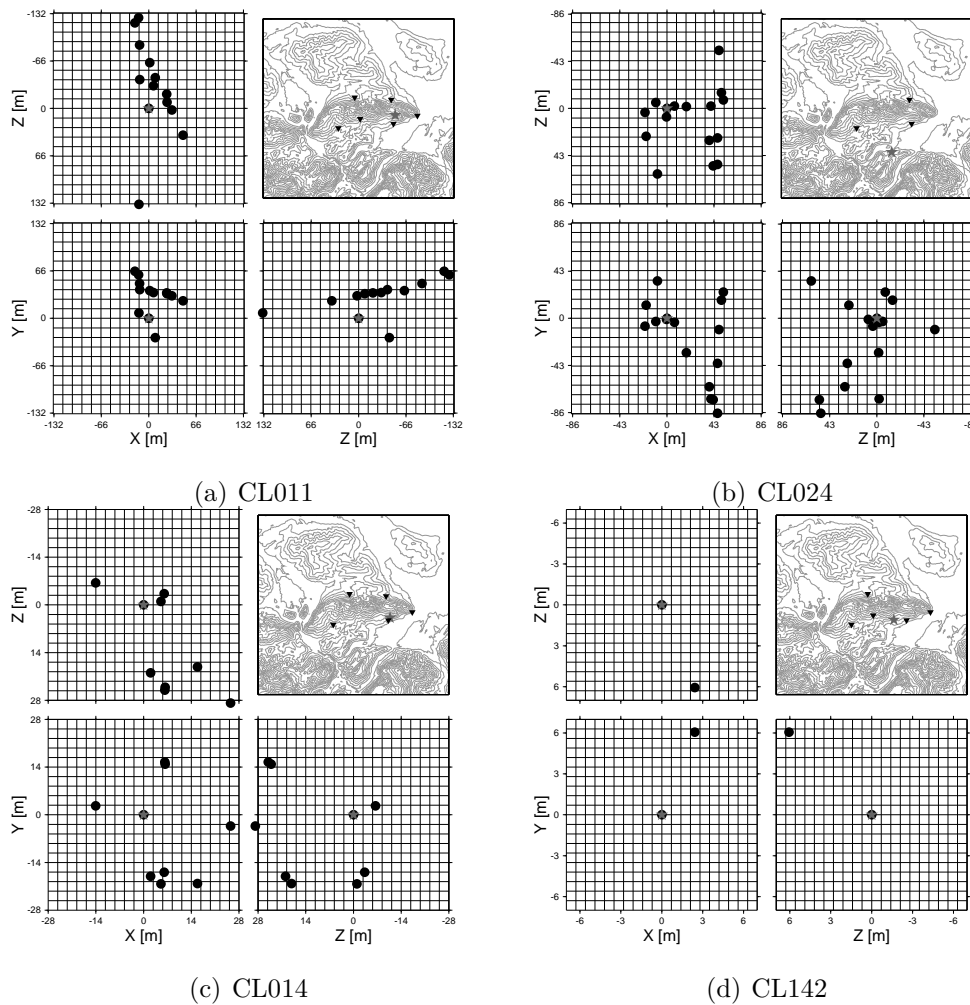


Figure 4.11: Relocation results for four clusters. Map-view and two vertical profiles centered on the master event (star) are shown. The absolute location of the master event and the available stations are indicated in a map of the study area in the top-right of the subfigures. Units are in meters from the master event. X: East-West, Y: North-South, Z: Down-Up (left handed system). a) CL011 b) CL024 most members (16) c) CL014 d) CL142 two-event cluster very small event distance.

However, the size of the event clouds seems to be a good estimate of the volume occupied by the cluster. For events with relocation uncertainty smaller than 200 m absolute locations were derived by adding the relative location and the NonLinLoc-location. For larger uncertainties of the master-event location we regard the NonLinLoc-location as more reliable. However, the master-event relocation significantly reduced the spread of the earthquake clouds compared to the probabilistic result down to a size of a few meters.

4.5.3 Result of the Relocation

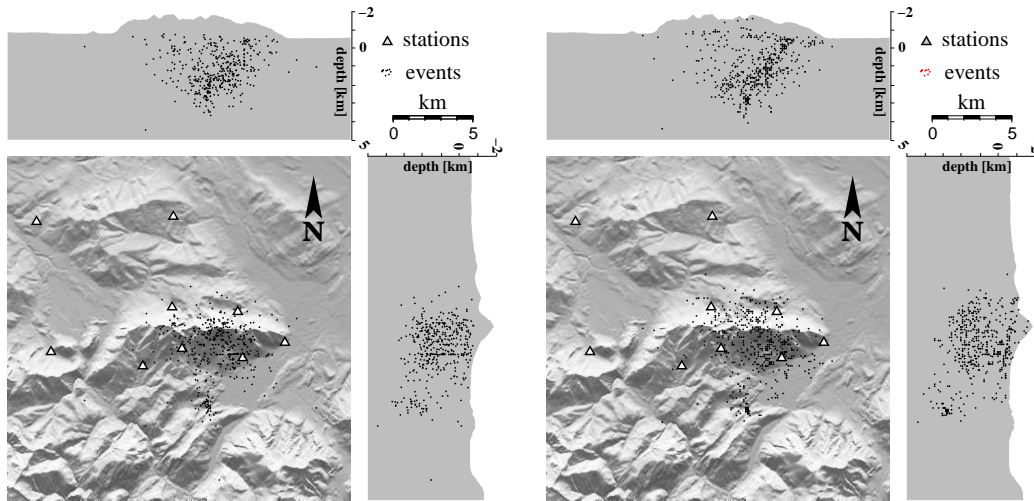
Hypocenters obtained using the master-event location technique were combined with the results of the probabilistic inversion to form the solution data set. If the location uncertainty of a relative location was less than 200 m the corresponding absolute location was included in the solution data set, otherwise the result of the probabilistic inversion were used. Compared to previous hypocenter locations, where the seismicity was diffusely distributed below the Staufen Massif [Fig. 4.12a, comp. *Kraft et al.*, 2006a], spatial and temporal patterns can now clearly be identified in the seismicity (Fig. 4.12b+c).

Using a pseudo-3D-velocity model with topography allowed to identify events above the average station elevation by taking advantage of the three-dimensionality of the station distribution. Hence, the depths of the located hypocenters span a range between -1.7 km and 4.2 km (b.s.l.) with the majority of the events deeper than -1.0 km. This means that earthquakes in the Staufen Massive can occur more than 1000m above the Reichenhall Basin.

In March 2002, the swarm-type seismicity concentrates in a very small source volume in 3 km depth south of Mt. Hochstaufen (Fig. 4.12b+c). The relocation tightened the hypocenter cloud significantly and in particular reduced its depth extension. The source volume of the March swarm coincides with the surface trace of the Kugelbach Zone, a part of the sinistral Saalachtal Fault Zone (Fig. 4.1).

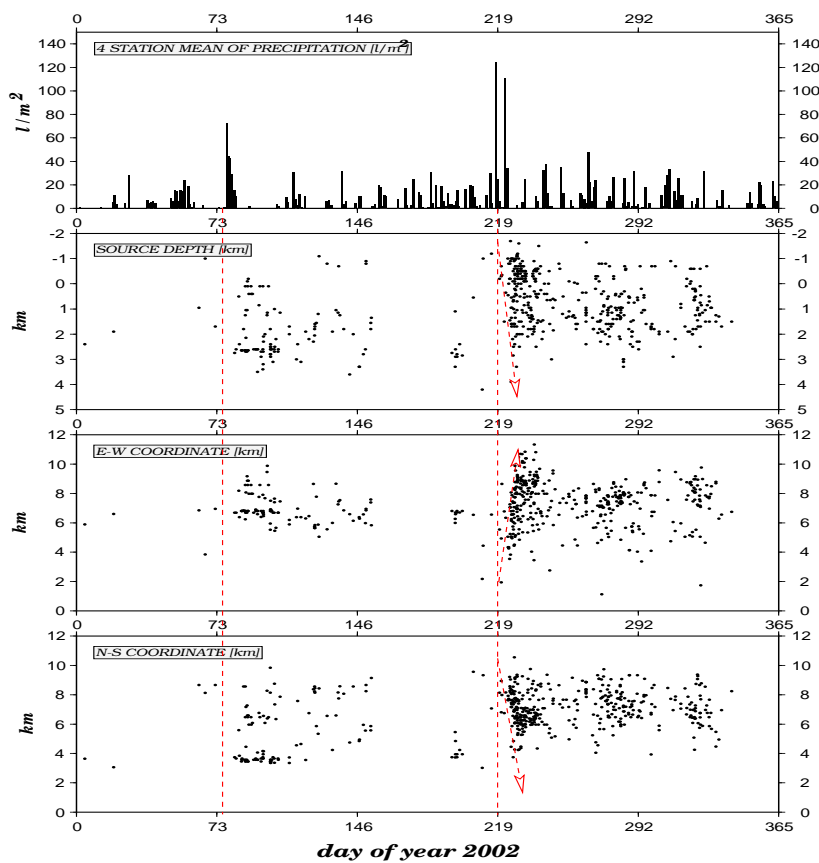
Later in the year, mainly during the swarm sequences starting in August, the seismicity is distributed over a larger source volume inside the Staufen Massif. However, the hypocenters seem to align along two planes. One is striking north-south and dipping approximately 50° west, connecting the easternmost summit of the Staufen Massif, and the source volume of the

Figure 4.12: Hypocenter map of 2002 Mt. Hochstaufen seismicity before (a) and after (b) relocation. EW- and NS-profiles through the summit of Mt. Hochstaufen are shown on top and to the left of the epicenter maps. The spatio-temporal development of the seismicity is shown in c). Dashed lines indicate the onset of the intense rain in March and August. Dashed arrows indicate the migration of the hypocenters.



(a) Standard locations

(b) Relocated seismicity



(c) Spatio-temporal development

March swarm (comp. east-west cross-section in Figure 4.12b). Yet, the strike and dip do not correspond to geological features observed in the study area and no explanation for the alignment along this plane can be given at present. The second plane seems to strike east-west with a southern dip of approximately 10° , very shallow beneath the mountain chain. Although, the thrust fault and the bedding plane orientations in the Staufen Massif follow this trend in general, the observed dip of the seismicity is too shallow to be associated with these geological features with reasonable certainty.

The spatio-temporal development of the seismicity (Fig. 4.12c) is essentially the same as before the relocation and was described in detail by *Kraft et al.* [2006a]. A major feature that can be observed is the concentration of earthquakes in several swarm-type sequences, which follow above average rain events. Furthermore, the August earthquake swarm is characterized by a depth migration of hypocenters over time. On the basis of these observations, *Kraft et al.* [2006a] proposed that rainfall triggered the earthquakes via the mechanism of pore pressure diffusion. Evidence for this hypothesis was recently reported by *Hainzl et al.* [2006], successfully predicting the seismic event rate from the calculated pore-pressure change at depth due to rainfall.

4.6 Focal Mechanism Determination

The fault-plane orientations and slip directions of earthquakes can provide important information about fault structure at depth and the stress field in which the earthquakes occur [e.g., *Gephart and Forsyth*, 1984]. The source of a small earthquake is typically approximated by a double-couple point source derived from observed body-wave first-motion polarities. The nodal planes of the body-wave radiation pattern excited by a point source divides a reference sphere around the source into areas of opposite first-motion polarities. The polarities can either be away from or toward the source for P-waves, away from or toward the source for the SV-component of the S-wave and to the left or to the right looking from the source for the SH-component of the S-wave [e.g., *Pujol*, 2003]. The first-motion polarities, observed at the seismic stations, are projected to the focal sphere at the azimuth and takeoff angle at which the seismic ray leaves the source. A focal mechanism can then be found that best fits the first-motion observations.

A widely used method for determining first-motion focal mechanisms from P, SV and SH-polarity data is the FOCMEC software package [*Snoke*, 2003]. FOCMEC employs a grid search over all possible fault-plane orientations

to identify the best-fitting focal mechanism and reports acceptable solutions based on selection criteria for the number of polarity data errors. However, no quality estimate for the solution is given and no stability check is performed in FOCMEC. We introduce an algorithm similar to that proposed by *Hardebeck and Shearer* [2002] for pure P-polarity datasets and test the stability of the focal mechanism solution by accounting for wrong polarity readings.

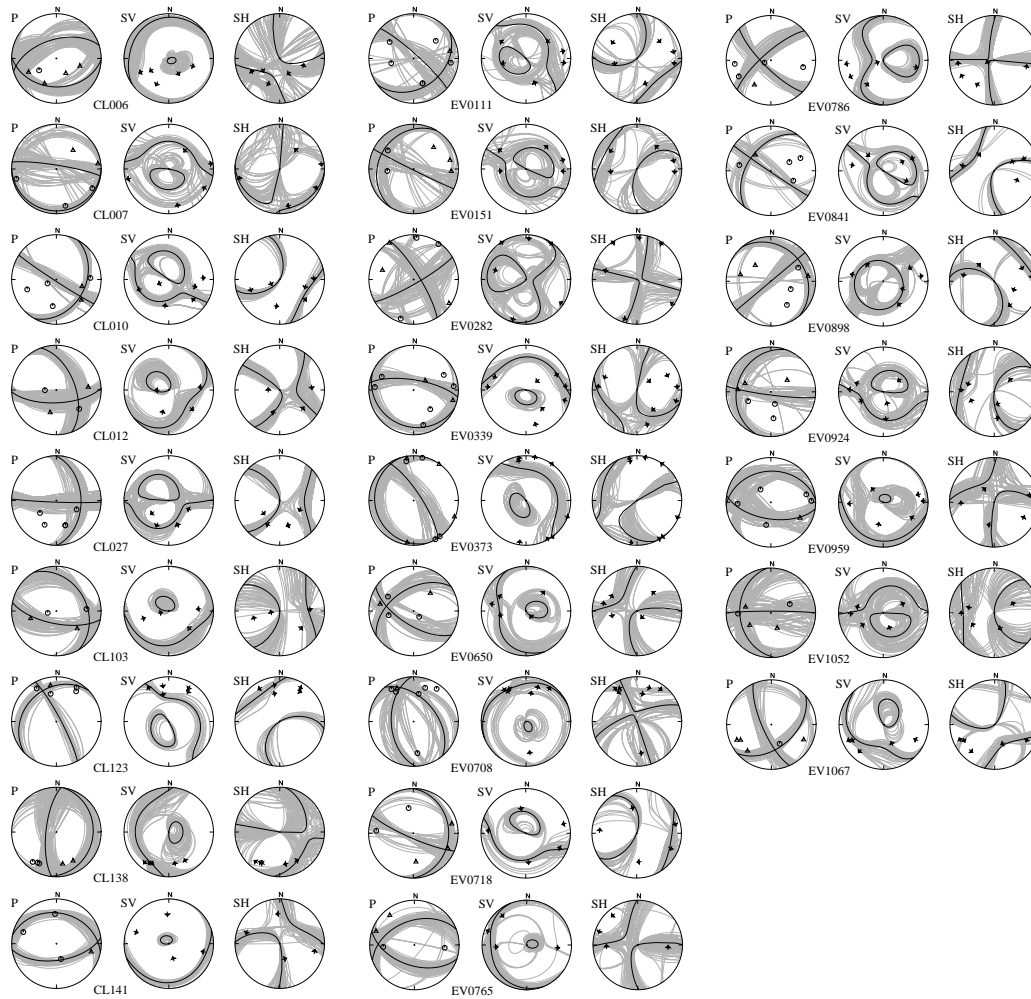


Figure 4.13: Focal mechanisms of earthquakes. 25 solutions with a minimum of 12 polarity observations and a maximum fault-plane variance of 20° are shown. Plots of the lower focal hemisphere contain nodal planes for P, SV and SH radiation for all derived solutions (light gray) and the preferred solution (black) for every cluster/event. Polarities are indicated for P (circle = up, triangle = down), SV (arrows: toward and away from source) and SH-component (arrows: to left and to right looking from source). Annotation indicates the individual cluster/event numbers.

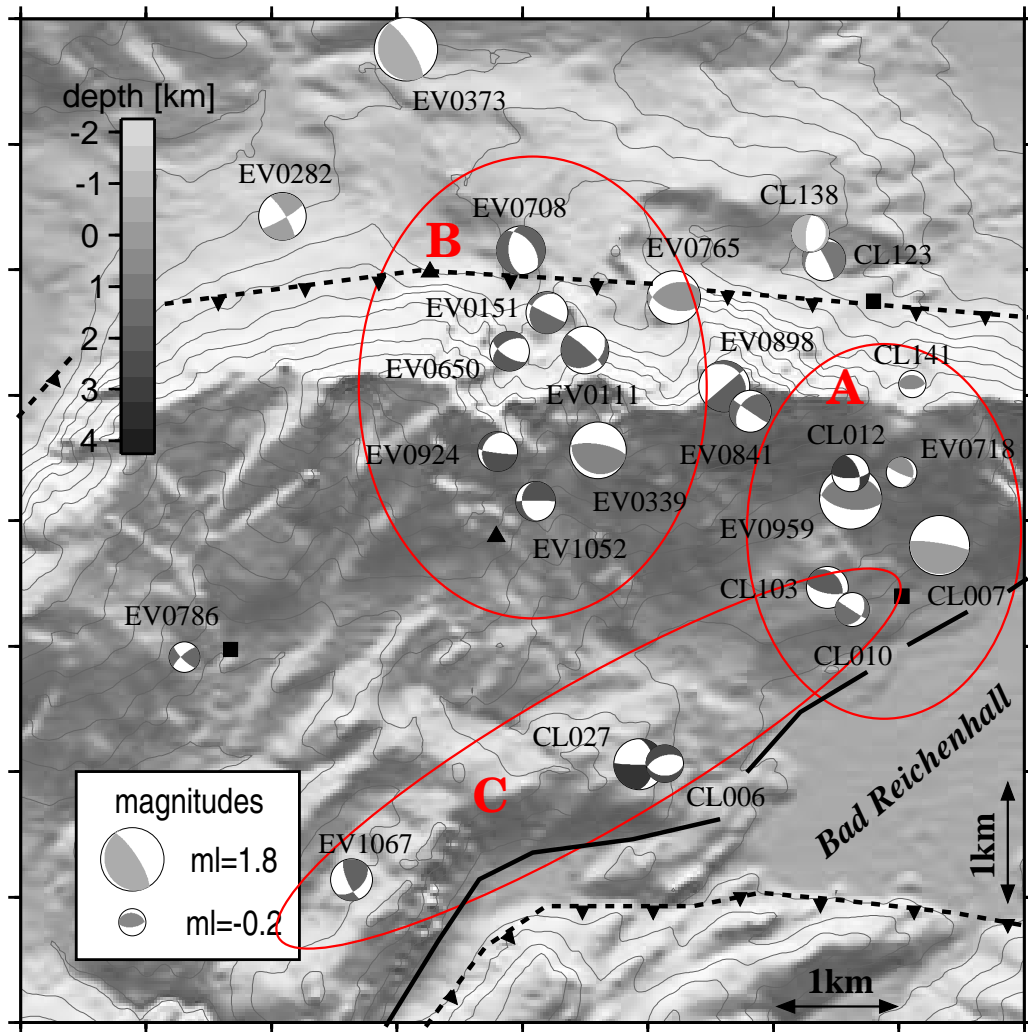
After applying a bandpass filter of 3-15 Hz the 3-component seismograms were rotated into the ray coordinate system to separate the P, SV and SH-components. The azimuth and incidence angles of the ray, needed for this rotation, were derived by a polarization analysis of the three-component recording of the P-onset. First-motion polarities were then determined in the rotated seismograms for all clusters and all events with more than five recording stations. The event clusters were treated as single events by combining the polarity information taken from seismograms of stations which had the highest signal to noise ratio. This was justified by the high similarity of the wave forms of the cluster members and by the fact that they coincide within the accuracy of the master event location technique.

FOCMEC was used to find the best fitting focal mechanism. The polarities were weighted according to the radiation pattern allowing for an absolute polarity error of two. Additionally, for all events and clusters N further FOCMEC runs were done with the same error tolerance, but each time leaving out one of the N polarity observations. Between one and fifty acceptable focal mechanisms were found for each run. Following the algorithm of *Hardebeck and Shearer [2002]* we calculated a preferred focal mechanism by vectorial averaging the normal vectors of the fault and auxiliary fault plane separately. Furthermore, we were in this way able to derive an estimate for the variance of the two normal vectors. Figure 4.13 shows the preferred focal mechanisms of 25 events with at least 12 polarity observations and a maximum normal vector variance of 20° .

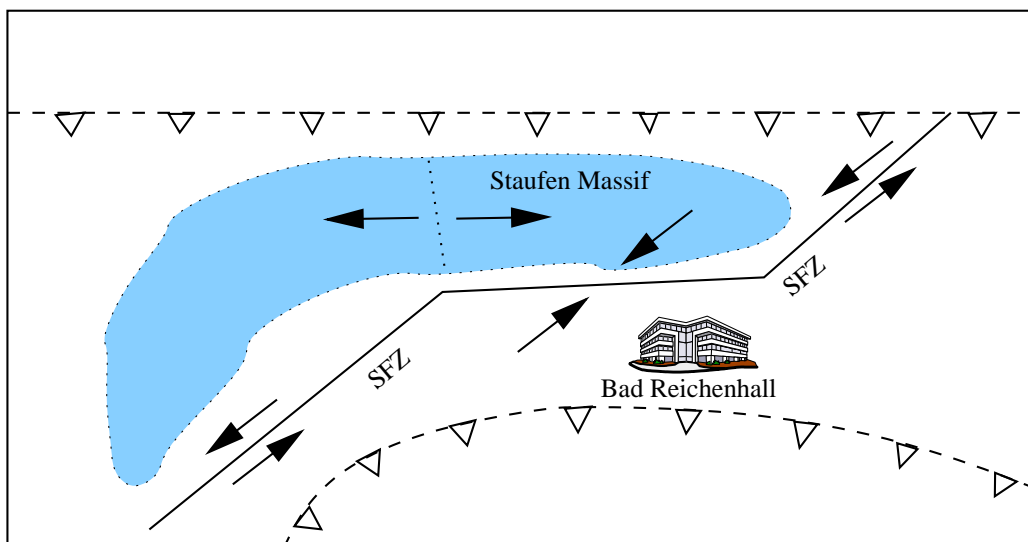
The preferred mechanisms of the nine clusters and 16 single events are plotted in an epicenter map scaled by magnitude and depth in Figure 4.14a. Three different faulting regimes, indicated by ellipses, seem to exist in the study area: (A) reverse faulting in the south-eastern part of Mt. Hochstaufen, (B) normal faulting in the central part of the Staufen Massif and (C) sinistral strike-slip faulting south of the massif near to the surface trace of the Saalachtal Fault Zone (SFZ, Fig. 4.1+4.14a [*Frisch and Gawlick, 2003*]). The number of derived focal mechanisms is not sufficient to give a definite answer to the question which tectonic processes control the seismicity of the Staufen Massif. However, the observed faulting regimes could indicate, that the SFZ is still active (C), forms a restraining bend in the south-east of the Staufen Massif (A) and further leads to extension of the central part of mountain chain (B). If this interpretation, which is illustrated in Fig. 4.14b, is valid has to be carefully tested in the future and has a major impact on seismic hazard assessment.

Name	Origin Time		Hypocenter				ml	Focal Mechanism							
	2002 UTC		lat. 47°	lon. 12°	dep.	strike		dip	rake	var.	strike	dip	rake	var.	
CL006	07.15.	23:20:21	43.67	50.41	2.6	0.4	253.00	55.00	-101.00	±17	91.72	36.48	-74.76	±15	
CL007	11.15.	08:31:35	44.59	52.18	-0.1	1.6	279.00	83.00	91.00	±17	90.85	7.07	81.91	±12	
CL010	08.24.	22:08:48	44.32	51.62	1.4	0.2	123.00	87.00	-125.00	±7	28.73	35.11	-5.22	±6	
CL012	10.11.	06:19:55	44.91	51.62	3.1	0.4	340.00	55.00	151.00	±11	87.64	66.60	38.68	±11	
CL027	05.27.	00:26:46	43.67	50.25	3.3	1.1	92.00	87.00	-134.00	±8	358.90	44.08	-4.31	±8	
CL103	08.19.	16:18:09	44.42	51.46	2.0	0.6	330.00	33.00	134.00	±10	100.97	66.93	65.72	±10	
CL123	09.21.	19:16:58	45.83	51.46	1.2	0.7	332.00	82.00	-116.00	±5	226.07	27.12	-17.78	±6	
CL138	08.15.	21:25:27	45.94	51.38	-0.9	0.4	186.00	71.00	-91.00	±14	9.07	19.03	-87.10	±16	
CL141	10.22.	00:40:55	45.29	52.02	0.6	-0.2	281.00	32.00	106.00	±8	82.32	59.38	80.23	±5	
EV0111	04.10.	16:53:47	45.45	49.93	1.8	0.9	312.00	82.00	123.00	±17	54.10	33.85	14.47	±13	
EV0151	05.03.	22:56:07	45.61	49.69	1.6	0.6	211.00	22.00	-175.00	±16	116.36	88.13	-68.08	±16	
EV0282	08.13.	04:41:08	46.04	48.01	-0.2	0.9	60.00	82.00	-169.00	±19	328.45	79.11	-8.15	±15	
EV0339	08.14.	22:49:29	45.02	50.01	0.7	1.4	114.00	19.00	104.00	±8	279.23	71.58	85.24	±8	
EV0373	08.15.	14:12:41	46.75	48.81	-0.6	1.8	327.00	76.00	86.00	±13	163.12	14.55	105.63	±11	
EV0650	08.22.	14:58:43	45.45	49.45	2.1	0.5	237.00	49.00	-145.00	±10	122.33	64.35	-46.70	±11	
EV0708	08.25.	12:27:54	45.88	49.53	1.8	1.0	320.00	48.00	-117.00	±11	177.29	48.54	-63.24	±11	
EV0718	08.25.	21:36:57	44.91	51.94	0.3	0.0	0.00	22.00	155.00	±9	113.38	80.89	69.89	±8	
EV0765	08.29.	09:53:55	45.67	50.50	0.2	0.6	108.00	52.00	116.00	±11	249.61	44.91	60.70	±11	
EV0786	09.02.	22:10:38	44.15	47.36	1.6	0.0	135.00	76.00	165.00	±7	228.71	75.46	14.47	±8	
EV0841	09.16.	14:31:50	45.18	50.98	1.6	0.6	124.00	88.00	136.00	±9	215.93	46.03	2.78	±7	
EV0898	09.30.	15:48:09	45.29	50.82	1.9	1.1	230.00	90.00	113.00	±10	320.00	23.00	0.00	±10	
EV0924	10.03.	03:43:21	45.02	49.37	2.4	0.5	200.00	25.00	-166.00	±11	97.27	84.13	-65.66	±13	
EV0959	10.07.	01:40:27	44.80	51.62	0.9	1.7	267.00	31.00	80.00	±15	98.62	59.52	95.96	±13	
EV1052	10.19.	13:05:17	44.80	49.61	2.3	0.5	270.00	87.00	-121.00	±16	175.02	31.13	-5.81	±18	
EV1067	10.25.	16:33:52	43.18	48.41	1.7	0.6	50.00	47.00	157.00	±18	156.15	73.40	45.37	±8	

Table 4.2: Source parameters of 25 events with a variance less than 20° of the fault-plane normals. For clusters the origin time of the master event is given. Hypocenter coordinates are given in minutes form 47° for latitude and from 12° for longitude. Depth is given in km b.s.l. Local magnitude (ml) is given for the master event or single event. For the preferred focal mechanism the orientation of the fault and auxiliary fault plane are given as dip, strike and rake in degrees following the convention of *Aki and Richards* [1980]. The variance of the fault-plane normals is given in degree for both planes. A epicenter map of this events can be found in Figure 4.14a.



(a)



(b)

4.7 Discussion

We have relocated 612 earthquakes of the 2002 Mt. Hochstaufen seismicity. By cross-correlation based cluster analysis 145 groups of similar earthquakes with up to 16 members were identified. Highly similar events are partly also clustered in time and reactivation of seismogenic regions over time occurs. However, the seismicity is concentrated in different source regions in the beginning and end of 2002.

Even though only the vertical component was considered in the cluster analysis, cluster members are characterized by having very similar wave forms also in the horizontal components. Furthermore, the high similarity is preserved over the complete length of the seismograms, even though, the strength of the earthquakes within a cluster can span two magnitudes. This indicates that for the observed magnitude range, the waveforms are nearly independent of the source-time function and are predominantly influenced by the Green function of the medium and the focal mechanisms. However, because of the high waveform similarity the latter two seem to be nearly identical within a cluster.

For all identified clusters a multi-event semi-automatic phase repicking improved the accuracy of onset-time determination. By taking advantage of the simultaneous display of all cross-correlation aligned one-component seismograms. Phase onsets were in this way identified more easily by tracking consistent wave forms over several traces. A quality check of the onset times demonstrated high consistency between individual cluster members with a standard deviation of relative arrival-time differences of $\sigma^{cl} \leq 0.012$ s.

Figure 4.14: Epicenter map of the 25 derived focal mechanisms. a) Depth is indicated as gray scaled compressional quadrants of the focal mechanisms. Negative values correspond to altitude above sea level. The size of the beach balls is proportional to local magnitude. Source parameters of the clusters/events are given in Table 4.2. Three faulting regimes seem to exist and are indicated: (A) reverse, (B) normal and (C) sinistral strike-slip faulting. Major tectonic elements are taken from Frisch & Gawlick (2003): Saalachtal Fault Zone (SFZ, solid line), major thrust faults (dashed lines). b) Cartoon of a possible tectonic interpretation (see text).

The absolute hypocenter location, calculated by a probabilistic non-linear method using the software package NonLinLoc [Lomax *et al.*, 2000], are of good quality. This is indicated by location uncertainties smaller than 0.6 km and root mean square (RMS) residuals of less than 0.1 s for the majority of the events (75%). Relative locations with respect to the strongest event of a cluster were derived using the master-event technique. Unfortunately, the estimated errors are of comparable size as the obtained distances between master and slave events. This prohibits a detailed interpretation of the geometrical distribution of the events within the clusters. The master-event relocation significantly reduced the dimensions of the earthquake clouds compared to the probabilistic result down to a size of a few meters.

Compared to previous location results, where the seismicity was diffusely distributed below the Staufen Massif [Kraft *et al.*, 2006a], spatial and temporal patterns in the seismicity can now be clearly identified. Earthquake hypocenters were located in a depth range between -1.7 km to 4.2 km (b.s.l.) with the majority of events deeper than -1 km, which means that earthquakes in the Staufen Massif can occur more 1000 m above the Reichenhall Basin. During the March swarm sequence, the seismicity mainly concentrates in a very small source volume in 3 km depth south of Mt. Hochstaufen, which coincides with the surface trace of the sinistral Saalachtal Fault Zone. Later in the year, mainly during the swarm sequences starting in August, the seismicity is distributed over a larger source volume inside the Staufen Massif. Hypocenters seem to align along two planes. One striking north-south and dipping west, the second plane strikes east-west with a nearly horizontal southern dip very shallow beneath the mountain chain. Neither of the planes can with reasonable certainty be associated with geological features observed in the study area.

Further, we have combined the focal-mechanism determination based on first-motion polarities of P and S-waves [Snoke, 2003], with a stability check and fault-plane variance estimator proposed by Hardebeck and Shearer [2002]. 25 focal-mechanism solutions with at least 12 first-motion observations and a fault-plane variance less than 20° were found. The focal mechanism seem to indicate that the sinistral Saalach Fault Zone poses an important tectonic boundary condition in the Mt. Hochstaufen area. Still active sinistral fault displacement may cause reverse faulting in a restraining bend at the southeastern end of the Staufen Massif and normal faulting in the central part of the mountain chain. However, the number of derived focal mechanisms is not

sufficient to give a definite answer to the question which tectonic processes control the seismicity of the Staufen Massif.

4.8 Conclusions

We have improved the location accuracy of the 2002 Mt. Hochstaufen seismicity by introducing a pseudo-3D-velocity model with topography and by using a probabilistic, non-linear location method. Additional improvement was achieved by analyzing wave-form similarities and relative relocation of groups of similar events.

The seismicity is mainly concentrated in the Staufen Massif and to depths less than 4 km. Several swarm-type earthquake sequences can be identified, which synchronously start with above-average rain events. A migration to depth can clearly be observed for the strongest earthquake swarm starting on August 8. This indicates that the seismic activity may be triggered by diffusion of rain water to seismogenic depth. Evidence for this hypothesis, based on our relocations, was recently reported by *Hainzl et al.* [2006] successfully predicting the seismic event rate from the calculated pore-pressure change at depth due to rainfall.

The derived focal mechanisms seem to indicate active sinistral displacement on the Saalachtal Fault Zone. Although, due to the small number of available focal mechanism a definite answer can not be given, this interpretation has to be tested carefully in the future and has major impact on seismic hazard assessment.

Further improvement of the earthquake location and focal mechanism determination could be archived by improving the velocity model of the Mt. Hochstaufen area. This could be achieved by passive tomographic methods, however a denser seismological network would be as essential as a sufficient number of recorded earthquakes. Between April to September 2004, a dense network of 12 seismological station was installed around Mt. Hochstaufen. Additionally an earthquake swarm started in July 2005 synchronously with an intense rain event comparable to the one in August 2002. The data is currently analyzed and may help to identify the mechanism which drives the crust in the Staufen area so close to failure.

4.9 Acknowledgements

This study was to a major part supported by the Bavarian Ministry for Environment and by the Geological Survey of the Bavarian State. Toni Kraft was partially supported by the German Research Foundation (DFG) and the EU Community initiative INTERREG III B Alpine Space Programme SIS-MOVALP. We thank the Bavarian Forest Administration for permitting the installation of mobile stations and access to forest roads. Special thanks are expressed to the communities of Bad Reichenhall, Inzell, Piding, Teisendorf, and Siegsdorf, to the tourist club "Die Naturfreunde", as well as to Mr. Waigl and Mrs. Kerkmann for the permission to install seismological stations on their properties. We like to thank the following persons for giving logistic and technical support throughout the study and field campaign: Werner Bauer, Peter Danecek, Teresa Reinwald, Martin Beblo, Martin Feller, Erwin Geiß, Gunnar Jahnke and Christian Verard. We want to acknowledge our gratitude to Roco Malservisi for his careful review and helpful discussions. Finally, we thank two anonymous reviewers for their useful comments, which helped to improve the original manuscript.

Chapter 5

Evidence for Rainfall-Triggered Earthquake Activity

Fluids are known to be of major importance for the earthquake generation because pore pressure variations alter the strength of faults. Thus they can initiate earthquakes if the crust is close enough to its critical state. Based on the observations of the isolated seismicity below the densely monitored Mt. Hochstaufen, SE Germany, we are now able to demonstrate that the crust can be so close-to-failure that even tiny pressure variations associated with precipitation can trigger earthquakes in a few kilometer depth. We find that the recorded seismicity is highly correlated with the calculated spatiotemporal pore pressure changes due to diffusing rain water and in good agreement with the response of faults described by the rate-state friction law.

This chapter was published as: HAINZL, S., T. KRAFT, J. WASSERMANN, H. IGEL AND E. SCHMEDES (2006), *Evidence for rainfall-triggered earthquake activity*, *Geophys. Res. Lett.*, **33**, doi:10.1029/2006GL027642, in press.

5.1 Introduction

In recent years, hydromechanical coupling has been proposed as a possible explanation for many geological phenomena including the anomalous weakness of many major faults [e.g., *Sleep and Blanpied*, 1992], silent slip events [e.g., *Kodaira et al.*, 2004], aftershock occurrence [e.g., *Nur and Booker*, 1972; *Miller et al.*, 2004], and remote triggering of earthquakes [e.g., *Prejean et al.*,

2004]. The widely accepted understanding is that an increase of the pore fluid pressure reduces the effective normal stress and thus the strength of faults, promoting earthquake rupture. Direct evidence for fluids affecting the stability of faults comes from reservoir induced seismicity [e.g., *Talwani, 1997*], and fluid injections in wells [e.g., *Zoback and Harjes, 1997*]. Fluid triggering is also observed for natural seismicity such as earthquake swarms where the fluid source is assumed to be in depth [e.g., *Parotidis et al., 2003; Miller et al., 2004; Hainzl and Ogata, 2005*]. Furthermore, seasonal variations of the seismic activity have been found which seems to correlate with the seasonality of ground water recharge [e.g., *Saar and Manga, 2003*] and precipitation [e.g., *Muco, 1999*]. However, so far, the lack of high-resolution data did not allow to prove the effect of surface water in more detail. Based on our observations for the isolated seismicity below Mt. Hochstaufen, we are now able to show that rainfall can trigger earthquakes via the mechanism of pore pressure diffusion.

5.2 Seismicity at Mt. Hochstaufen

The Staufen Massif is an east-west striking mountain chain in SE Germany, northwest of the town Bad Reichenhall. The most prominent summit, Mt. Hochstaufen, reaches an altitude of 1775m (Fig. 5.1). Belonging to the elongated fold-and-thrust belt of the Northern Limestone Alps, the geology of the Staufen Massif is dominated by lower to middle Triassic limestone and dolomite [e.g., *Bögel and Schmidt, 1976*]. Since more than 600 years ago, earthquakes with maximum macroseismic intensities of $I_0 = V$ have been reported in this region, which is embedded in an almost quiet surrounding. The majority of the earthquakes occurs in the summer months, which are also characterized by having the highest average precipitation values during the year [*Kraft et al., 2006a*]. To explore the underlying mechanisms, seismic monitoring of the Bad Reichenhall area was initiated in 2001, consisting of six permanent and three mobile short period stations (see locations in Fig. 5.1). In 2002, this network recorded more than 1100 earthquakes with a maximum magnitude of $M_l = 2.4$, mainly concentrated in two swarm type sequences following above-average rainfall in March and August. For the first time, these data allow a detailed analysis of the activity in this rare example of an isolated but critical system.

The observed seismicity is inconspicuous in its magnitude-frequency distribution that follows the Gutenberg-Richter law with a typical b -value of

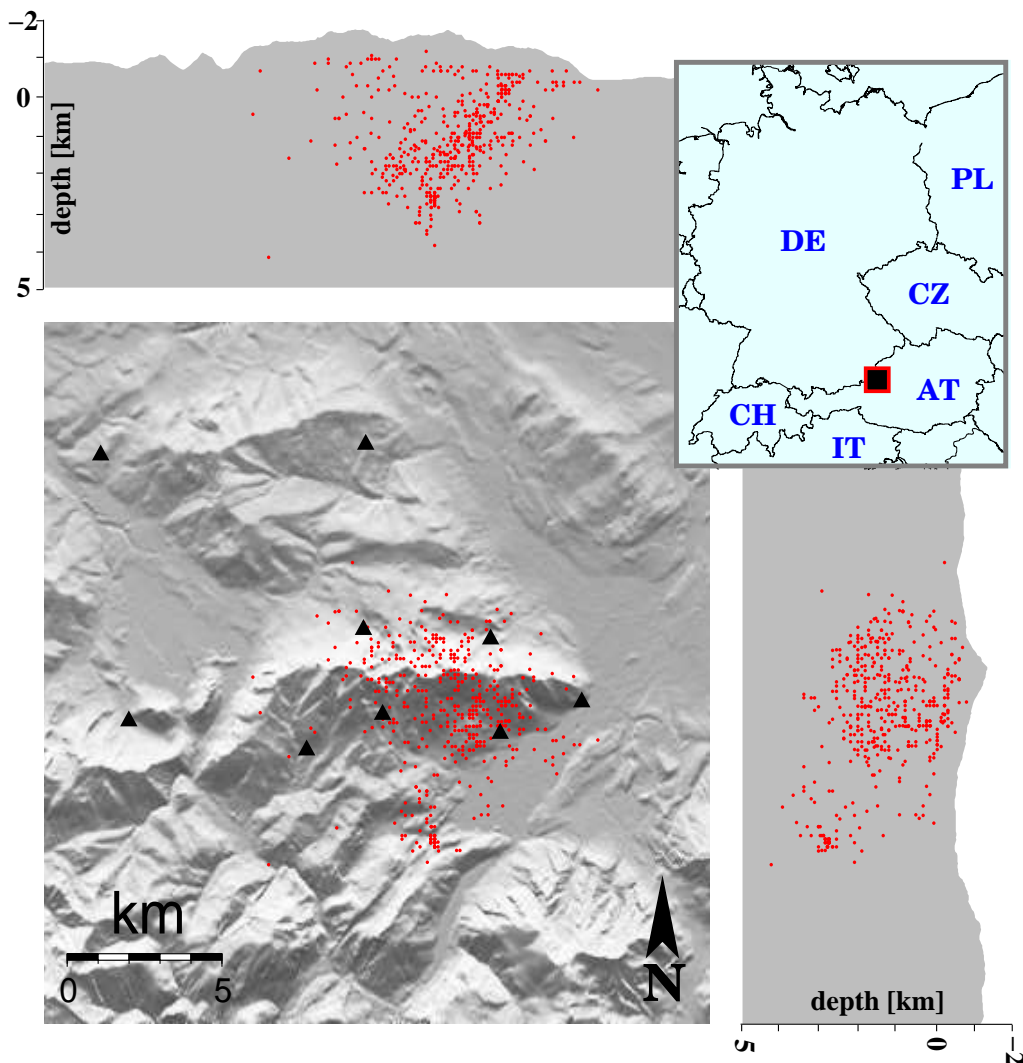


Figure 5.1: Map of Staufen Massif as well as EW and NS profiles through the summit of Mt. Hochstaufen (1775m) with the located earthquakes in the year 2002 (dots). Map borders are longitude $12^{\circ}40' - 12^{\circ}57' E$ and latitude $47^{\circ}40.5' - 47^{\circ}55.5' N$. Triangles mark seismological stations installed in 2002.

1.1 ± 0.1 for magnitudes larger than $M_l = -0.2$. Below this value the distribution deviates from the Gutenberg-Richter law, indicating incomplete data collection. We therefore restrict our analysis to $M_l \geq -0.2$ events. Hypocenter locations are derived for a subset of these events using a 2D-velocity model with topography. Groups of events with very similar wave forms are identified by cluster analysis and relocated using the master event technique [Kraft *et al.*, 2006b]. In this way, over 500 locations were obtained, shown as points in Figure 5.1.

5.3 Seismicity Model

In order to test the hypothesis that rainfall triggered seismicity, we calculate the pore-fluid pressure changes at depth in response to the surface rain. Assuming a homogeneous crust and spatially uniform rainfall, we can restrict our analysis to the one-dimensional case. The process of fluid pressure relaxation can be approximately characterized by a system of equations describing the dynamics of fluid saturated porous elastic solid [Biot, 1962]. A diffusion equation describing the evolution of fluid mass alteration per unit volume, m , can be uncoupled [Rudnicki, 1986; PHASE Research project, 2005]

$$\frac{\partial m}{\partial t} = D \frac{\partial^2 m}{\partial z^2} + Q(z, t) \quad , \quad (5.1)$$

where z is the depth coordinate, D the hydraulic diffusivity, and $Q(z, t)$ a fluid mass source. If porosity is assumed to be constant, the alteration of pore pressure p is proportional to the mass alteration m and the same equation holds for the pore pressure alteration where $Q(z, t)$ now defines the pressure source. The solution of the diffusion equation is given by

$$p(z, t) = \int_{-\infty}^t \int_{-\infty}^{\infty} 2G(z - z_0, t - \tau) Q(z_0, \tau) dz_0 d\tau \quad (5.2)$$

with Green's function $G(z - z_0, t - \tau) = [4\pi D(t - \tau)]^{-0.5} \exp[-(z - z_0)^2/4D(t - \tau)]$ [Barton, 1989]. The factor of 2 results from the fact that the total fluid mass which can only migrate into depth must be conserved [Landau and Lifschitz, 1966]. In our case, the source is given by the linearly interpolated rain rate measured at four daily sampled meteorologic stations surrounding Mt. Hochstaufen. Because we are only interested in pressure deviations from the stationary state, we consider the deviation of the rainfall from the long-term mean, namely $Q(z, t) = \rho g(h(t) - \bar{h})\delta(z)$. The average rain amount \bar{h} is calculated from the precipitation data from 1995-2001 at the same meteorological stations. To avoid boundary effects, we start the integration of Eq.(5.2) at 1/1/2001.

To quantify the effect of the pressure changes on seismicity, we use the framework of rate-state friction [e.g., Dieterich, 1994; Dieterich et al., 2000] which properly takes into consideration the rate- and slip-dependence of frictional strength and time-dependent restrengthening observed in laboratory experiments. This concept has already been successfully applied to

explain earthquake clustering in nature such as aftershock activity [e.g., *Scholz*, 1998]. In this theory, the seismicity rate λ is inversely proportional to the state variable γ describing the creep velocities on the faults, namely $\lambda(z, t) = r/(\dot{\tau}\gamma(z, t))$, where r is the stationary background rate and $\dot{\tau}$ the tectonic loading rate. The evolution of the state variable is given by $d\gamma = (dt - \gamma dCFS)/(A\sigma)$ with A being a dimensionless fault constitutive parameter usually ~ 0.01 [e.g., *Dieterich*, 1994; *Dieterich et al.*, 2000]. In our case, the Coulomb failure stress CFS changes due the constant stressing rate $\dot{\tau}$ and the variation of the pore pressure p , altering the effective normal stress $\sigma = \sigma_n - p$ on the faults. We track the evolution of γ by considering sufficiently small times steps leading to stress increments of $\Delta CFS(z, t) = \dot{\tau}\Delta t + \mu(p(z, t + \Delta t) - p(z, t))$. We choose time steps of 0.5 days and set the coefficient of friction μ to the typical value of 0.6 [?]. The state variable is iterated according to

$$\dot{\tau}\gamma(z, t + \Delta t) = \dot{\tau}\gamma(z, t)e^{-\frac{\Delta CFS}{A\sigma}} + \frac{\Delta t}{t_a} \quad (5.3)$$

starting from the background level, that is, $\dot{\tau}\gamma(z, 0) = 1$. Because the pressure changes are assumed to be much smaller than the effective normal stress, we can use $A\sigma$ as a constant free parameter. The rate depends additionally on the value of the background rate r , the relaxation time $t_a = A\sigma/\dot{\tau}$, and implicitly on the hydraulic diffusivity D .

5.4 Results

The estimation of the four parameters is carried out by the maximum likelihood method. The likelihood function L , which is the joint probability function for a given model, is constructed by multiplying the probability density function of each of the data points together. For a given rate $\lambda(z, t)$, the log-likelihood with respect to the N earthquakes occurring at the depth interval $[z_o, z_1]$ at times t_i can be determined by

$$\ln L(r, t_a, A\sigma, D) = \sum_{i=1}^N \ln \lambda(z_i, t_i) - \int_{t_s}^{t_e} \int_{z_0}^{z_1} \lambda(z, t) dz dt, \quad (5.4)$$

where $t_s=1/1/2002$ is the starting and $t_e=1/1/2003$ the ending time of the activity [e.g., *Ogata*, 1998; ?]. We account for the uncertainty of earthquake locations by evaluating the formula (5.4) for z_i which are Gaussian distributed around the determined values. According to the localization procedure, the location errors vary between 50m and 2km with a median of 200m.

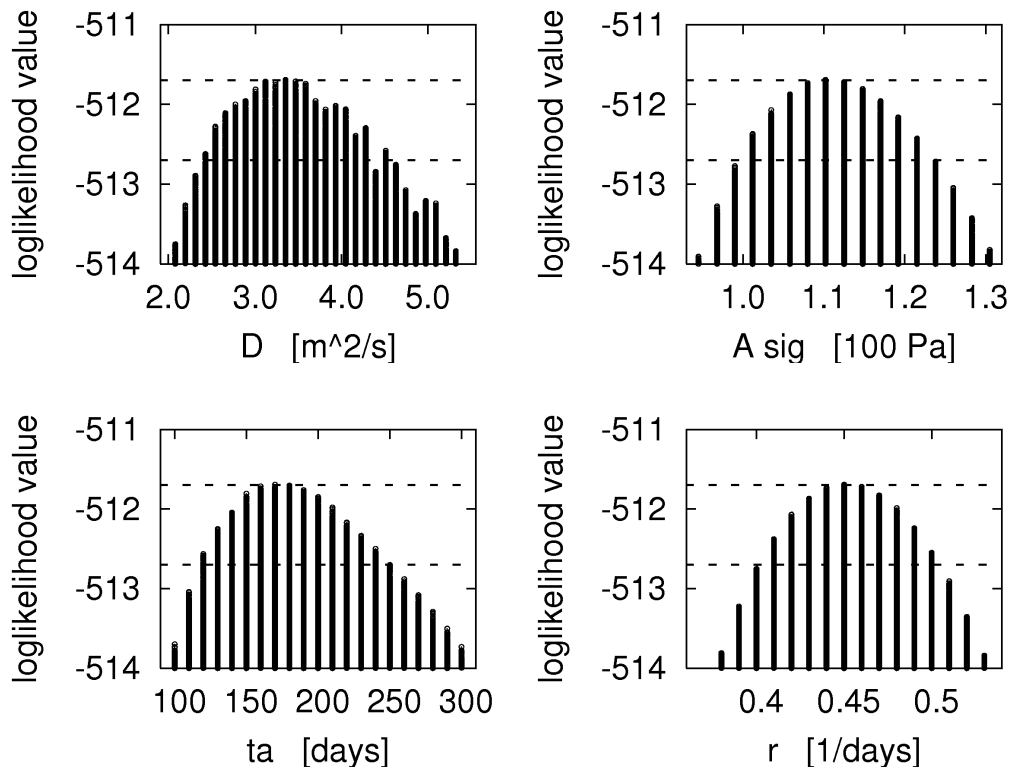


Figure 5.2: The result of the parameter search for maximizing the likelihood value. Additionally, the maximum as well as the 63% decrease of the likelihood value are plotted as horizontal lines.

For the earthquakes in the depth interval 1-4 km, the result of the parameter grid-search is illustrated in Figure 5.2. The maximization of the likelihood function (Eq. 5.4) yields $r=0.45\pm 0.05$ [days⁻¹], $t_a=180\pm 60$ [days], $A\sigma=110\pm 10$ [Pa] and a hydraulic diffusivity $D=3.3\pm 0.8$ m²/s, where the errors refer to a 63%-decrease of the likelihood function. Considering a typical value of $A=0.01$, our estimated $A\sigma$ -value would yield an effective normal stress of only 11 [kPa] which requires very high in situ pore pressure in this region (see further discussion in section 5.5). The resulting diffusivity value, which corresponds well to the range of values obtained from fluid injection experiments [e.g., Shapiro *et al.*, 1997], is slightly higher than the previously estimated value for the same region of 0.75 ± 0.35 m²/s [Kraft *et al.*, 2006a]. However, the previous result is based only on fitting single pressure-front curves to first locations of the observed activity and did not incorporate the complete pressure field.

Using our estimated value for hydraulic diffusivity, we calculate now the pore pressure variations at depth from the observed rainfall (Fig. 5.3a).

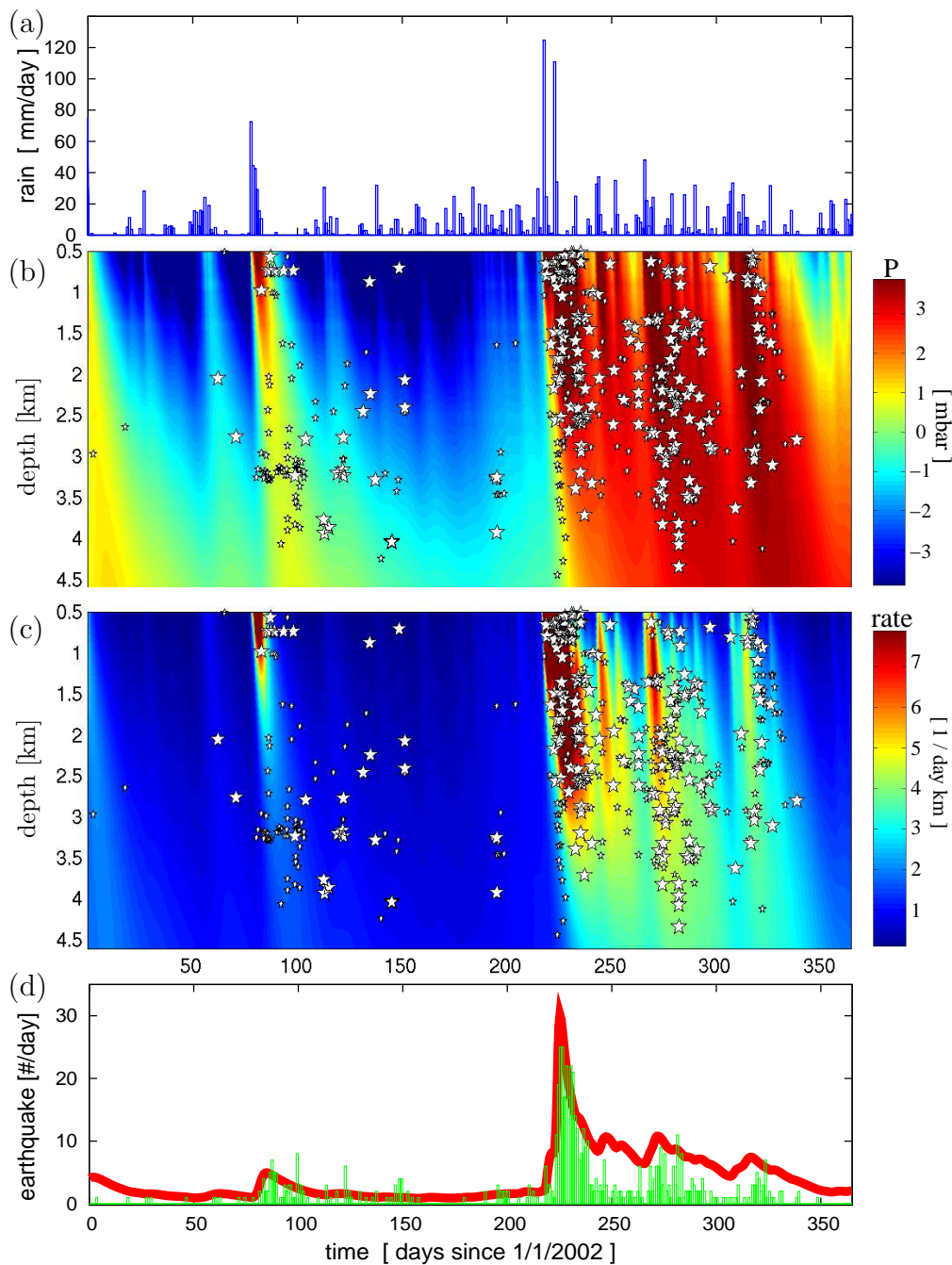


Figure 5.3: The spatiotemporal pattern of (b) pore pressure and (c) estimated earthquake rate as the result of the surface rain rate (a) in the case of one-dimensional linear diffusion with hydraulic diffusivity $D=2.9 \text{ m}^2/\text{s}^2$. Earthquake locations are marked by white stars (big: errors $\leq 100\text{m}$). (d) shows the daily number of detected earthquakes (green) in comparison with the theoretical rate for the 1-4 km depth interval (red).

The comparison of the observed seismic activity with the resulting spatio-temporal pressure field is shown in Figure 5.3b and with the forecasted earthquake rate in Figure 5.3c. In either case, the observed seismicity (indicated by stars) corresponds well to elevated values of the calculated functions, indicating a strong spatial and temporal correlation. In Figure 5.3d, the calculated and observed earthquake rate, including also the events without hypocenter information ($M_l \geq -0.2$), are compared in the form of time series representing the number of earthquakes per day.

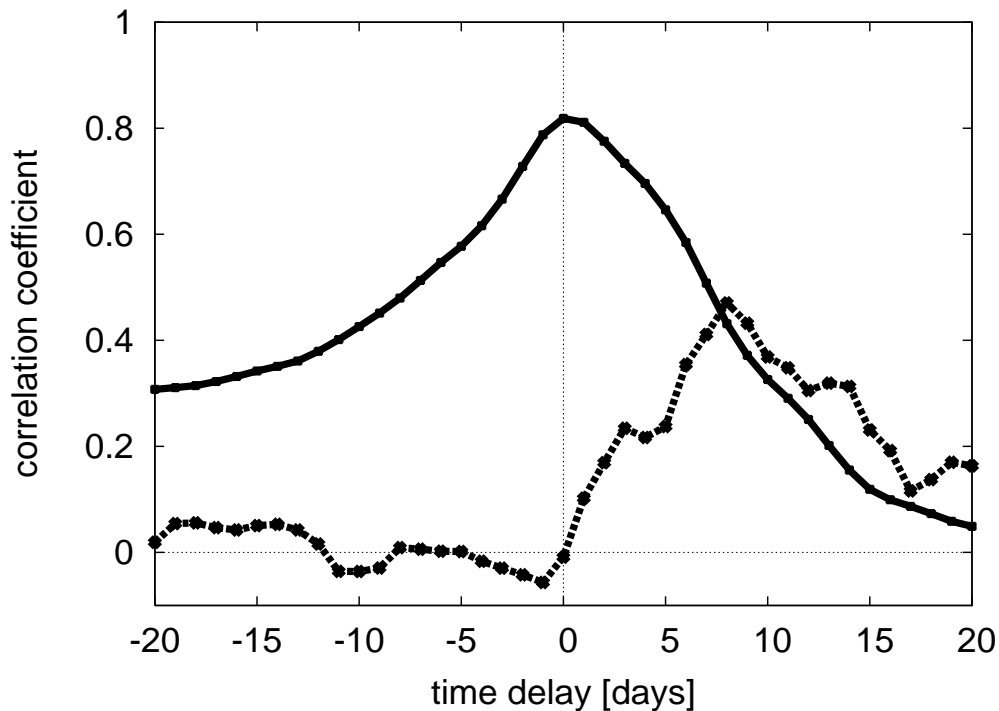


Figure 5.4: The linear correlation coefficient as a function of the time shift between the time series of the daily observed number of earthquakes and (i) the daily rain amount (dashed line) and (ii) the theoretical rate of earthquakes in the 1-4 km depth interval (solid line).

The correlation between these time series and between those of observed earthquake rate and rainfall is quantified by their cross-correlation coefficient, shown in Figure 5.4. While the seismicity is not correlated with the rain data at zero time delay, it shows some correlation if the seismicity is shifted backwards 8 days ($R_{max}=0.47$). On the other hand, the earthquake rate calculated from the pore pressure changes at depth is strongly correlated at zero delay time with a maximum correlation coefficient, almost doubling that

of the rain data ($R_{max}=0.82$). Note that the value of the hydraulic diffusivity that maximizes the likelihood function in Eq. (5.4), is also found to maximize the linear correlation coefficient indicating the consistency of our parameter estimation.

5.5 Discussion

The high correlation indicates that our model is a good approximation of the underlying processes, although we have strongly simplified the real world. In particular, the crust is assumed to be a homogeneous half-space which certainly is an over-simplified model of the local geology, where systems of open fractures are observed [Weede, 2002] extending from the surface to depth of at least 100m. Thus a likely situation is a localized channeling of larger volume of precipitation into a limited number of open fractures, resulting in strongly amplified hydraulic head changes. If fluid diffusion is assumed to be confined within deep fracture zones, the physics of rate-state friction and fluid pressure diffusion within an equivalent porous medium model (e.g., Berkowitz et al. 1988) would be the same. The only effect would be that the estimated value of the parameter $A\sigma$ would be amplified in the same way as the pressure, because the evolution of the state variable $\dot{\tau}\gamma$ (Eq. 5.3) is invariant under identical amplification of p , $\dot{\tau}$, and $A\sigma$.

Furthermore, we have neglected in our model seasonal effects such as snow coverage as well as coseismic stress changes induced by the earthquakes themselves, which are known to trigger local aftershocks according to the Omori law [Stein, 1999]. Previous studies of natural swarm activity in the Vogtland region, Central Europe, indicate that aftershock sequences are embedded in the swarm activity and can even dominate it [Hainzl and Ogata, 2005]. However, for the Mt. Hochstaufen region, simple stacking of the activity relative to the largest events indicates that aftershocks play only a minor role. Assuming homogeneous conditions, the absolute pressure variation during the year is found to be between 0.5 - 1.3 kPa in the depth range between 1-4 km, where most of the earthquakes occurred. This is in the same range as the effects of earth tides [Tolstoy et al., 2002]. However, inserting tidal stresses (calculated from volume strain at 2 km depth below Bad Reichenhall) as the loading mechanism into our model yields a maximum effect of only 15% compared to the rainfall induced rate changes. The underlying reason is the higher frequency of the tidal stress changes. The relative effect of tides would

be further reduced in the likely case that rain is collected in open fracture systems at the surface (see above).

5.6 Conclusions

Although some seasonal variability of seismicity related to ground water recharge and precipitation has been previously observed [*Saar and Manga, 2003; Muco, 1999*], we can show here for the first time a statistically significant causal relationship between rainfall and earthquake activity for an isolated region. Our analysis of the high quality meteorological and seismic data in the Mt. Hochstaufen region yields clear evidence that pore pressure changes induced by rainfall are able to trigger earthquake activity even at 4 km depth via the mechanism of fluid diffusion. Assuming homogeneous condition, stress changes of the order of millibar are found to trigger the earthquakes. This is much less than usually observed for the bulk of induced earthquakes in fluid injection experiments (in the order of 10 bar), even though some fraction of those events has been triggered by similar tiny pressure changes [*Zoback and Harjes, 1997; PHASE Research project, 2005*]. Our results indicate an extreme sensitivity of the crust with regard to minute changes. However, the existence of deep open faults channeling larger volume of precipitation would lead to significantly higher stress changes which could explain the sensitivity of the seismogenic volume in the Mt. Hochstaufen region. In any case, the high correlation between rain-induced pressure changes at depth and seismicity opens the possibility of forecasting future earthquake rates on the basis of rainfall data in this region.

5.7 Acknowledgments

The authors want to thank Serge Shapiro and two anonymous reviewers for their fruitful comments as well as Jim Dieterich and Agnes Helmstetter for helpful discussion of the rate-state friction framework. Furthermore, we are thankful to Thomas Jahr for calculating the tidal effects and Ed Sobel for carefully reading the manuscript. This work was supported by the Deutsche Forschungsgemeinschaft (SCHE280/14-2 and Ig16/7), Bavarian Ministry for Environment, and the EU Community initiative INTERREG III B Alpine Space Programme SISMOVALP.

Bibliography

- Ahern, T. K., R. Casey, D. Barnes, R. Benson, and T. Knight (2006), SEED Reference Manual, Standard for the Exchange of Earthquake Data, <http://www.iris.edu/manuals/>.
- Aki, K., and P. Richards (1980), *Quantitative Seismology, Theory and Methods*, Freeman and Company, San Francisco.
- Angenheister, G., H. Bögel, H. Gebrande, P. Giese, P. Schmidt-Thome, and W. Zeil (1972), Recent investigations of surficial and deeper crustal structures of the eastern and southern Alps, *Geol. Rundschau*, 61(2), 349–395.
- Aster, C. R., and C. Rowe (2000), *Automatic phase picking refinement and similar event association in large seismic datasets*, pp. 231–263, Kluwer, Amsterdam.
- Baisch, S., M. Bohnhoff, L. Ceranna, Y. Tu, and H.-P. Harjes (2002), Probing the crust to 9 km depth: Fluid-injection experiments and induced seismicity at the KTB super-deep drilling hole, Germany, *Bull. Seism. Soc. Am.*, 92(6), 2369–2380, doi:10.1785/0120010236.
- Bakun, W., and W. Joiner (1984), The ML scale in central California, *Bull. Seism. Soc. Am.*, 74, 1827.
- Barrett, D. J., and R. Silverman (2001), *SSH, the secure shell: The definitive guide*, O'Reilly.
- Barton, G. (1989), *Elements of Green's functions and propagation - Potentials, diffusion and waves*, Oxford University Press.
- Biot, M. (1962), Mechanics of deformation and acoustic propagation in porous media, *J. Appl. Phys.*, 33(4), 1482–1498.
- Bleibinhaus, F., and H. Gebrande (2006), Crustal structure of the Eastern Alps along the TRANSALP profile from wide-angle seismic tomography, *Tectonophysics*, 414, 51–69, doi:10.1016/j.tecto.2005.10.028.

- Bögel, H., and K. Schmidt (1976), *Kleine Geologie der Ostalpen*, 231 pp., Ott Verlag Thun, Switzerland.
- Bosl, W., and A. Nur (2002), Aftershocks and pore fluid diffusion following the 1992 Landers earthquake, *J. Geophys. Res.*, *107*(B12), 1–12.
- Braitenberg, C. (2000), Non-random spectral components in the seismicity of NE Italy, *Earth Planet. Sci. Lett.*, *179*, 379–390.
- Bräuer, K., H. Kämpf, G. Strauch, and S. M. Weise (2003), Isotopic evidence ($^3\text{He}/^4\text{He}$, $^{13}\text{C}_{\text{CO}_2}$) of fluid-triggered intraplate seismicity, *J. Geophys. Res.*, *108*, 3–1, doi:10.1029/2002JB002077.
- Byerlee, J. (1993), Model for episodic flow of high-pressure water in fault zones before earthquakes, *Geology*, *21*, 303–306.
- CompuServe Inc. (1990), Graphics interactive format (sm) version 89a, <http://www.w3.org/Graphics/GIF/spec-gif89a.txt>.
- Cooley, J. W., and O. W. Tukey (1965), An algorithm for the machine calculation of complex fourier series, *Math. Comput.*, *19*, 297–307.
- Costain, J. K., and G. A. Bollinger (1991), Correlation between streamflow and intraplate seismicity in central Virginia, USA, seismic zone: Evidence for possible climatic controls, *Tectonophysics*, *186*, 193–214.
- Dahlheim, H.-A., H. Gebrande, E. Schmedes, and H. Soffel (1997), Seismicity and stress field in the vicinity of the KTB location, *J. Geophys. Res.*, *102*, 18,493–18,506, doi:10.1029/96JB02812.
- de Hoon, M. J. L., S. Imoto, J. Nolan, and S. Miyano (2004), Open source clustering software, *Bioinformatics*, *20*(9), 1453–1454, doi:10.1093/bioinformatics/bth078.
- Deichmann, N., and M. Garcia-Fernandez (1992), Rupture geometry from high-precision relative hypocenter location of microearthquake clusters, *Geophys. J. Int.*, *110*, 501–517.
- Dieterich, J. H. (1994), A constitutive law for rate of earthquake production and its application to earthquake clustering, *J. Geophys. Res.*, *99*, 2601–2618.
- Dieterich, J. H., V. Cayol, and P. Okubo (2000), The use of earthquake rate changes as a stress meter at Kilauea volcano, *Nature*, *408*, 457–460.

- Eimeren, B., H. Gerhard, and B. Frees (2003), ARD/ZDF Online Studie 2003. Internetverbreitung in Deutschland: Unerwartet hoher Zuwachs, *Media Perspektiven*, 8, 338–358.
- El-Rabbany, A. (2002), *Introduction to GPS: The global positioning system*, Artech House, Inc., Norwood, Massachusetts, USA.
- Emmermann, R., and J. Lauterjung (1997), The German Continental Deep Drilling Program KTB: Overview and major results, *J. Geophys. Res.*, 102, 18,179–18,202, doi:10.1029/96JB03945.
- Erhardt, W. (1931), Der Staufeu: Geologische Aufnahme der Berge zwischen Reichenhall und Inzell, *Wiss. Veröffentlichungen d. Deutschen u. Österreichischen Alpenvereins*, 11, 52.
- Essen, H.-H., F. Krüger, T. Dahm, and I. Grevemeyer (2003), On the generation of secondary microseisms observed in northern and central Europe, *J. Geophys. Res.*, 108(B10), 2506, doi:10.1029/2002JB002338.
- Ferreira, J. M., R. T. Oliveira, M. Assumpcao, J. A. M. Moreira, R. G. Pearce, and M. K. Takeya (1995), Correlation of seismicity and water level in the Acu Reservoir; an example from Northeast Brazil, *Bull. Seism. Soc. Am.*, 85(5), 1483–1489.
- Fischer, T. (2003), The August-December 2000 earthquake swarm in NW-Bohemia: The first results based on automatic processing of seismograms, *J. Geodyn.*, 35, 59–81, doi:10.1016/S0264-3707(02)00054-6.
- Flanagan, D. (2002), *JavaScript: The definitive guide*, O'Reilly.
- Frank, H. (1996), *Erläuterungen zur Geologischen Karte von Bayern 1:500 000*, chap. Geologie Bayerns – ein Überblick, pp. 1–15, 4. neubearbeitete Auflage ed., Bayerisches Geologisches Landesamt, Munich.
- Free Software Foundation (1991), *GNU General Public License*, Free Software Foundation, Inc., Boston, Massachusetts, USA.
- Fremont, M.-J., and S. D. Malone (1987), High precision relative localization of earthquakes at Mount St. Helens, Washington, *J. Geophys. Res.*, 92(B10), 10,223–10,236.
- Frisch, W., and H.-J. Gawlick (2003), The nappe structure of the central Northern Calcareous Alps and its disintegration during Miocene tectonic extrusion - A contribution to understanding the orogenic evolution of the Eastern Alps, *Int. J. Earth Sci.*, 92, 712–727.

- Fuchs, T., J. Rapp, and B. Rudolf (1999), *Klimastatusbericht 1999*, chap. Niederschlagsanalyse zum Pfingsthochwasser 1999 im Einzugsgebiet von Donau und Bodensee, pp. 26–34, Deutschen Wetterdienst, Offenbach/Main.
- Gailly, J.-L., and M. Adler (1993), gzip the data compression program, <http://www.gzip.org/>.
- Gebrande, H., H. Miller, and E. Schmedes (1977), Digital registrations of the aftershocks of the Friuli earthquake 1976, *Publ. Inst. Geophys. Polish Acad. Sci.*, 117, 75–84.
- Geller, R. J., and C. S. Mueller (1980), Four similar earthquakes in central California, *Geophys. Res. Lett.*, 7, 821–824.
- Gephart, J. W., and D. W. Forsyth (1984), Improved method for determining the regional stress tensor using earthquake focal mechanism data: Application to the San Fernando earthquake sequence, *J. Geophys. Res.*, 89, 9305–9320.
- Giessberger, H. (1918), Das Reichenhaller Einsturzbeben vom 19. November 1910, *Sitzungsber. mathem.-phys. Kl. Bayer. Akad. Wiss. (München)*, pp. 221–258.
- Giessberger, H. (1922), Die Erdbeben Bayerns. 1. Teil, *Abh. Bayer. Akad. Wiss. mathem.-naturwiss. Kl.*, 29, 3–72.
- GLA-Bayern (1998), *Geologie von Bayern. Geologische Karte von Bayern 1: 500 000 mit Erläuterungen und farbigen Beilagen*, Bayerisches Geologisches Landesamt, Munich.
- Glaser, S. (2004), Der Hochstaufen 1349, in *Münchner Höhlengeschichte II. 50 Jahre Verein für Höhlenkunde in München e.V.*, edited by G. Stautz, pp. 291–295, VHM, München.
- Grünthal, G. (2004), The history of historical earthquake research in Germany, *Ann. Geoph.*, 47(2/3), 631–643.
- GSETT-3 (1997), *Provisional GSE2.1 formats and protocols*, Group of Scientific Experts at the Conference on Disarmament, http://www.seismo.ethz.ch/autodrm/downloads/provisional_GSE2.1.pdf.
- Gümbel, C. W. (1889), Das Erdbeben vom 22. Februar 1889 in der Umgegend von Neuburg a.D., *Ber. Bayer. Akad. Wiss. (München)*.

- Gümbel, C. W. (1898), Über die in den letzten Jahren in Bayern wahrgenommenen Erdbeben, *Ber. Bayer. Akad. Wiss. (München)*, pp. 3–18.
- Günther, S. (1890), Münchener Erdbeben und Prodigienlitteratur in älterer Zeit, *Jahrb. Münch. Gesch.*, 4, 233–256.
- Günther, S., and J. Reindl (1903), Seismologische Untersuchungen, *Sitzungsber. mathem.-phys. Kl. Bayer. Akad. Wiss. (München)*, XXXIII(2), 631–671.
- Hainzl, S., and Y. Ogata (2005), Detecting fluid signals in seismicity data through statistical earthquake modeling, *J. Geophys. Res.*, 110(B9), B05S07, doi:10.1029/2004JB003247.
- Hainzl, S., T. Kraft, J. Wassermann, H. Igel, and E. Schmedes (2006), Evidence for rainfall-triggered earthquake activity, *Geophys. Res. Lett.*, 33, doi:10.1029/2006GL027642, in press.
- Hanka, W., and R. Kind (1994), The GEOFON Program, *Annali di Geofisica*, XXXVII(5), 1060–1065.
- Hanka, W., A. Heinloo, and K.-H. Jäckel (2000), Geofon real-time data distribution, *Orfeus Electronic Newsletter*, 2, 24.
- Hardebeck, J. L., and P. M. Shearer (2002), A new method for determining first-motion focal mechanisms, *Bull. Seism. Soc. Am.*, 92(6), 2264–2276, doi:10.1785/0120010200.
- Harjes, H. P. (1990), Design and siting of a new regional array in central Europe, *Bull. Seism. Soc. Am.*, 80, 1801–1817.
- Harris, R. (1998), Introduction to special section: Stress triggers, stress shadows, and implications for seismic hazard, *J. Geophys. Res.*, 103, 24,347–24,358, doi:10.1029/98JB01576.
- Heim, A. (1878), *Mechanismus der Gebirgsbildung*, Basel.
- Henrich, R., and H. Zankl (1981), Die Geologie des Hochstaufermassivs in den Nördlichen Kalkalpen, *Verh. Geol. Bundesanstalt, Wien*, 2, 31–57.
- Hill, P. (1977), A model for earthquake swarms, *J. Geophys. Res.*, 82, 1347–1352.

- Howells, L. (1974), The time for a significant change of pore pressure, *Eng. Geol.*, *8*, 135–138.
- Hubbert, M., and W. Rubey (1959), Role of fluid pressure in mechanics of overthrust faulting: I. Mechanics of fluid-filled porous solids and its application to overthrust faulting, *Geol. Soc. Am. Bull.*, *70*(2), 115–166.
- Humboldt, A. v. (1845–1861), *Kosmos I-V. Entwurf einer physischen Weltbeschreibung*, Stuttgart und Tübingen.
- Hunt, C. (2002), *TCP/IP Network Administration*, 3rd ed., O'Reilly & Associates, Inc., Sebastopol, Canada.
- Kennett, B. L. N., and E. R. Engdahl (1991), Traveltimes for global earthquake location and phase identification, *Geophys. J. Int.*, *105*, 429–465.
- King, G. C. P., R. S. Stein, and J. Lin (1994), Static stress changes and the triggering of earthquakes, *Bull. Seism. Soc. Am.*, *84*, 935–953.
- Kirch, O., and T. Dawson (2000), *Linux Network Administrator's Guide*, 2nd ed., O'Reilly.
- Kissling, E., W. Ellsworth, D. Eberhart-Phillips, and U. Kradolfer (1994), Initial reference models in local earthquake tomography, *J. Geophys. Res.*, *99*(B10), 19,635–19,646.
- Knett, J. (1899), Das Erzgebirgische Schwarmbeben zu Hartenberg vom 1. Jänner bis 5. Feber 1824., *Sitzungsber. Deutsche Naturwiss.-Med. Ver. Böhmen. Lotos Prag N. F.*, *19*, 167–191.
- Kodaira, S., T. Idaka, A. Kato, J. Park, T. Iwasak, and Y. Kaneda (2004), High pore fluid pressure may cause silent slip in the Nankai Trough, *Science*, *304*, 1295–1298.
- Koschyk, K. G. (1973), Seismische Untersuchungen der Erdstöße der Jahre 1926–1971 in Peißenberg, Ph.D. thesis, LMU Munich.
- Kraft, T., J. Wassermann, E. Schmedes, and H. Igel (2006a), Meteorological triggering of earthquake swarms at Mt. Hochstaufen, SE-Germany, *Tectonophysics*, *424*(3–4), 245–258, doi:10.1016/j.tecto.2006.03.044.
- Kraft, T., J. Wassermann, and H. Igel (2006b), High-precision relocation and focal mechanism of the 2002 rain-triggered earthquake swarms at Mt. Hochstaufen, SE-Germany, *Geophys. J. Int.*, doi:10.1111/i.1365-246X.2006.03171.x, in press.

- Kümpel, H.-J. (1991), Poroelasticity: Parameters reviewed, *Geophys. J. Int.*, *105*, 783–799.
- Kurz, J., T. Jahr, and G. Jentzsch (2003), Earthquake swarm examples and a look at the generation mechanism of the Vogtland/Western Bohemia earthquake swarms, *Phys. Earth Planet. Int.*, *142*, 75–88, doi: 10.1016/j.pepi.2003.12.007.
- Landau, L. D., and E. M. Lifschitz (1966), *Lehrbuch der theoretischen Physik*, vol. VI, Akademie-Verlag, Berlin.
- Lee, M., and L. W. Wolf (1998), Analysis of fluid pressure propagation in heterogeneous rocks: Implications for hydrologically-induced earthquakes, *Geophys. Res. Lett.*, *25*(13), 2329–2332.
- Lee, W. H. K., and J. C. Lahr (1975), Hypo71 (revised): A computer program for determining hypocenter, magnitude, and first motion of local earthquakes, *USGS open-file report*, *75-311*, 114.
- Lippmann, E. (1982), Umwandlung eines elektrodynamischen Seismometers in einen Beschleunigungs-Aufnehmer und Entwicklung eines Filters zur Simulation eines niederfrequenten Seismometers, Diploma Thesis, University of Munich.
- Lomax, A., J. Virieux, P. Volant, and C. Berge (2000), Probabilistic earthquake location in 3d and layered models: Introduction of a Metropolis-Gibbs method and comparison with linear locations, in *Advances in Seismic Event Location*, edited by C. Thurber and N. Rabinowitz, pp. 101–134, Kluwer, Amsterdam.
- Lutz, C. W. (1921), Erdbeben in Bayern 1908/20, *Abh. Bayer. Akad. Wiss. mathem.-naturwiss. Klasse*.
- LVG-Bayern (2000), Digital elevation model DGM 5 (10 m grid), Landesamts für Vermessung und Geoinformation, Bayern, www.geodaten.bayern.de, Nutzungserlaubnis vom 6.12.2000, AZ.: VM 3860 B - 4562.
- Manga, M., E. E. Brodsky, and M. Boone (2003), Response of streamflow to multiple earthquakes, *Geophys. Res. Lett.*, *30*, 1214, doi: 10.1029/2002GL016618.
- Matlab[®] (2005), *The language of technical computing*, The MathWorks, Inc., Natick, Massachusetts, USA.

- Medvedev, S. V., W. Spohnauer, and V. Karnik (1965), Seismic intensity scale version MSK 1964, *Akad. Nauk SSSR, Geofiz. Kom. (Moscow)*, p. 10.
- Menke, W. (1989), *Geophysical data analysis: Discrete inverse theory, International Geophysics Series*, vol. 45, Academic Press, New York, USA.
- Messerschmitt, J. (1907), Die Registrierungen der letzten großen Erdbebenkatastrophen auf der Erdbebenstation in München, *Mitteilungen der geographischen Gesellschaft in München, 197-235*.
- Miller, S. A., C. Collettini, L. Chiaraluce, M. Cocco, M. Barchi, and B. J. P. Kaus (2004), Aftershocks driven by a high-pressure CO₂ source at depth, *Nature*, *427*, 724–727.
- Mills, D. L. (1991), Internet time synchronization: The network time protocol, *IEEE Transactions on Communications*, *39*(10), 1482–1493.
- Mogi, K. (1963), Some discussions on aftershocks, foreshocks and earthquake swarms - the fracture of a semi infinite body caused by inner stress origin and its relation to the earthquake phenomena, *Bull. Earthquake Res. Int. Univ. Tokyo*, *41*, 615–658.
- Moore, E. H. (1920), On the reciprocal of the general algebraic matrix, *Bull. Amer. Math. Soc.*, *23*, 394–395.
- Moser, T. J., T. van Eck, and G. Nolet (1992), Hypocenter determination in strongly heterogeneous earth models using the shortest path method, *J. Geophys. Res.*, *97*, 6563–6572.
- Muco, B. (1995), The seasonality of Albanian earthquakes and cross-correlation with rainfall, *Phys. Earth Planet. Int.*, *88*, 285–291.
- Muco, B. (1999), Statistical investigation on possible seasonality of seismic activity and rainfall-induced earthquakes in Balkan area, *Phys. Earth Planet. Int.*, *114*, 119–127.
- Munich Re Group (2003), *topics: Annual review: Natural catastrophes 2002*, vol. 10th year, chap. The summer floods in Europe - A millennium flood?, pp. 17–25, Münchener Rückversicherungsgesellschaft, Munich, Germany.
- Neuzil, C. (2003), Hydromechanical coupling in geologic processes, *Hydrogeol. J.*, *11*, 41–83.

- NMEA (2002), *National Marine Electronics Association (NMEA) 0183 Standard*, National Marine Electronics Association, www.nmea.org, Severna Park, Mariland, USA.
- Nöthen, M. (1981), Untersuchung der lokalen seismischen Aktivität im Raum Bad Reichenhall, Diploma thesis, University of Munich.
- Nur, A., and J. Booker (1972), Aftershocks caused by pore fluid flow?, *Science*, *175*, 885–887.
- Ogata, Y. (1998), Space-time point-process models for earthquake occurrences, *Ann. Inst. Statist. Math*, *50*, 379–402.
- Parotidis, M., E. Rothert, and S. A. Shapiro (2003), Pore-pressure diffusion: A possible triggering mechanism for the earthquake swarm 2000 in Vogtland/NW-Bohemia, Cental Europe, *Geophys. Res. Lett.*, *30*(20), 2075, doi:10.1029/2003GL018110.
- Parotidis, M., S. A. Shapiro, and E. Rothert (2005), Evidence for triggering of the Vogtland swarms 2000 by pore pressure diffusion, *J. Geophys. Res.*, *110*(B9), 2075, doi:10.1029/2004JB003267.
- Penrose, R. (1955), A generalized inverse of matrices, *Proc. Cambridge Philos. Soc.*, *51*, 406–413.
- PHASE Research project (2005), Phase research project, annual report (2005), Freie Universität Berlin (<http://phase.geophysik.fu-berlin.de/index.html>).
- Podvin, P., and I. Lecomte (1991), Finite difference computations of traveltimes in very contrasted velocity models: a massively parallel approach and its associated tools, *Geophys. J. Int.*, *105*, 271–284.
- Poupinet, G., V. L. Ellsworth, and J. Frechet (1984), Monitoring velocity variations in the crust using earthquake doublets: An application to the Calaveras fault, California, *J. Geophys. Res.*, *89*, 5719–5732.
- Prejean, S. G., P. D. Hill, E. E. Brodsky, S. E. Hough, M. J. S. Johnston, S. D. Malone, D. H. Oppenheimer, A. M. Pitt, and K. D. Richards-Dinger (2004), Remotely triggered seismicity on the United States west coast following the Mw 7.9 Denali Fault earthquake, *Bull. Seism. Soc. Am.*, *94*(6B), 348–359.
- Pujol, J. (2003), *Elastic Wave Propagation and Generation in Seismology*, Cambridge University Press.

- Quanterra (2002), *COMSERV*, Quanterra, Inc., Harvard, Massachusetts, USA, (<http://www.kinometrics.com>), doi:<http://www.kinometrics.com>.
- Reindl, J. (1902-1903), Die Erdbeben der geschichtlichen Zeit im Königreiche Bayern, *Die Erdbebenwarte*, 2.
- Reindl, J. (1903), Beiträge zur Erdbebenkunde von Bayern., *Sitzungsber. mathem.-phys. Kl. Bayer. Akad. Wiss. (München)*, 33(1), 171–200.
- Reindl, J. (1905a), Ergänzungen und Nachträge zu v. Gübels Erdbebenkatalog, *Sitzungsber. math.-phys. Kl. Bayer. Akad. Wiss. (München)*, 35(1), 31–68.
- Reindl, J. (1905b), Die Erdbeben Nordbayerns, *Abh. Naturhist. Ges. (Nürnberg)*, 15(3), 251–294.
- Rietbrock, A., and F. Scherbaum (1998), The GIANT analysis system (Graphical Interactive Aftershock Network Toolbox), *Seismol. Res. Lett.*, 69, 40–45.
- Roeloffs, E. A. (1988), Fault stability changes induced beneath a reservoir with cyclic variations in water level, *J. Geophys. Res.*, 93(12), 2107–2124, doi:10.1029/88JB01272.
- Roeloffs, E. A., M. Sneed, D. L. Galloway, M. L. Sorey, C. D. Farrar, J. F. Howle, and J. Hughes (2003), Water-level changes induced by local and distant earthquakes at Long Valley caldera, California, *J. Volcanol. Geoth. Res.*, 127, 269–303, doi:10.1016/S0377-0273(03)00173-2.
- Roth, P., N. Pavoni, and N. Deichmann (1992), Seismotectonic of the eastern Swiss Alps and evidence for precipitation-induced variations of seismic activity, *Tectonophysics*, 207, 183–197.
- Rothert, E., and J. R. R. Ritter (2000), Small-scale heterogeneities below the Gräfenberg array, Germany from seismic wavefield fluctuations of Hindu Kush events, *Geophys. J. Int.*, 140, 140, 175–184.
- Rothert, E., and S. A. Shapiro (2003), Microseismic monitoring of borehole fluid injections: Data modeling and inversion for hydraulic properties of rocks, *Geophys.*, 68(2), 685–689, doi:10.1190/1.1567239.
- Rowe, C. A., R. C. Aster, W. S. Phillips, R. H. Jones, B. Borchers, and M. C. Fehler (2002), Using automated, high-precision repicking to improve delineation of microseismic structures at the Soultz geothermal reservoir, *Pure Appl. Geophys.*, 159, 563–596.

- Rudnicki, J. W. (1986), 5, *Mechanics of Materials*, 5, 383–393.
- Saar, M. O., and M. Manga (2003), Seismicity induced by seasonal groundwater recharge at Mt. Hood, Oregon, *Earth Planet. Sci. Lett.*, 214, 605–618.
- Schmedes, E. (1979), Die seismische Aktivität im Raum Bad Reichenhall, *Geol. Jahrb.*, C22, 91–102.
- Scholz, C. H. (1994), *The Mechanics of Earthquakes and Faulting*, Cambridge University Press.
- Scholz, C. H. (1998), Earthquakes and friction laws, *Nature*, 391, 37–42.
- Schwarzmann, A. (1996), Untersuchungen der seismischen Aktivität im Raum Bad Reichenhall, Diploma Thesis, University of Munich.
- Schwarzmann, A., F. Scherbaum, and E. Schmedes (2001), *Erdbeben in Deutschland 1995. Berichte der deutschen seismologischen Observatorien mit einem Katalog wichtiger Weltbeben*, chap. Alpen - der Erdbebenschwarm im Raum Bad Reichenhall, pp. 29–36, Bundesanstalt für Geowissenschaften und Rohstoffe.
- Schweitzer, J., and W. H. K. Lee (2003), *International Handbook of Earthquake and Engineering Seismology*, chap. Old seismic bulletins to 1920: A collective heritage from early seismologists, pp. 1665–1723, Academic Press.
- SED (2002), ECOS - earthquake catalog of Switzerland. ECOS report to PEGASOS, Swiss Seismological Service, Zurich, <http://histserver.ethz.ch/download/ECOS.pdf>.
- Segall, P. (1985), Stress and subsidence resulting from subsurface fluid withdrawal in the epicentral region of the 1983 Coalinga earthquake, *J. Geophys. Res.*, 90(9), 6801–6816, doi: 10.1029/0JGREA0000900000B8006801000001.
- Seidl, D., and H. Aichele (1997), *Zur Geschichte der Geophysik in Deutschland, Jubiläumsschrift "Deutsche Geophysikalische Gesellschaft 1922-1997"*, chap. Die Geschichte des Seismologischen Zentralobservatoriums Gräfenberg (SZGRF), pp. 101–107, Deutsche Geophysikalische Gesellschaft.
- Shapiro, S. A., E. Huenges, and G. Borm (1997), Estimating the crust permeability from fluid-injection-induced seismic emission at the KTB site, *Geophys. J. Int.*, 131, F15–F18.

- Shapiro, S. A., R. Patzig, and E. Rothert (2003), Triggering of seismicity by pore-pressure perturbations: Permeability-related signatures of the phenomenon, *Pure Appl. Geophys.*, *160*, 1051–1066.
- Sleep, N., and M. L. Blanpied (1992), Creep, compaction and the weak rheology of major faults, *Nature*, *359*, 687–692.
- Snoke, J. A. (2003), *International Handbook of Earthquake and Engineering Seismology*, chap. FOCMEC: FOcal MEChanism determinations, pp. 29–30, Academic Press, San Diego.
- Spicak, A. (2000), Earthquake swarms and accompanying phenomena in intraplate regions: A review, *Stud. Geophys. Geod.*, *44*, 89–106.
- Stammler, K. (1993), SeismichHandler – programmable multichannel data handler for interactive and automatic processing of seismological analysis, *Computers & Geosciences*, *19*(2), 135–140.
- Stein, R. S. (1999), The role of stress transfer in earthquake occurrence, *Nature*, *402*, 605–609.
- Sykes, L. (1970), Earthquake swarms and sea-floor spreading, *J. Geophys. Res.*, *75*, 6598–6611.
- Talwani, P. (1997), On the nature of reservoir-induced seismicity, *Pure Appl. Geophys.*, *150*, 473–492.
- Talwani, P. (2000), Seismogenic properties of the crust inferred from recent studies of reservoir-induced seismicity - Application to Koyna, *Curr. Sci. India.*, *79*(9), 1327–1333.
- Tarantola, A. (2004), *Inverse problem theory and methods for model parameter estimation*, SIAM, Philadelphia.
- Tarantola, A., and B. Valette (1982), Generalized nonlinear inverse problems solved using the least squares criterion, *Rev. Geophys. Space Phys.*, *20*, 219–232.
- Terzaghi, K. (1923), Die Berechnung der Durchlässigkeitziffer des Tones aus dem Verlauf der hydrodynamischen Spannungserscheinungen, *Akad. Wiss. Wien, Sitzungsber. mathem.-naturwiss. Kl., Part IIa*, *132*(3/4), 125–138.
- Tollmann, A. (1976), *Der Bau der Nördlichen Kalkalpen. Orogene Stellung und regionale Tektonik*, vol. 3, 449+7 pp., Deuticke, Wien.

- Tolstoy, M., F. L. Vernon, Orcutt, J. A., and F. K. Wyatt (2002), The breathing of the seafloor: Tidal correlations of seismicity on Axial volcano, *Geology*, *30*, 503–506.
- Torvalds, L. (1997), Linux: A portable operating system, C-1997-12, University of Helsinki, Department of Computer Science, Helsinki, Finland.
- Ventura, G., and G. Vilaro (1999), Seismic-based estimate of hydraulic parameters at Vesuvius volcano, *Geophys. Res. Lett.*, *26*, 887–890, doi: 10.1029/1999GL900140.
- Volger, G. H. O. (1857–1858), *Untersuchungen über das Phänomen der Erdbeben in der Schweiz I-III*, Gotha: Perthes.
- Waldhauser, F., and W. L. Ellsworth (2000), A double-difference earthquake location algorithm: Method and application to the northern Hayward fault, California, *Bull. Seism. Soc. Am.*, *90*(6), 1353–1368.
- Wang, H. F. (2000), *Theory of linear poroelasticity with applications to geomechanics and hydrogeology*, Princeton University Press.
- Weede, M. (2002), Die Geologie des Hochstaufen unter besonderer Berücksichtigung der Massenbewegungen, Diploma Thesis, Technical University of Munich.
- Wessel, P., and W. H. F. Smith (1991), Free software helps map and display data, *EOS Trans. AGU*, *72*, 441.
- Wielandt, E. (1997), *Zur Geschichte der Geophysik in Deutschland, Jubiläumsschrift "Deutsche Geophysikalische Gesellschaft 1922-1997"*, chap. Hunder Jahre Erdbebenforschung in Stuttgart, pp. 134–140, Deutsche Geophysikalische Gesellschaft.
- Wielandt, E., and G. Streckeisen (1982), The leaf-spring seismometer: design and performance, *Bull. Seism. Soc. Am.*, *72*(6), 2349–2367.
- Will, M. (1975), Refraktions-Seismik im Nordteil der Ostalpen zwischen Salzach und Inn, 1970-1974; Messungen und deren Interpretation, Ph.D. thesis, LMU Munich.
- Wittlinger, G., G. Herquel, and T. Nakache (1993), Earthquake location in strongly heterogeneous media, *Geophys. J. Int.*, *115*, 759–777.

- Wolf, L., C. Rowe, and R. Horner (1997), Periodic seismicity near Mt. Ogden on the Alaska-British Columbia border: A case for hydrologically triggered earthquakes?, *Bull. Seism. Soc. Am.*, *87*(6), 1473–1483.
- Wolfe, C. J. (2002), On the mathematics of using difference operators to relocate earthquakes, *Bull. Seism. Soc. Am.*, *92*(8), 2879–2892.
- Yamashita, T. (1999), Pore creation due to fault slip in a fluid-permeated fault zone and its effects on seismicity: Generation mechanism of earthquake swarms, *Pure Appl. Geophys.*, *155*, 625–647.
- Ylonen, T. (1995), Openssh, <http://www.openssh.com>.
- Zankl, H., and O. Schell (1979), Der geologische Bau des Talkessels von Bad Reichenhall (Nördliche Kalkalpen), *Geol. Jahrb.*, *22*.
- Zhang, H., and C. H. Thurber (2003), Double-difference tomography: Method and its application to the Hayward Fault, California, *Bull. Seism. Soc. Am.*, *93*(5), 1875–1889.
- Zoback, M. D., and H.-P. Harjes (1997), Injection-induced earthquakes and crustal stress at 9 km depth at the KTB deep drilling site, Germany, *J. Geophys. Res.*, *102*, 18,477–18,492.

Appendix A

Seismological station

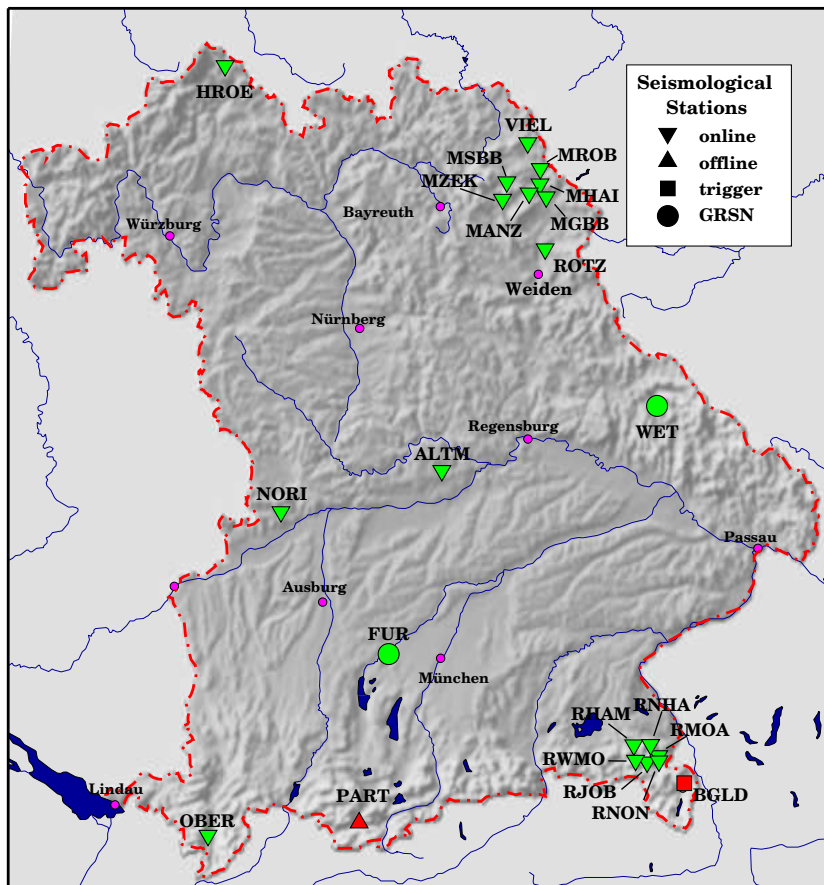


Figure A.1: Map of the new Bavarian Seismological Network (BayernNetz). Station locations are indicated by symbols explained in the figure. A list of all stations can be found in Table A.1. Individual station sheets with geological maps are collected in Appendix A.

CODE	NAME	COORDINATES	START	SEISMOMETER	LOGGER	SAMPLING	PHONE
ALL-BAVARIAN NETWORK							
HROE	<i>Hohe Rhön</i>	50.537 10.157 569	10.12.02	LE-3Dlite	LE-M24	200Hz	ISDN
PART	<i>Partenkirchen</i>	47.496 11.116 760	01.01.01	LE-3Dlite	LE-M24	200Hz	offline
OBER	<i>Oberstdorf</i>	47.407 10.293 1000	18.03.02	LE-3Dlite	LE-M24	200Hz	ISDN
NORI	<i>Nördlinger Ries</i>	48.720 10.624 480	10.06.03	LE-3Dlite	LE-M24	200Hz	ISDN
ALTM	<i>Altmühltal (GRC1)</i>	48.995 11.520 430	20.06.01	LE-3Dlite	LE-M24	200Hz	ISDN
BGLD	<i>Berchtesgaden</i>	47.652 13.012 930	01.10.99	LE-3Dlite	MARS88	80Hz	Modem
ROTZ	<i>Rotzenmühle</i>	49.768 12.208 430	22.07.99	STS-2	LE-M24	200Hz	ISDN
VIEL	<i>Selb/Vielitz</i>	50.186 12.103 670	02.06.03	LE-3Dlite	LE-M24	200Hz	ISDN
BGLD	<i>Berchtesgadener Land</i>	47.652 13.012 930	01.01.92	STS-2	Mars88	125Hz	ISDN
FUR	<i>Fürstfeldbruck</i>	48.163 11.275 570	28.02.01	STS-2	Quanterra	80Hz	ISDN
WET	<i>Wetzell</i>	49.144 12.8782 613	01.01.92	STS-2	Quanterra	80Hz	ISDN
SUBNET MARKREDWITZ							
MHAI	<i>Haid</i>	50.023 12.176 550	13.03.01	LE-3Dlite	LE-M24	200Hz	ISDN
MGBB	<i>Großbüchelberg</i>	49.972 12.215 650	12.03.01	LE-3Dlite	LE-M24	200Hz	ISDN
MROB	<i>Rosenbühl</i>	50.083 12.179 570	08.10.01	LE-3Dlite	LE-M24	200Hz	ISDN
MSBB	<i>Schöbrunner Berg</i>	50.031 11.973 622	10.04.01	LE-3Dlite	LE-M24	200Hz	ISDN
MZEK	<i>Zeckenberg</i>	49.963 11.947 627	24.04.01	LE-3Dlite	LE-M24	200Hz	ISDN
MANZ	<i>Manzenberg</i>	49.986 12.108 638	17.11.03	STS-2	LE-M24	200Hz	ISDN
SUBNET BAD REICHENHALL							
RJOB	<i>Jochberg</i>	47.737 12.796 860	15.05.01	LE-3Dlite	LE-M24	200Hz	ISDN
RHAM	<i>Hammer</i>	47.804 12.720 799	09.04.01	LE-3Dlite	LE-M24	200Hz	ISDN
RNHA	<i>Neuhaus</i>	47.806 12.819 855	22.05.01	LE-3Dlite	LE-M24	200Hz	ISDN
RWMO	<i>Wildenmoos</i>	47.744 12.730 763	09.04.01	LE-3Dlite	LE-M24	200Hz	ISDN
RMOA	<i>Moar-Alm</i>	47.762 12.864 815	24.08.01	LE-3Dlite	LE-M24	200Hz	ISDN
RNON	<i>Nonn</i>	47.740 12.867 555	21.01.04	LE-3Dlite	LE-M24	200Hz	ISDN

Table A.1: Station parameters of the Bavarian seismological Network. Station code, station name, station coordinates, seismometer type, data logger type, sampling rate, and telephone number are given.

RMOA

Subnetwork Bad Reichenhall
Moar-Alm



Location:

lon: 12.864478 lat: 47.761675 alt: 815m

Mountain cabin, north of Mt. Hochstaufen

Underground: talus cone

Hydroelectric power supply, weather station attached

Seismometer: LE3Dlite

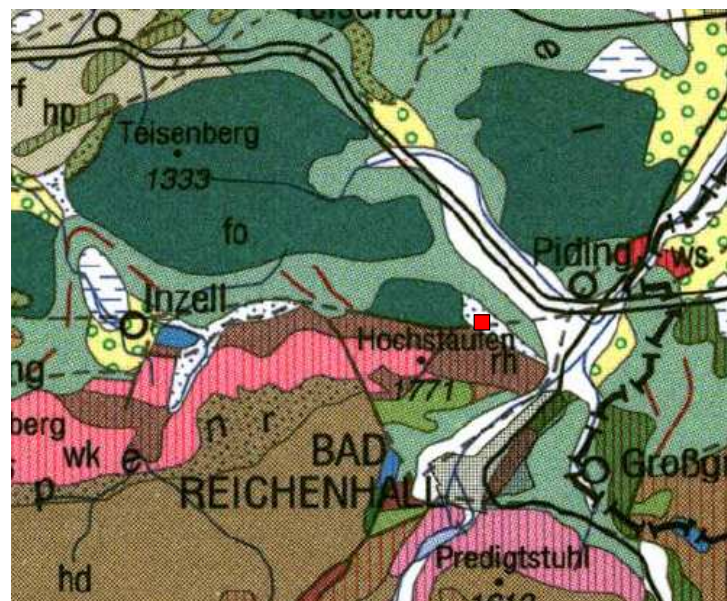
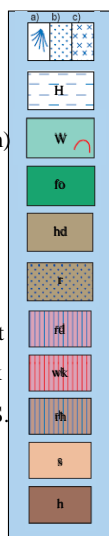
Concrete casing outside cabin, distance 15m.

Start: Aug. 24, 2001

Telephone: 08651 / 602112

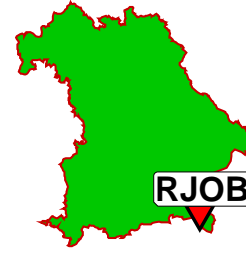
IP number: 192.168.20.141

talus cone
peat
moraine (wrüm)
Flysch
Hauptdolomit
Raibler S.
Ramsadolomit
Wettersteinkalk
Reichenhaller S.
Werfener S.
Haselgebirge



RJOB

Subnetwork Bad Reichenhall
Jochberg



Location:

lon: 12.795728 lat: 47.737192 alt: 860m

Privat house, southwest of Mt. Hochstaufen

Underground: Limestone, Raibler Schichten

Weather station attached

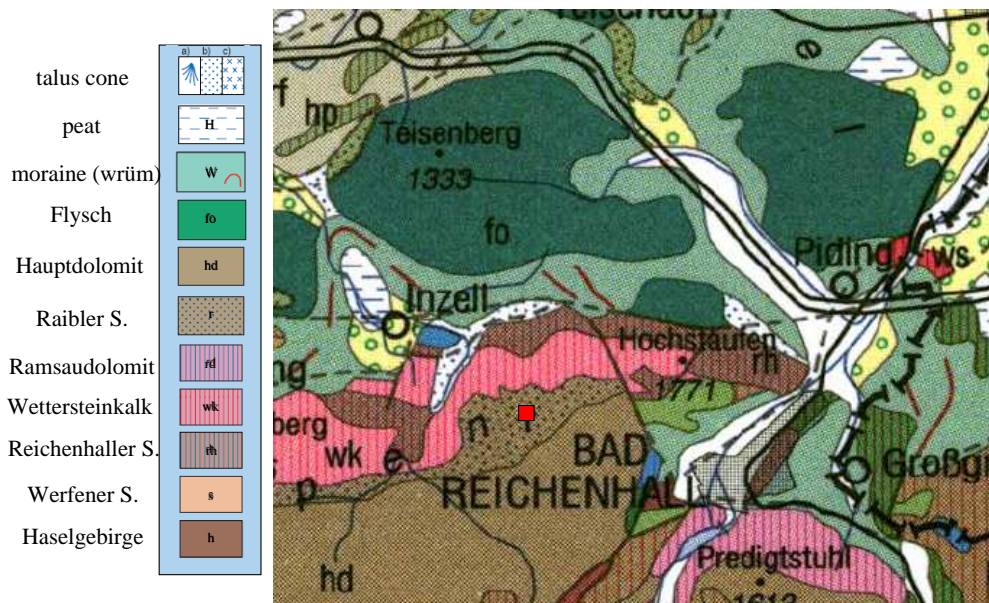
Seismometer: LE3Dlite

Concrete foundation on limestone, in garage

Start: May 15, 2001

Telephone: 08665 / 928127

IP number: 192.168.20.150



RNON

Subnetwork Bad Reichenhall
Bad Reichenhall – Nonn



Location:

lon: 12.867629 lat: 47.740509 alt: 555m

Closed water reservoir, south of Mt. Hochstaufen

Underground: moraine, Würm ice age

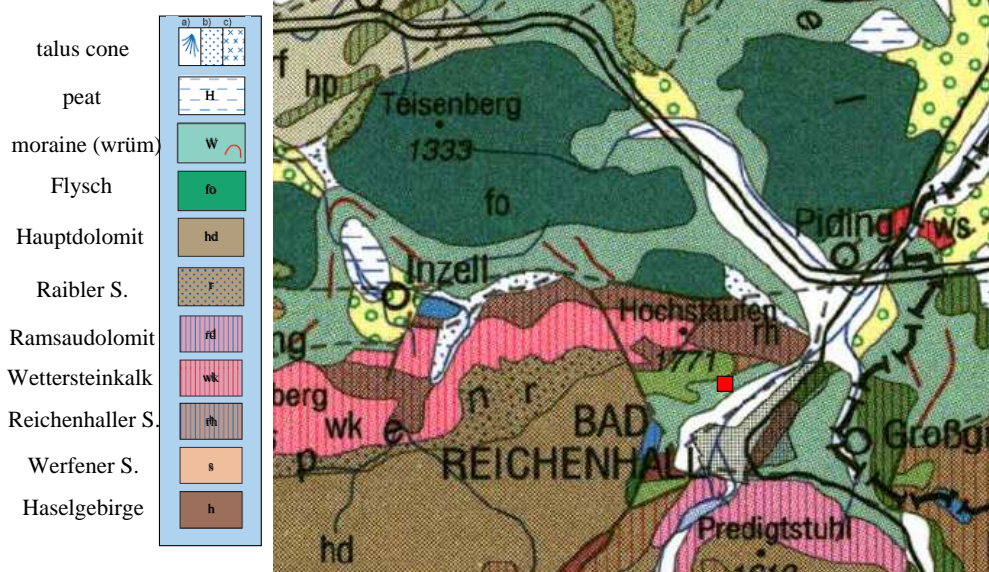
Weather station attached

Seismometer: LE3Dlite
concrete foundation, 2m below surface

Start: Jan. 21, 2004

Telephone: 08656 / 983592

IP number: 192.168.20.152



RWMO

Subnetwork Bad Reichenhall
Wildenmoos



Location:

lon: 12.729892 lat: 47.744187 alt: 763m

Transformer house, west of Mt. Hochstaufen

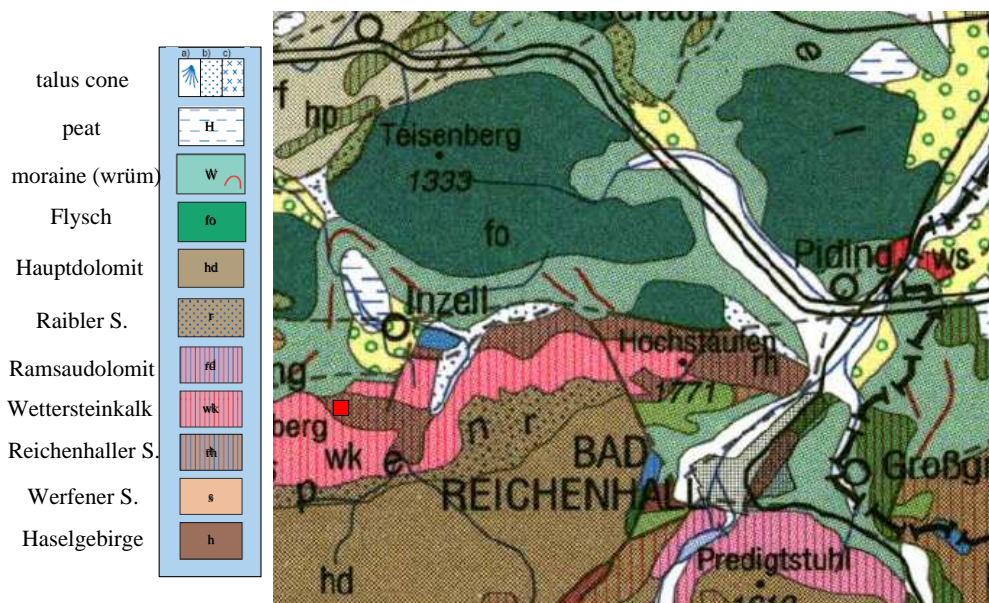
Underground: Reichenhaller Schichten

Seismometer: LE3Dlite
concrete foundation, 2m below surface

Start: Apr. 09, 2001

Telephone: 08665 / 928134

IP number: 192.168.20.145



RHAM

Subnetwork Bad Reichenhall
Hammer



Location:

lon: 12.720285 lat: 47.803969 alt: 799m

Water reservoir, 10km northwest of Mt. Hochstaufen

Underground: Flysch

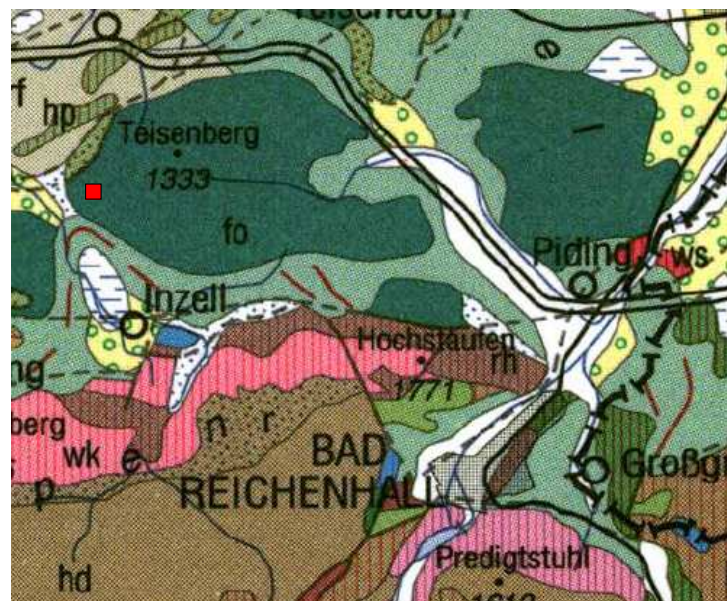
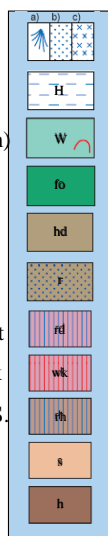
Seismometer: LE3Dlite
Concrete foundation, 6m below surface

Start: Apr. 9, 2001

Telephone: 08662 / 667247

IP number: 192.168.20.144

talus cone
peat
moraine (wrüm)
Flysch
Hauptdolomit
Raibler S.
Ramsadolomit
Wettersteinkalk
Reichenhaller S.
Werfener S.
Haselgebirge



RNHA

Subnetwork Bad Reichenhall
Neuhaus



Location:

lon: 12.818851 lat: 47.805738 alt: 855m

Water reservoir, north of Mt. Hochstaufen

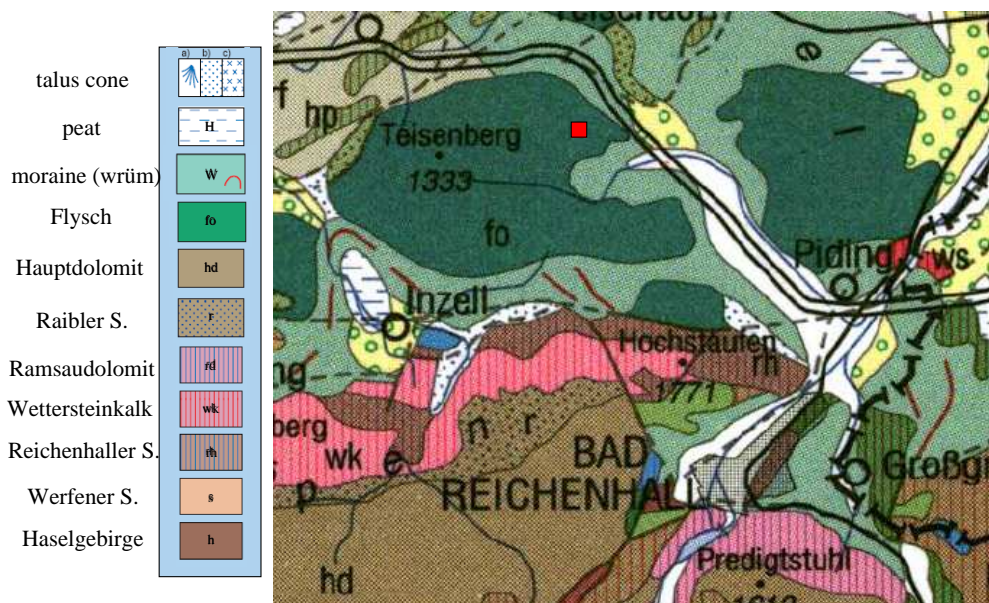
Underground: Flysch

Seismometer: LE3Dlite
concrete foundation, 4m below surface

Start: May 22, 2001

Telephone: 08665 / 928134

IP number: 192.168.20.152



MANZ

Subnetwork Marktredwitz
Manzenberg



Location:

lon: 12.10832 lat: 49.98623 alt: 638m

Water reservoir, south of Marktredwitz

Underground: Cambrian phyllite

Seismometer: STS-2

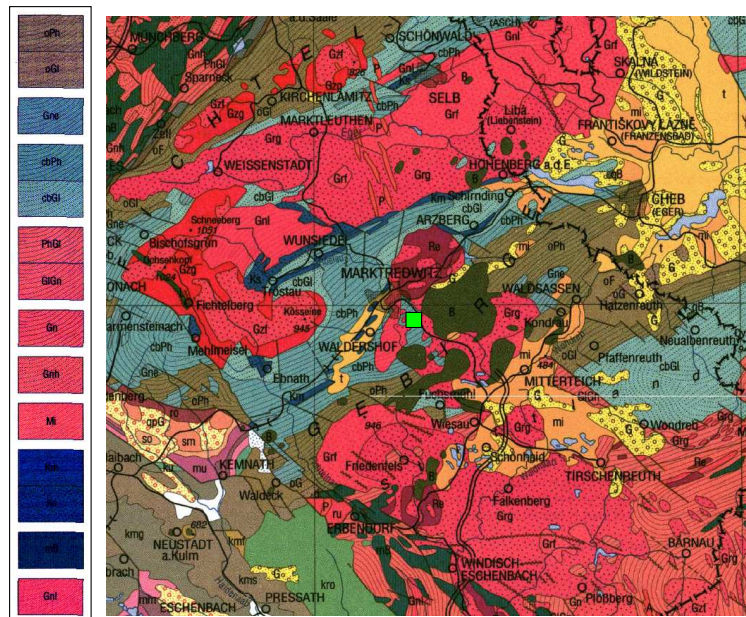
Concrete foundation, 6m below surface

Start: Nov. 17, 2003

Telephone: 09231 / 667934

IP number: 192.168.20.177

Frauenbach phyllite
Frauenbach mica slate
Epigneiss
Cambrian phyllite
Cambrian mica slate
phyllite → mica slate
mica slate → gneiss
gneiss + graphite
Hornblende gneiss
micmatic gneiss
marble
skarn (Kalksilikatfels)
metabasit
leucocratic gneiss



MZEK

Subnetwork Marktredwitz
Zeckenberg



Location:

lon: 11.947431 lat: 49.962605 alt: 627m

Water reservoir, southwest of Marktredwitz

Underground: Granit

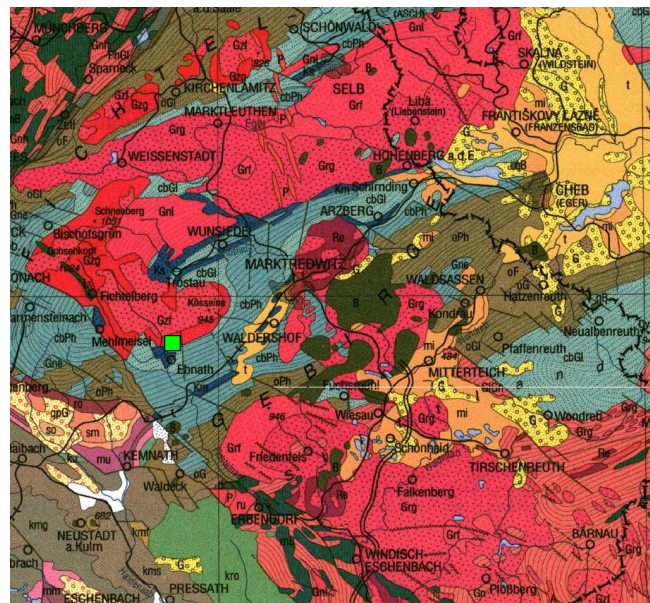
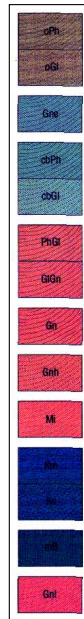
Seismometer: LE3Dlite
Concrete foundation, 6m below surface

Start: Apr. 24, 2001

Telephone: 09234 / 980633

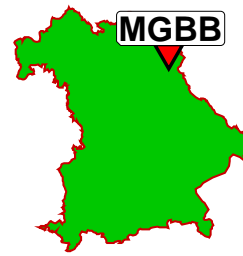
IP number: 192.168.20.142

Frauenbach phyllite
Frauenbach mica slate
Epigneiss
Cambrian phyllite
Cambrian mica slate
phyllite -> mica slate
mica slate -> gneiss
gneiss + graphite
Hornblende gneiss
micmatic gneiss
marble
skarn (Kalksilikatfels)
metabasit
leucocratic gneiss



MGBB

Subnetwork Marktredwitz
Großbüchelberg



Location:

lon: 12.214983 lat: 49.971972 alt: 650m

Water reservoir, southeast of Marktredwitz

Underground: Basalt

Seismometer: LE3Dlite

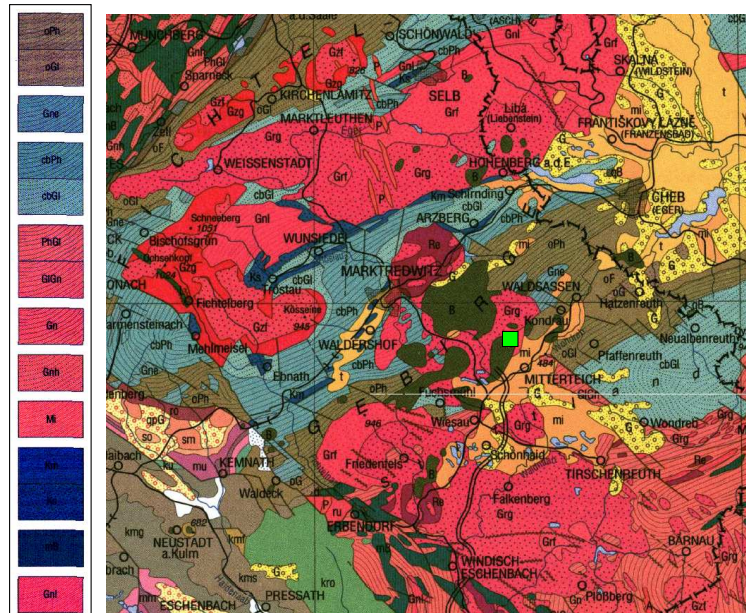
Concrete foundation, 6m below surface

Start: Mar. 12, 2001

Telephone: 09633 / 918644

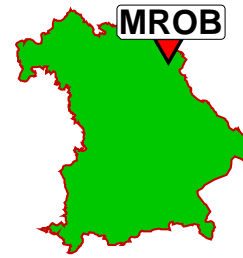
IP number: 192.168.20.148

Frauenbach phyllite
Frauenbach mica slate
Epigneis
Cambrian phyllite
Cambrian mica slate
phyllite → mica slate
mica slate → gneiss
gneiss + graphite
Hornblende gneiss
micmatic gneiss
marble
skarn (Kalksilikatfels)
metabasit
leucocratic gneiss



MROB

Subnetwork Marktredwitz
Rosenbühl



Location:

lon: 12.178602 lat: 50.083159 alt: 570m
water reservoir, northeast of Marktredwitz.

Underground: Basalt

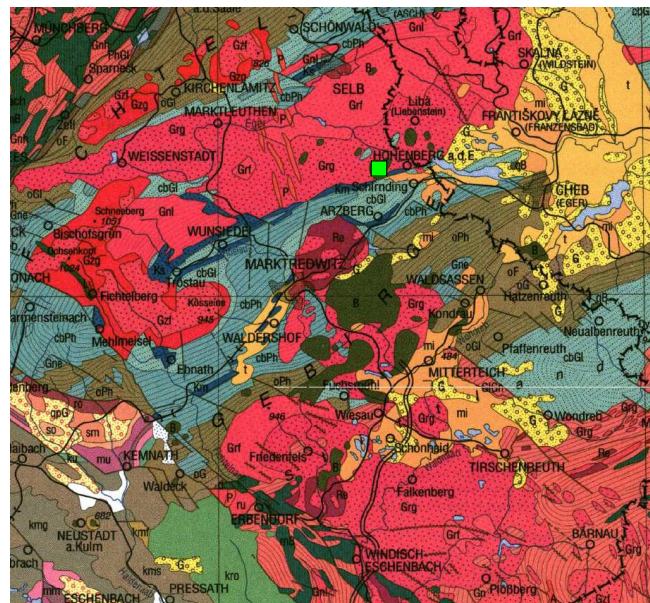
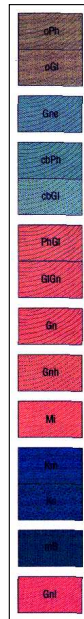
Seismometer: LE3Dlite
concrete foundation, 7m below surface

Start: Oct. 8, 2001

Telephone: 09233 / 716934

IP number: 192.168.20.151

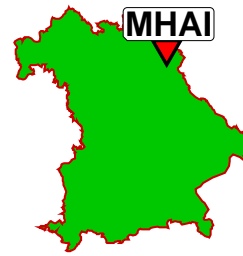
Frauenbach phyllite
Frauenbach mica slate
Epigneiss
Cambrian phyllite
Cambrian mica slate
phyllite -> mica slate
mica slate -> gneiss
gneiss + graphite
Hornblende gneiss
micmatic gneiss
marble
skarn (Kalksilikatfels)
metabasit
leucocratic gneiss



MHAI

Subnetwork Marktredwitz

Arzberg – Haid



Location:

lon: 12.176201 lat: 50.022532 alt: 550m

Water reservoir, east of Marktredwitz

Underground: Basalt

Seismometer: LE3Dlite

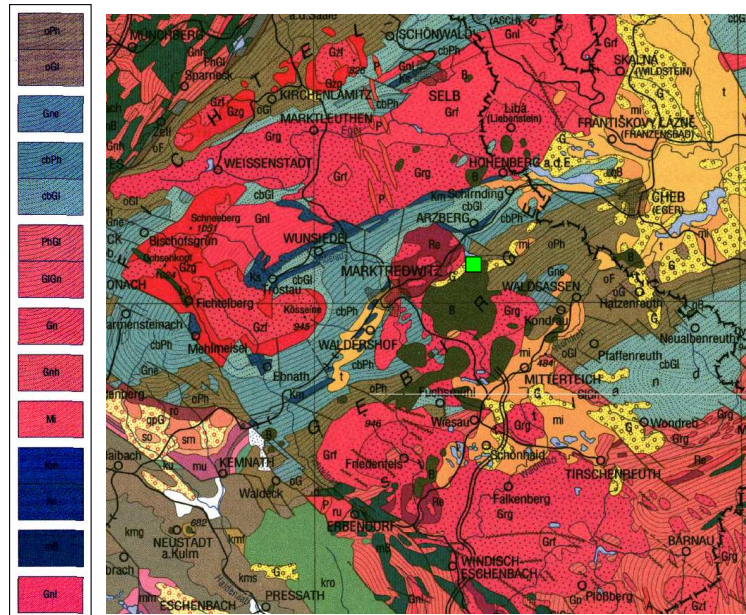
Concrete foundation, 5m below surface

Start: Mar. 13, 2001

Telephone: 09233 / 716926

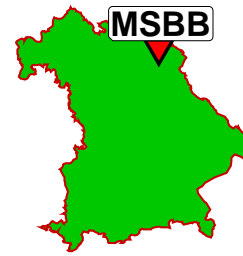
IP number: 192.168.20.140

Frauenbach phyllite
 Frauenbach mica slate
 Epigneiss
 Cambrian phyllite
 Cambrian mica slate
 phyllite → mica slate
 mica slate → gneiss
 gneiss + graphite
 Hornblende gneiss
 micmatic gneiss
 marble
 skarn (Kalksilikatfels)
 metabasit
 leucocratic gneiss



MSBB

Subnetwork Marktredwitz
Schönbrunner Berg



Location:

lon: 11.972784 lat: 50.031436 alt: 622m

Water reservoir, northwest on Marktredwitz

Underground: Skarn (Kalksilikatfels)

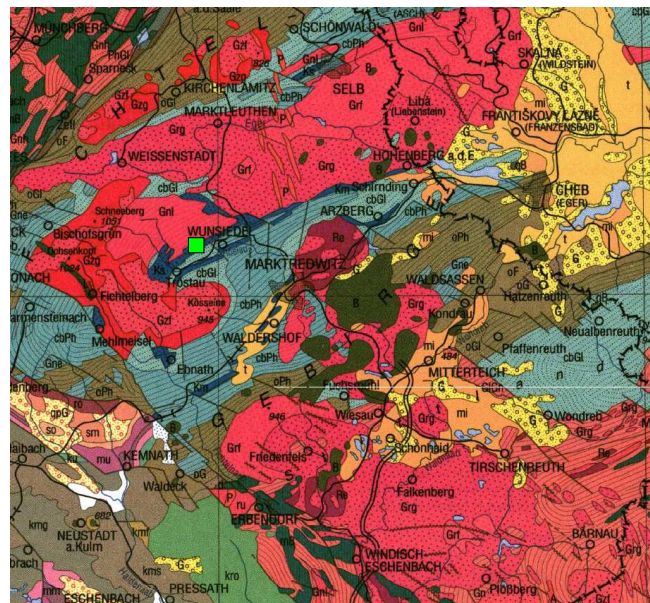
Seismometer: LE3Dlite
Concrete foundation, 4m below surface

Start: Apr. 10, 2001

Telephone: 09231/667934

IP number: 192.168.20.144

Frauenbach phyllite
Frauenbach mica slate
Epigneiss
Cambrian phyllite
Cambrian mica slate
phyllite -> mica slate
mica slate -> gneiss
gneiss + graphite
Hornblende gneiss
micmatic gneiss
marble
skarn (Kalksilikatfels)
metabasit
leucocratic gneiss



HROE

Main network Bavaria
Hohe Rhön



Location:

lon: 10.157351 lat: 50.536598 alt: 569m

Water reservoir, north of Fladungen

Underground: Gipskeuper

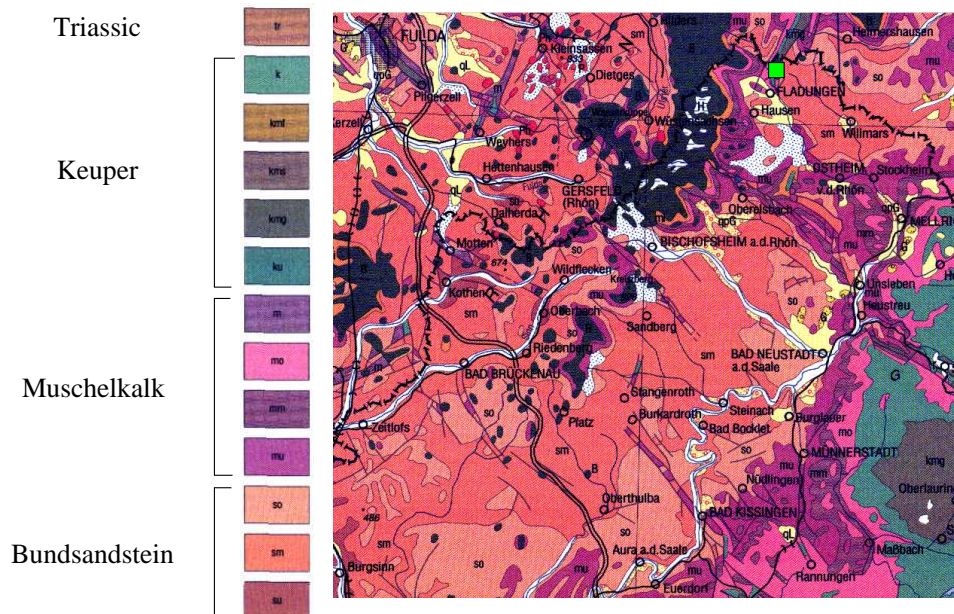
Seismometer: LE3Dlite

Concrete foundation, 7m below surface

Start: Dec. 10, 2001

Telephone: 09778 / 748693

IP number: 192.168.20.172



VIEL

Main network Bavaria
Selb – Vielitz



Location:

lon: 12.102784 lat: 50.185644 alt: 670m

Water reservoir, north of Selb

Underground: leucocratic gneiss

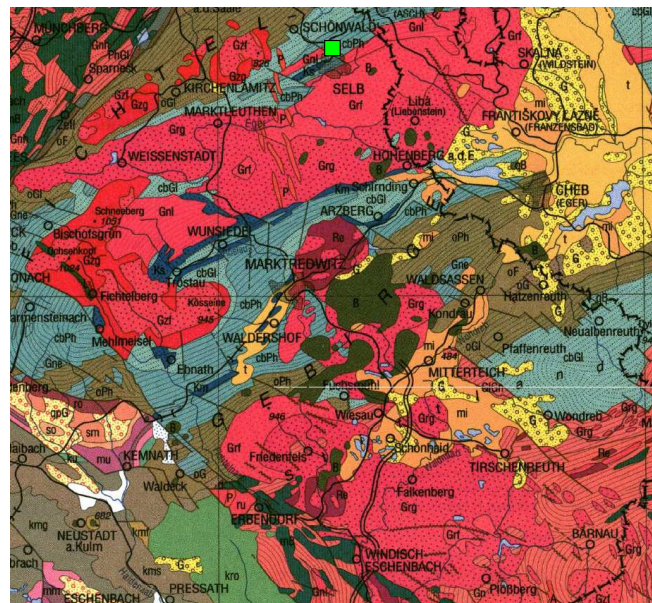
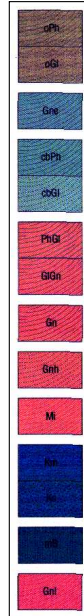
Seismometer: LE3Dlite
Concrete foundation, 4m below surface

Start: Jun. 2, 2003

Telephone: 09287/870687

IP number: 192.168.20.174

Frauenbach phyllite
Frauenbach mica slate
Epigneiss
Cambrian phyllite
Cambrian mica slate
phyllite -> mica slate
mica slate -> gneiss
gneiss + graphite
Hornblende gneiss
micmatic gneiss
marble
skarn (Kalksilikatfels)
metabasit
leucocratic gneiss



ROTZ

Main network Bavaria
Rotzenmühle



Location:

lon: 12.207006 lat: 49.766886 alt: 430m

Closed open pit mine, southeast of Windischeschenbach

Underground: Granit

Seismometer: STS-2

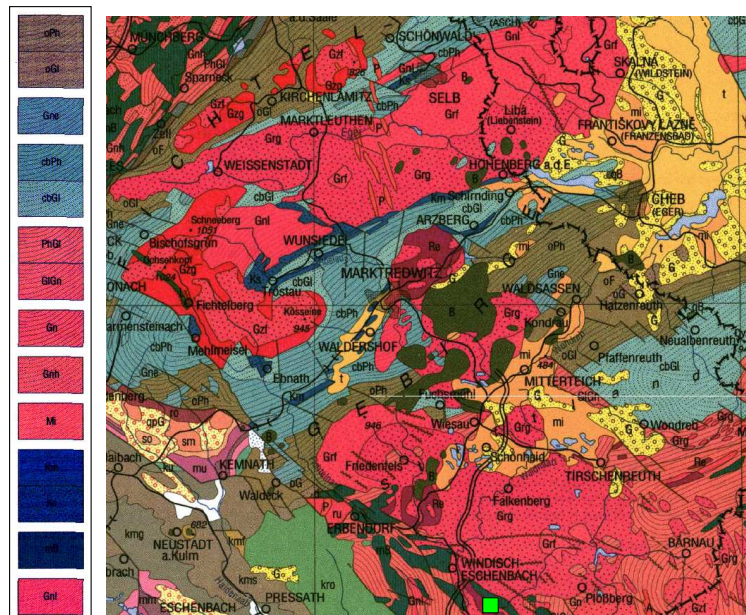
Concrete foundation, surface level

Start: Jun. 2, 2003

Telephone: 09602 / 3685

IP number: 192.168.20.175

Frauenbach phyllite
Frauenbach mica slate
Epigneiss
Cambrian phyllite
Cambrian mica slate
phyllite -> mica slate
mica slate -> gneiss
gneiss + graphite
Hornblende gneiss
micmatic gneiss
marble
skarn (Kalksilikatfels)
metabasit
leucocratic gneiss



WET

Subnetwork Marktredwitz
Wetzell



Location:

lon: 12.8782 lat: 49.1440 alt: 613m

Concrete bunker, west of Wetzell

Underground: Gneiss with graphite inclusions

GRSN station, radio telescope station (VLBI)

Seismometer: STS-2

Concrete foundation, 4m below surface

Start: Jan. 1, 1992

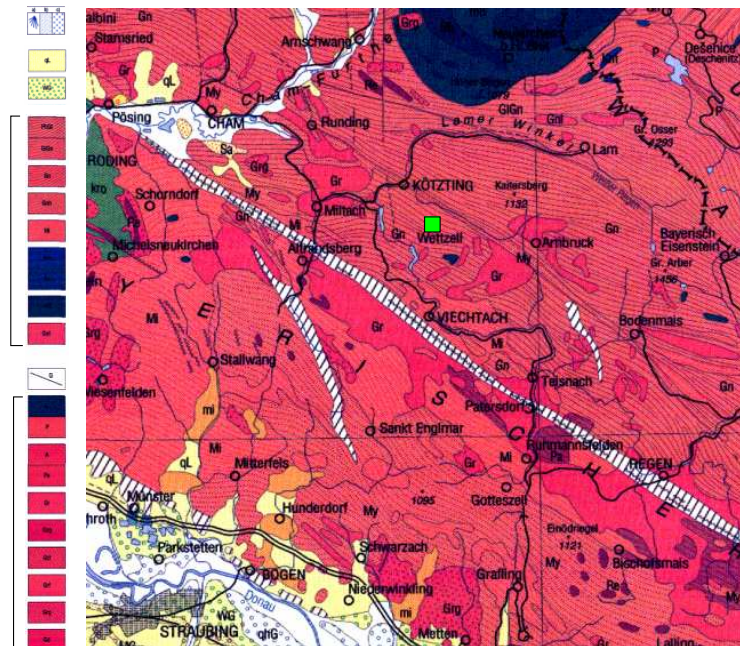
Telephone: _____

IP number: _____

river sediments
loess
grit, Würm ice age

metamorphic
rocks

plutonic
rocks



ALTM

Main network Bavaria
Altmühltal



Location:

lon: 11.519932 lat: 48.995178 alt: 430m

Cased pit, northeast of Beilngries

Underground: Ablehm

Colocated with GRC1 of GRF–array

Seismometer:

LE3Dlite

Concrete foundation, 3m below surface

Start:

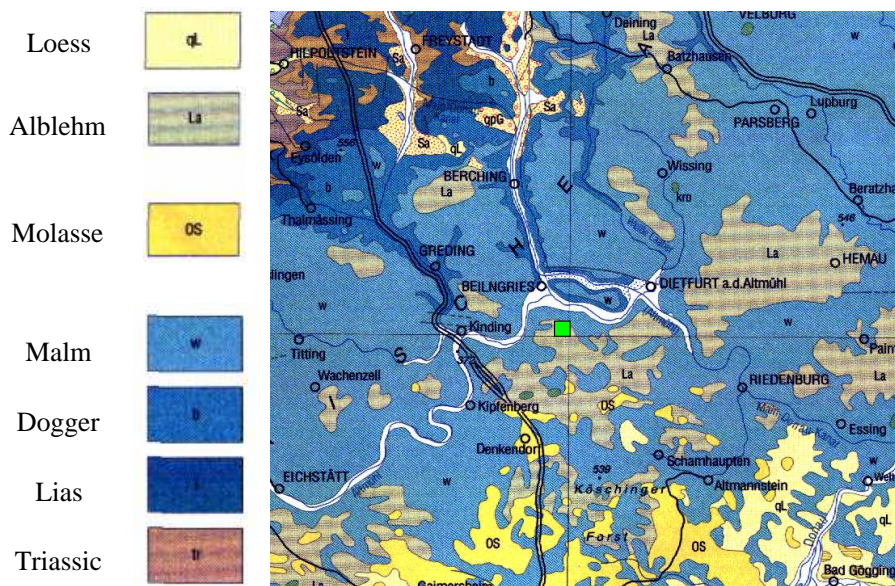
Jun. 20, 2001

Telephone:

08461/605639

IP number:

192.168.20.143



FUR

Main network Bavaria
Fürstenfeldbruck



Location:

lon: 11.275112 lat: 48.162968 alt: 570m

Concrete bunker, east of Fürstenfeldbruck

Underground: Moraine Ries / Mindel

GRSN station

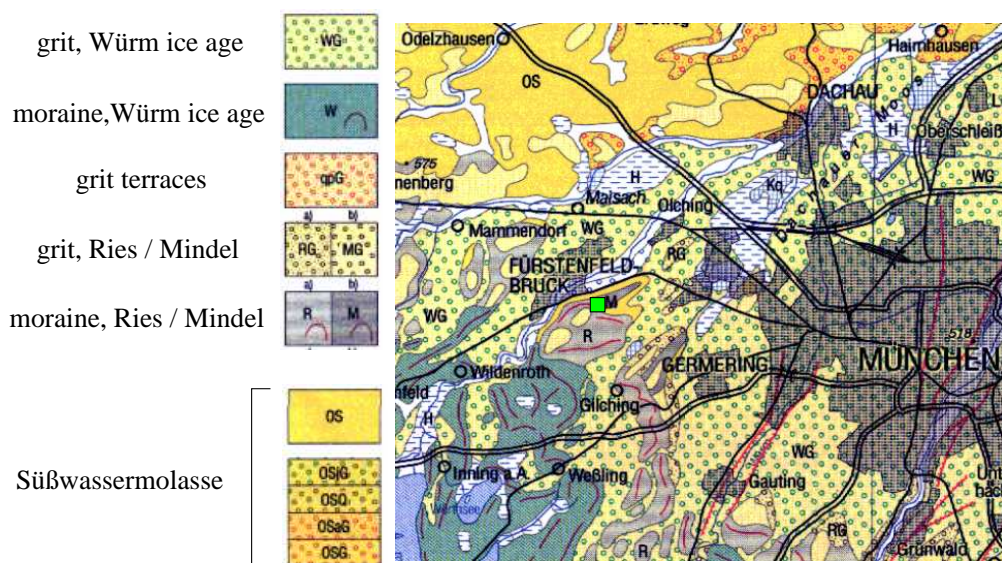
Seismometer: STS-2

Concrete foundation, 4m below surface

Start: Jun. 2, 2003

Telephone: _____

IP number: _____



BGLD

Main network Bavaria
Berchtesgadener Land



Location:

lon: 13.01250 lat: 47.65240 alt: 930m

Water reservoir, north of Berchtesgaden

Underground: Halstätter Kalk (limestone)

Mars88 station, old configuration !!

Seismometer: LE3Dlite

Concrete foundation, 4m below surface

Start: Oct. 1, 1999

Telephone: _____

IP number: _____

moraine, Würm ice age



Gossau



Losensteiner Schichten



Schrambachschichten



Liasbasiskalk



Hallstätter Kalk



Kössener Schichten



Dachsteinklak



Plattenkalk



Hauptdolomit



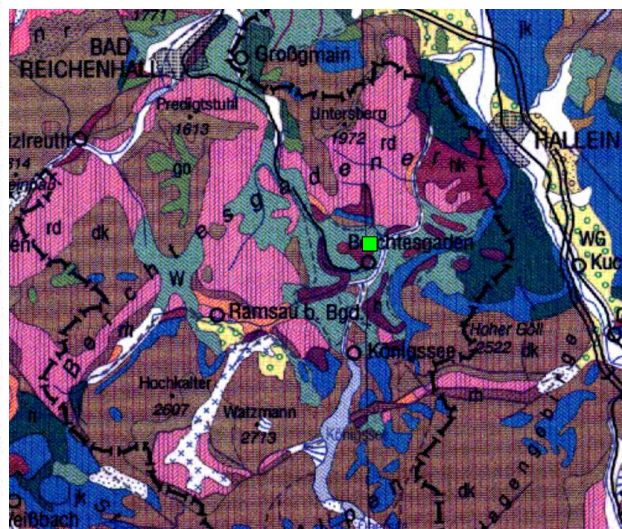
Raibler Schichten



Arlbergschichten



Ramsaudolomit



PART

Main network Bavaria
Garmisch–Partenkirchen



Location:

lon: 11.115670 lat: 47.496437 alt: 760m

Water reservoir, east of Partenkirchen

Underground: Plattenkalk (limestone)

Station offline !!

Seismometer: LE3Dlite
Concrete foundation, surface level

Start: Jan. 01, 2001

Telephone: _____

IP number: 192.168.20.146

Molasse Basin

silt, clay, marl,
lime-, sandstone,
silt

Helvetic Unit

marl, limestone
sandstone

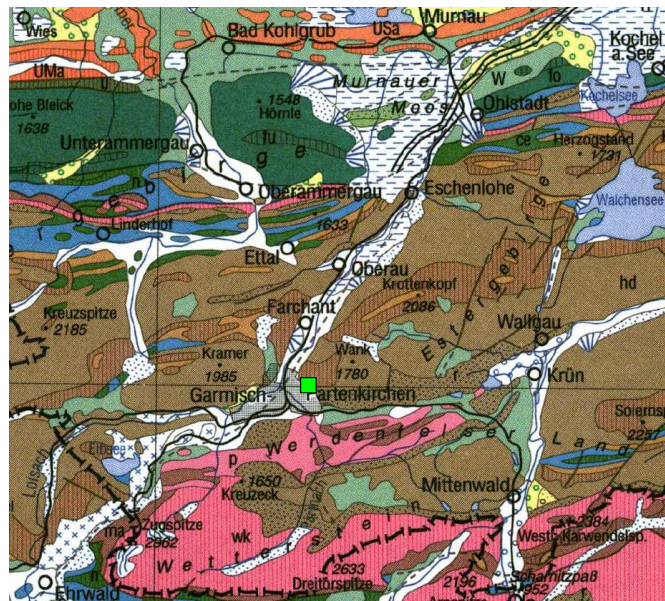
Flysch

marl, limestone
sandstone

Arosa-Zone

N. Calc. Alps

limest., dolomite
silt, clay, marl,
sandstone



OBER

Main network Bavaria
Oberstdorf



Location:

lon: 10.293368 lat: 47.406959 alt: 1000m

Water reservoir, south of Oberstdorf

Underground: Lime- and Sandstone

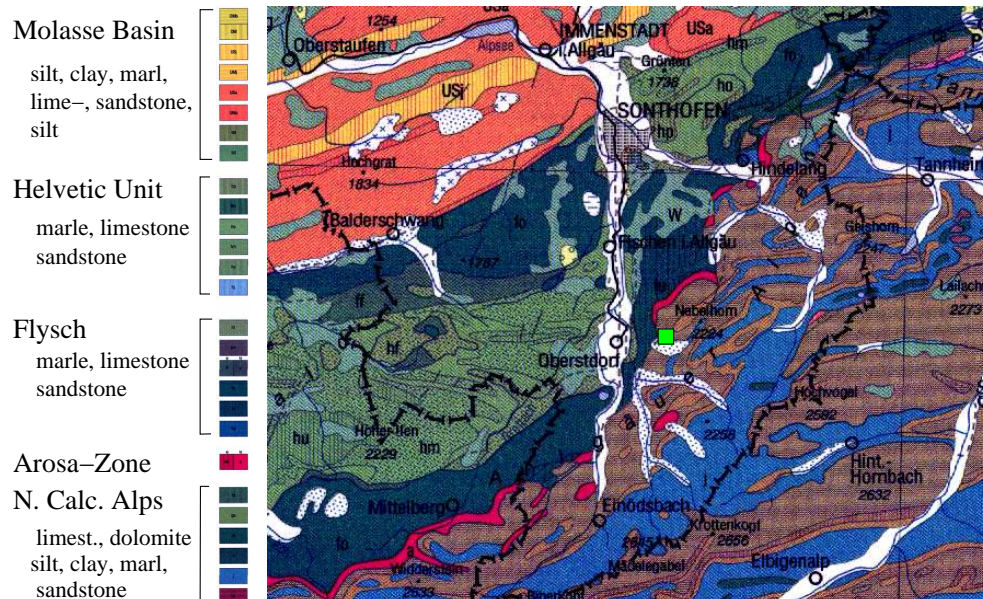
Seismometer: LE3Dlite

Concrete foundation, 3m below surface

Start: Mar. 18, 2002

Telephone: 08322 / 959078

IP number: 192.168.20.153



NORI

Main network Bavaria
Nördlinger Ries



Location:

lon: 10.624990 lat: 48.720263 alt: 480m

Water reservoir, east of Bissingen

Underground: Bunte Trümmermasse (impact breccia)

Sensor in separate building, distance 30m

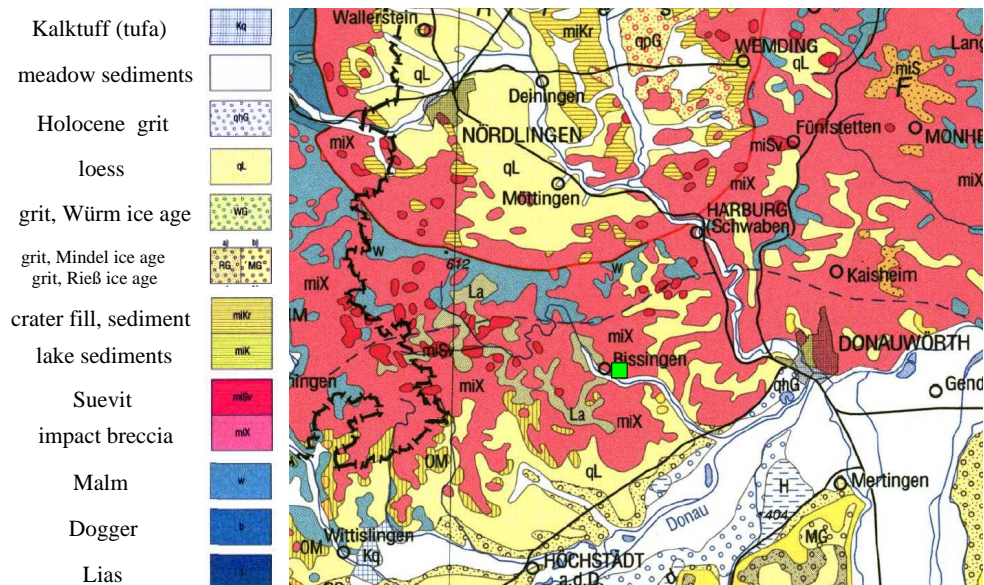
Seismometer: LE3Dlite

Concrete foundation, 4m below surface

Start: Nov. 15, 2002

Telephone: 09084 / 920974

IP number: 192.168.20.173



Appendix B

Content of Supplement CD

The Supplement CD is structured in subdirectories that correspond to the chapters of the thesis and has the following content:

Toni_Kraft_PhD.pdf

PDF file of the PhD thesis.

Part_1/Chapter_2

WWW_institute

Directory containing scripts and programs, necessary for the presentation of near-realtime seismological data on the internet homepage of the Geophysical Institute of the University of Munich (<http://www.geophysik.uni-muenchen.de>).

WWW_infocenter

Directory containing the HTML sources of the slide show presented at the info centers of the Bavarian Earthquake Service.

WWW_EDB

Directory containing the HTML sources and file system structure of the data presentation section of the internet homepage of the Bavarian Earthquake Service.

stationPC / dialerPC

Directories containing scripts, programs and configuration files for the station-PC and dialer-PC.

Baywatch.dat

Station book file for the Bavarian Seismological network, containing information on instrumentation, location and operation intervals of the stations. The fields of the file have the following meaning:

1	instrument number data logger
2	instrument type data logger
3	pre-amplification factor
4	bit resolution of data logger
5	instrument type data seismometer
6	running number
7	station code
8	longitude (WGS84)
9	latitude (WGS84)
10	error of coordinates
11	station elevation in meter (Bessel)
12+13	start of registration
14+15	end of registration
16	telephone number (if available)
17	IP number (last three digits)
18	name of station-PC (if available)
19	instrument number GPS/DCF antenna
20	station name

Part_2/Chapter_3PHASEN_no.dat

Phase arrival times from manual analysis used for the location in Chapter 3.

Format:	1 - 40	Hypo71 phase format [Lee & Lahr, 1975]
	44 - 48	amplitude ratio P/S (do not use!!)
	57 - 59	back azimuth from horizontal P first motion
	65 - 68	local magnitude
	73 - 74	applied full second correction (comp. Chap.2.2)

BULL2002.dat

Hypo71 location result described in Chapter 3. The format is follows the output format of Hypo71 [Lee and Lahr, 1975] and is elswise described in the file header.

HYMET_DATA

Directory containing precipitation and groundwater level data of the Mt. Hochstaufen region. File content is described in the file headers.

GIANT_DB

Directory containing the GIANT database [Rietbrock and Scherbaum, 1998]. Including the waveforms data of the Mt. Hochstaufen seismological network for 2002.

Part_2/Chapter_4

STAUFEN_obs.dat

NonLinLoc input file with arrival times derived from manual analysis, semi-manual analysis and cross-correlation analysis, described in 4. The format is conform to the NonLonLoc manual [Lomax et al., 2000].

mkVel.c

C program to generate the 3D-model with topography used for the relocation described in 4.

RH_topo_ev.dat

Binary data file containing the topographic model of the Mt. Hochstaufen region. The file contains single precision-float altitude data in a grid of 50 m × 50 m.

staufen.inp

NonLinLoc control file used for the location run. The format is conform to the NonLonLoc manual [Lomax et al., 2000].

BULL2002_NLLCC_all.dat

NonLinLoc location results described in Chapter 4. The format is follows the output format of Hypo71. Additional entries are:

Dabs	absolute hypocenter depth (positive down)
Dtopo	hypocenter depth bellow topography (positive down)
DOY	source time in decimal days of year

mkBestSol.f Fortran program to calculate the preferred focal mechanism described in Chapter 4. (needs include files: *param.inc* and *rot.inc*. The program is modified from Hardebeck and Shearer [2002].

Part_2/Chapter_5

RH_Rain95-02.dat

Four station mean precipitation data for Mt. Hochstaufen region for the years 1995-2002.

Acknowledgments

This study was to a major part supported by the Bavarian Ministry for Environment and by the Geological Survey of the Bavarian State. Financial support was provided by the German Research Foundation (DFG) and the EU Community initiative INTERREG III B Alpine Space Program SIS-MOVALP. Data was provided by the German Weather Service, SüdSalz GmbH in Bad Reichenhall and the Bavarian Bureau of Water Resources in Traunstein.

I thank the Bavarian Forest Administration for permitting the installation of mobile stations and access to forest roads. Special thanks are expressed to the communities of Fladungen, Wunsiedel, Arzberg, Mitterteich, Marktredwitz, Rotzendorf, Bissingen, Berchtesgaden, Garmisch-Partenkirchen, Oberstdorf, Bad Reichenhall, Inzell, Piding, Teisendorf, and Siegsdorf, to the tourist club "Die Naturfreunde", as well as to Mr. Waigl and Mrs. Kerkmann for the permission to install seismological stations on their properties. Special thanks for support, accommodation and the good times goes to Hansi Pauli and to landlord and landlady of Stoaneralm as well as to Martina and Heinz Frommelt from Staufenhaus.

I like to thank the following persons for giving logistic and technical support throughout the study and field campaign: Dr. Eberhard Schmedes, Dr. Joachim Wassermann, Werner Bauer, Peter Danecek, Teresa Reinwald, Julia Linder, Dr. Martin Beblo, Martin Feller, Dr. Erwin Geiß, Gunnar Jahnke, Michael Ewald, Gilbert Brietzke and Christian Verard. Special thanks are expressed to Dr. Sebastian Hainzl, for his cooperation, support and patience.

Thankfully I acknowledge my admired teacher Prof. Heiner Igel, for encouraging and supervising this work.

Curriculum Vitae – Toni Kraft

PERSONAL DETAILS

Date of Birth: March 24, 1970

Place of Birth: Munich, Germany

Nationality: German

Marital Status: Single

Gender : Male

PROFESSIONAL EXPERIENCE

since June 2006

Project Manager of the Earthquake Monitoring System of the German Indian Ocean Tsunami Early Warning System (GITEWS), GeoForschungsZentrum Potsdam, Section 2.4 (Seismology)

July 2003 - December 2005

Graduate research assistant at the Department of Earth and Environmental Sciences, Geophysics Section, Ludwig-Maximilians University Munich, Seismology Group

November 2000 - June 2003

Seismologist at the Bavarian Earthquake Service, Geophysical Observatory of the Ludwig-Maximilians University Munich, Seismology Section

August 1999 - October 2000

Graduate research assistant at the Institute of Pure and Applied Geophysics, Ludwig-Maximilians University Munich, Seismics Group, TRANSALP-Project

UNIVERSITY EDUCATION

July 2003 - May 2006

Ph.D. student at the Department of Earth and Environmental Sciences, Geophysics Section, Ludwig-Maximilians University Munich, Seismology Group

Thesis title: *A New Seismological Network for Bavaria and its Application to the Study of Meteorologically Triggered Earthquake Swarms*

Supervisor: Prof. Dr. H. Igel

June 1999

Graduated in Geophysics, Ludwig-Maximilians University Munich, Degree: Diplom

Thesis title: *The seismicity of the northern Eastern Alps and source mechanisms of selected earthquakes.* (translated)

Supervisor: Prof. Dr. H. Gebrande

October 1992 - June 1999

Studied Geophysics with Mathematics, Physics, theoretical Physics, Geology, Mineralogy and Meteorology at the Ludwig-Maximilians University Munich

SCHOOL AND PROFESSIONAL EDUCATION

1989 - 1991

Berufsoberschule Technik, in Munich

Matriculation standard for technical universities and technical studies at universities

1986 - 1989

Stadtwerke München, in Munich

Apprenticeship as metal worker (Rohrinstallateur) at municipal utilities of Munich

1976 - 1986

Basic schooling up to Mittlere Reife, in Munich

Practically and theoretically oriented education for trade, technical and administrative professions

CIVILIAN SERVICE

October 1991 - December 1992

Montessori School, Aktion Sonnenschein, Munich

Worked in an integrational school for disabled children.